HOC APPROACH TO THE DYNAMICS OF WAVES IN EXCITABLE MEDIA

Ph.D. Thesis

Devanand

DEPARTMENT OF MATHEMATICS
INDIAN INSTITUTE OF TECHNOLOGY GUWAHATI
GUWAHATI-781039, INDIA
March, 2020

TH-2268_136123014


भारतीय प्रौद्योगिकी संस्थान गुवाहाटी
Indian Institute of Technology Guwahati

HOC APPROACH TO THE DYNAMICS OF WAVES IN EXCITABLE MEDIA

A thesis submitted
in partial fulfillment of the requirements
for the degree of

DOCTOR OF PHILOSOPHY

by

Devanand

(Roll Number: 136123014)

(Under the supervision of Prof. Jiten C. Kalita)

to the

DEPARTMENT OF MATHEMATICS
INDIAN INSTITUTE OF TECHNOLOGY GUWAHATI
GUWAHATI-781039, INDIA
March, 2020

TH-2268_136123014


भारतीय प्रौद्योगिकी संस्थान गुवाहाटी
Indian Institute of Technology Guwahati

DECLARATION

I hereby declare that the work contained in the thesis entitled **"HOC Approach to the Dynamics of Waves in Excitable Media"** has been done by me, under the guidance of **Dr. Jiten C. Kalita**, Professor, Department of Matheamtics, Indian Institute of Technology Guwahati, for the award of the degree of Doctor of Philosophy and this work has not been submitted elsewhere for a degree.

Guwahati
March, 2020.

Devanand
Roll No: 136123014
Department of Mathematics
Indian Institute of Technology Guwahati
Guwahati-781039, India

CERTIFICATE

It is certified that the work contained in this thesis entitled **“HOC Approach to the Dynamics of Waves in Excitable Media”** by **Devanand**, a student of Department of Matheamtics, Indian Institute of Technology Guwahati, for the award of the degree of Doctor of Philosophy has been carried out under my supervision and this work has not been submitted elsewhere for a degree.

Guwahati
March, 2020

Prof. Jiten C. Kalita
Department of Mathematics
Indian Institute of Technology Guwahati
Guwahati-781039, India

Dedicated

To

My Parents

Indian Institute of Technology Guwahati

Acknowledgements

First and foremost, I would like to convey my indebtedness and render warmest thanks to my thesis supervisor, **Prof. Jiten C. Kalita**, who made this work possible. I express my deep and sincere gratitude to him for his constant support, enthusiastic encouragement, patient guidance, constructive criticisms, and scholarly inputs, throughout all stages of my research work. I am deeply indebted to him for his utmost care and making me feel free to express my views. His wholehearted cooperation and support inspired and enabled me to carry out and completing this research. His erudition and rich experience shaped the course of the study and sharpened its outcome. I will forever be grateful to him for his encouragement in every aspect of my life. Once again, I thank you from the bottom of my heart, Sir!

I owe a huge debt of gratitude to Mrs. Deepshikha Choudhury, who showered me with her motherly love and affection. In reality, it is very difficult to acknowledge her with only a few words.

I extend my deepest appreciation to my doctoral committee members Dr. P.A.S. Sree Krishna, Prof. Siddhartha Pratim Chakrabarty, and Prof. Anoop K. Dass, for their encouragement, insightful comments, and valuable suggestions. I greatly appreciate the help and cooperation of all the faculty members of the Department of Mathematics, Indian Institute of Technology Guwahati. I thank all the staff members of the Department of Mathematics, Indian Institute of Technology Guwahati, for their assistance in official and technical matters. I also express my heartfelt gratitude to all the teachers who motivated and helped me in some way or another during my school and college days.

This thesis has been written during my stay at the Mathematics Department of the Indian Institute of Technology Guwahati. I sincerely acknowledge the Indian Institute of Technology Guwahati for providing a very nice educational environment and various facilities to carry out my research work. I am highly grateful to the Ministry of Human Resource Development, Government of India, for its financial support during the period of my research work.

I take this opportunity to convey my gratefulness to my friends and co-researchers. I would like to thank Anirban, Biswajit, Madhusudan, Sonjoy, Koyel, Ranjan, Maneesh, Debasish, Ashish, Ankur, Swapnendu, Ramesh, N. Balasubramani, Anirudha, Abhishek, Pratibha, Tanushree, Swarup, Pankaj, Raghav, Sakshi, Sailen for all timely help, encouragement, and support. My heartfelt thanks to my senior Dr. Sougata Biswas for his friendship, brotherly love, care, valuable suggestions and help throughout this work.

I express my very profound gratitude to my parents, Mrs. Fulmati Devi (mother) and Mr. Haridas Prasad (father), for their endless love, encouragement, guidance, help, and prayer that they have bestowed on me, whom I am really very proud of. I would like to thank my elder sisters Usha, Asha, and Manisha for their pampering love and care. Especially, I would like to thank my younger brother Sampoorna Nand for his unfailing support and for always believing in me and encouraging me to follow my dreams.

Lastly, I would like to convey my deepest gratitude to Dharmendra Prasad, Chandrashekhar Prasad, Shyam Bihari, Anil Kumar Verma, Praveen Singh, Shailesh Bharatwasi, Kuldeep Kumar Verma for their encouragement and support.

And above all, I thank God for everything.

March, 2020 **Devanand**

प्रौद्योगिकी संस्थान गुवाहाटी • Indian Institute of Technology Guwahati •

Abstract

This work is concerned with the High Order Compact (HOC) simulation of spiral waves in excitable media in general and study of spiral wave dynamics in particular. An existing unconditionally stable, $O(h^4, (\Delta t)^2)$ implicit HOC scheme for the two dimensional convection-diffusion equations is reconstructed to discretize some of very well-known models of pattern formation in excitable media, notable amongst them are the Barkley and the FitzHugh-Nagumo (FHN) models. In the process it removes the debilitating effects of the frequently used lower order accurate schemes, notably Euler's explicit scheme to accurately resolve the underlying physiological processes. The discrepancies of explicit schemes are explained through the concept of implicit reaction, dispersion and diffusion by carrying out a thorough analysis of corresponding modified differential equation. Contrary to the usual practice of using state variables solely to explore the dynamics of spiral waves, the spiral wave tip is used as a major tool to study the same. Our study reveals that while the use of the tip leads to accurate prediction of the dynamics, many a time, sole use of the state variables bring about misleading conclusions.

The simulations of spiral waves from our numerical computations are found to be extremely close to the experimental and the available benchmark results in the existing literature. In the process, fourth order accurate approximations to the periodic boundary conditions are derived and used to study the effect of zero flux and periodic boundary conditions on the spiral wave patterns resulting from the Barkley and FHN models in excitable media. Further, the effect of an obstacle on the dynamics of periodic rotating spiral waves is studied, where it is seen to change the trajectory of spiral tip which eventually settles into periodic motion. The reconstructed HOC scheme is then employed to the Oregonator model to study the effect of straining on the stable rotating spiral wave, which is seen to generate a host of complex patterns in three broad regimes: no break up, transitional and break up regimes; these regimes are different from the ones predicted in literature earlier. Finally a dual-purpose implicit, unconditionally stable HOC scheme is developed to discretize the 3D unsteady R-D equations, which is seen to resolve both 3D reaction-diffusion and convection-diffusion equations with equal ease, and could go a long way in simulating scroll waves in excitable media.

TH-2268_136123014

Contents

TH-2268_136123014

List of Figures

TH-2268_136123014

Institute of Technology

भारतीय प्रौद्योगिकी संस्थान गुवाहाटी • Indian Institute of Technology Guwahati •

List of Tables

TH-2268_136123014

Chapter 1

INTRODUCTION

1.1 General background

Over the last few decades the study of spatio-temporal pattern formations occurring in diverse fields such as mathematical, physical, biological and engineering sciences, has been of considerable interest amongst the followers of the above mentioned fields. The most notable work in the field of pattern formations at the earliest part was done by the famous British mathematician and theoretical biologist Alan M Turing in 1952 [108], who for the first time studied the biological mechanism of morphogenesis through a mathematical model. The mathematical model developed by Turing in order to study pattern comprises of a system of the unsteady nonlinear reaction-diffusion (R-D) equations in which the transport variables are the concentrations of the chemicals that lead to the formation of pattern. Turing's theory of the pattern formation insists that both the transport variables must diffuse at different rates in order to form the patterns. The transport variable which diffuse at a slower rate is known as activator and the faster one is called an inhibitor.

There has been a rejuvenated interest in another kind of pattern formation in excitable media through system of nonlinear R-D equations. It is the study of spiral and scroll waves in two dimensional (2D) and three dimensional (3D) excitable media respectively. *An excitable medium can be defined as; a dynamical system distributed continuously in space, each elementary segment of which possesses the property of excitability. Neighbouring segments of an excitable medium interact with each other by diffusion like local transport processes.* More elaborately, an excitable medium can be characterized as a group of

TH-2268_136123014

individual points communicating only with it's intimate neighbours which inherit a degree of excitableness. In an excitable medium a point can be either at state of rest, in a state of excitement or somewhere between these two extrema. An application of small perturbations applied to the point at state of rest will lead to the point to be at rest, but while the applied perturbations crosses a certain threshold, it results in an excitation and after a certain period of time, the point will come back slowly to the state of rest, which is called as the refractory phase. The excitation of a point is passed on to its neighbouring points through the process of diffusion. A state of recovery will follow the refractory phase and during this phase the point will lose its ability to get excited. An intuitive example of excitable medium is a forest fire; the fire will spread like diffusion and trees on fire will ignite the neighbouring trees. After a tree has been burnt down, the fire can pass this particular point afresh only after it has been regrown. It is worth mentioning that the pattern formations in excitable media do not require faster diffusion of the inhibitor component in comparison to the activator component; in fact the diffusion of the inhibitor component is not mandatory at all, opposed to the ones propounded by Turing theory of pattern formations. For more details, one can see [35, 101, 107].

In the current dissertation, we are primarily concerned about the dynamics of spiral wave patterns in 2D excitable media under different conditions through the simulations of systems of nonlinear R-D equations. A prototype of a spiral wave is depicted in figure 1.1(a), where one can see a typical spiral wave being represented by different colours. Here, the red colour represents the excitation field while the blue colour exhibits the inhibitor field [35]; and their interaction determines the behaviour of the spiral wave.

Investigation of the dynamics of rotating spiral wave patterns has aroused a substantial interest in recent decades due to their applications in some intriguing biological phenomenon such as propagation of spiral wave in heart leading to lethal arrhythmia, which characterized by the disruption of the normal cardiac rhythm [18, 30, 60, 77, 87, 90, 99, 120] and the aggregation of dictyostelium discoideum amoebae [62]. Alike rotating spiral wave patterns have also been encountered in a famous chemical reaction called Belousov-

Zhabotinsky (B-Z) reaction which represents oxidation of malonic acid by bromate, named after the two eminent Rusian biochemists Boris Pavlovich Belousov and Anatol Zhabotinsky [10, 38, 45, 84, 115, 120]. The B-Z reaction exhibits patterns such as rotating spirals or expanding trigger waves in extended excitable systems like thin layers of B-Z reaction (see figure 1.1(b)). It is interesting to note that both these scientist are from different eras and carried out their research independently [12, 38, 84]. It was Belousov who initiated the work in the early 1950's and after several years, it was carried out by Zhabotinsky in the mid of 1960's without both of them being aware of each others work. It was only in the early 1970's that Arthur Winfree [33, 46, 112–116] brought their work to the public notice and subsequently made the B-Z reaction very popular. Since then there has been a lot of development in the experimental and numerical studies on the pattern formation in excitable media.

The main dynamical features of a broad class of excitable media can be obtained by simulating the two component nonlinear R-D systems. The mathematical models which have been employed to study the dynamics of self sustaining spiral and scroll waves in excitable media can be written as in following form:

$$\frac{\partial u}{\partial t} = \frac{1}{\epsilon} f(u,v) + D_u \nabla^2 u, \tag{1.1}$$

$$\frac{\partial v}{\partial t} = g(u,v) + D_v \nabla^2 v. \tag{1.2}$$

Here D_u and D_v are the non-negative diffusion coefficients corresponding the transport variables u and v respectively. The parameter ϵ is a positive constant whose value lies between 0 and 1, that determines how slowly the variable v (referred as recovery) evolves with time as compared to the variable u (referred as excitable). The functions $f(u,v)$ and $g(u,v)$ describe the local reaction kinetics of the transport variables u and v respectively; and the function $g(u,v)$ controls the growth of recovery variable v. The operator ∇^2 is the Laplacian operator, its dimension depending upon whether one is studying the 2D spiral or 3D scroll waves.

One of the elementary ways to explore the dynamics of spiral wave is to study of spiral wave as a motion of two curve, first excitation wave front and the second recovery wave back. It is also important to note that the excitation front and recovery wave back meet each other at a point and this point is a phase singularity known as the spiral tip. Thus the location of spiral wave tip plays a significant role in the analysis of the dynamics of spiral wave. Therefore the evolution of the rotating spiral waves are characterized by the tracking of the tip of such waves. Several numerical techniques have been exploited to determine the location of spiral tip [35, 40, 65, 101], among which the most well known method is to find the intersection of isolines of the excitable u and recovery v variables (see figure 1.1(c)). Mathematically, the tip is the intersection of contours given by

$$u(x, y, t) = u_*, \tag{1.3}$$

$$v(x, y, t) = v_*, \tag{1.4}$$

where x and y are coordinate variables and t is the time. The choices of the u_* and v_* must be within some limit as shown in figure 1.1(c).

(a) (b) (c)

Figure 1.1: (a) A typical spiral wave [35]: colour red representing excitation and blue blue representing inhibitor field, (b) spiral waves observed in B-Z reaction [107], and (c) spiral wave tip as the intersection of two isocontours (from our own simulations).

Initially, it was assumed that spiral wave tip rotates periodically *i.e.* tip path is a closed curve. Moreover the tip of rigidly rotating spiral wave traces a perfect circle (see figure 1.2(a)). But it was Winfree, who for the first time in 1973 [115], detected that the rotating spiral waves in B-Z reaction do not necessarily rotate rigidly about fixed centers and observed that spiral wave tip could trace out complex patterns (e.g. floral trajectories see figures 1.2(b)-(c)) as they rotate. In other words spiral wave tip paths perform either periodic (stable) and non-periodic motion depending on the reaction parameters and for such a non-periodic rotating spiral waves, Winfree coined a term called "meandering" of the waves.

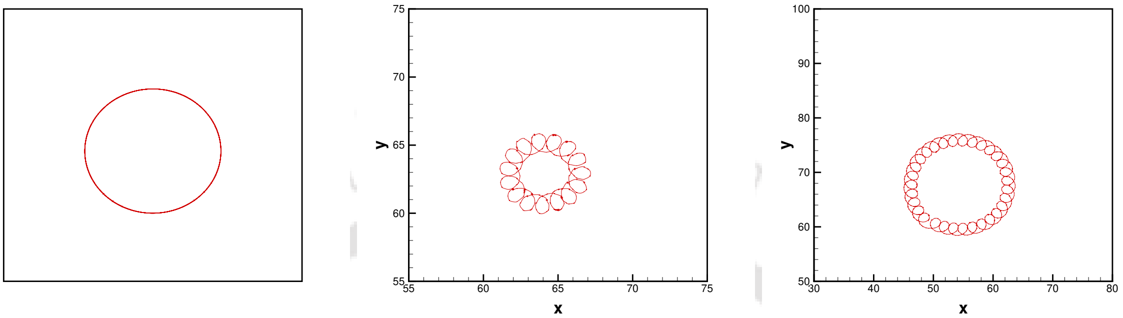

(a) (b) (c)

Figure 1.2: Spiral wave tip paths depicting different behaviours: (a) periodic, (b) meandering (outward petal) and (c) meandering (inward petal), all from our own simulations.

1.1.1 Some mathematical models of excitable media

By choosing different expressions for the functions $f(u, v)$ and $g(u, v)$ in the system (1.1)-(1.2), one can arrive at different physical models for mathematically modelling the motion of spiral and scroll waves. The notable amongst such models are: the FitzHugh-Nagumo [40], the Oregonator [110] and the Barkley [9] model. In the following, we give brief information about these models:

FitgHugh-Nagumo model:

In 1952, Alan Lloyd Hodgkin and Andrew Huxley derived a model constituting a coupled set of differential equations to describe the ionic basis of action potential based on their series of electro-physiological experiments on the squid giant axon. This model is known as Hudgkin and Huxely (H-H) model [43], for which they received the 1963 Nobel Prize in medicine or physiology. This model was further simplified by famous Biophysicist Richard FitzHugh. Later in 1964, Jin-Ichi Nagumo constructed a circuit replicating the model and as a tribute to him, the system is now called as the FitzHugh-Nagumo (FHN) model [40].

Indian Institute of Technology

The reaction terms of FHN model that has been used in the study of the characteristics of several excitable medium are given by,

$$f(u,v) = Bu(u-C)(1-u) - v, \quad g(u,v) = (u - \gamma v). \tag{1.5}$$

There is a another variant of FHN model for which the functions f and g are:

$$f(u,v) = u - \frac{u^3}{3} - v, \quad g(u,v) = (u + \beta - \gamma v). \tag{1.6}$$

B, C β and γ are model parameters.

Oregonator model:

In [32], Field and Noyes generalized the chemical mechanism of Field *et. al.* [31], for the oscillatory Belousov chemical reaction by a model and this model which is composed of five steps involves three independent chemical intermediate. Subsequently in 1980, Tyson and Fife [110], devised a system of R-D equations depending upon the kinetics of B-Z reaction, which is widely known as the "Oregonator" model and the reaction terms for the Oregonator model are given by

$$f(u,v) = (u - u^2 - av\frac{u-b}{u+b}), \quad g(u,v) = u - v, \tag{1.7}$$

where a and b are parameters.

Barkley model:

Further, a famous mathematician Dwight Barkley [9], proposed a simplified version FHN model of excitable media which is widely known as "Barkley model". This model has been derived in a such manner that it can be used to explain all the characteristics of excitable media. The reaction terms of the simplest form of the Barkley model can be written as:

$$f(u,v) = u(1-u)\left(u - \frac{v+b}{a}\right), \quad g(u,v) = u - v, \tag{1.8}$$

where a and b positive parameters and their values can be adjusted according to the requirement of an excitable system.

The form of the functions $f(u, v)$ and $g(u, v)$ in equations (1.5), (1.6), (1.7) and (1.8) renders high nonlinearity to the systems and as such finding their solutions analytically is extremely difficult. Consequently, numerical solution is the only option for the solution of such systems. Amongst the well known numerical approaches, the finite difference method has been the most popular and frequently used ones in discretizing the governing equations in excitable media owing to their simplicity in application. This method is based on setting up a grid on the problem domain and then approximation of the derivative appearing in the governing equations by replacing them with difference quotients at each grid point. The discretization results in a system of linear algebraic equations, which can be solved with some matrix solution method. Most of finite difference approximations to the derivatives are based on Taylor series expansion of the variables at these grid points. The order of accuracy of such a scheme is determined by the leading term in the truncation error (TE) of the Taylor's expansion. For example, finite difference scheme is said to be accurate of order m and written as $O(h^m)$ where h is the step size, if the TE is asymptotically proportional to h^m.

1.2 Motivation and the work

From the time, Winfree made pattern formations in excitable media popular in the early 1970's, there has been a lot of development in the experimental and numerical studies on the dynamics of spiral and scroll waves of the excitable media. A meticulous inspection on such numerical studies reveals that the majority of them were carried out by using the standard Euler's forward time centered space (FTCS) finite difference schemes [5,17,28,29, 40,45,77,79,85,90]. These schemes are conditionally stable, first order accurate in time and second order accurate in all spatial variables. Therefore, simulations resulting from these schemes might not be able to accurately represent the actual phenomenon owing to their lower order accuracy. As such there is an imminent need for exploring and exploiting high order accurate efficient finite difference schemes for the simulation of pattern formation in excitable media. Such attempts in this direction have been few and far between and the motivation of the current work comes from that. Not only it inspects the probable causes of failure of the Euler's explicit scheme in accurately resolving the actual physiological phenomena through a modified differential equation (MDE) analysis, but also exploits the good features of an existing high order compact (HOC) finite difference scheme [53] to bring out some hitherto unexplored features of spiral wave dynamics.

This scheme [53], which is second order accurate in time and fourth order accurate in space has been reconstructed to discretize the governing R-D equations of various models in 2D excitable media. In the process we have also developed a fourth order approximation to the periodic boundary conditions for the FHN model and further examined its effect on spiral waves dynamics. Besides we have also developed an implicit, unconditionally stable, temporally second order and spatially fourth order accurate HOC scheme to discretize the models of 3D excitable media.

Furthermore, depending upon the reaction parameters, spiral wave in 2D excitable media can execute either stable or meandering rotation [5, 40]. The motion of spiral tip plays a very crucial role in transition of a stable rotating wave from a periodic to a meandering one and eventual spiral wave break-up. The importance of this can be gauged from the fact that the exact occurrence of the aforesaid phenomenon is observed in human heart where there is a transition from stable to polymorphic arrhythmias and then to fibrillation and sudden cardiac death [40]. Despite this, almost all the numerical studies utilize only the state variables in order to examine the stability of rotating spiral waves. Thus a precise numerical treatment requires the use of the spiral tip as a major tool for the investigation of such transition. In line with this, the current dissertation attempts a comprehensive spectral density analysis exploiting the spiral tip motion to study the dynamics of spiral waves. We have also carried out the stability analysis of the rotating spiral wave solutions resulting from the reconstructed HOC scheme.

In many practical fields, one comes across the interaction of the spiral waves with obstacles present or placed in excitable media, which may in turn affect its dynamics. For example, rotating waves of electrical activity in heart may become stable after being pinned to unexcitable tissue (an obstacle) and this pinned spiral waves can be removed by a process known as unpinning of spiral waves where an electrical field is applied to the excitable media [29]. Interaction of meandering spiral waves with obstacles may also results in the break up of spiral waves [79]. Looking at the importance of the obstacles on the spiral waves dynamics, we also endeavour to examine the effect of placing an obstacle on the dynamics of stable rotating spiral waves in the current thesis.

A careful look at the existing literatures will reveal that most of the numerical studies on spiral wave dynamics have been performed without considering the effect of medium motion which can be mathematically modelled by the addition of an advection term in each of the equations of the system (1.1)-(1.2). It is also important to note that in laboratory experiments, the interaction between the excitation waves and dissipative structure results in chaos and breakup of waves due the strong convective motions. Only very few numerical studies (for example [14,16,94,95]) have been carried out by considering the presence of the effect of medium motions. The current study also examines the effect of medium motion on the spiral wave dynamics through the B-Z system which is seen to result in many complex behaviours of the spiral waves.

1.3 Organization of the dissertation

In chapter 2, we reconstruct an existing HOC finite difference scheme to discretize the 2D unsteady reaction-diffusion equations after providing a brief introduction of the HOC scheme. Chapter 3 deals with the applications of this reconstructed HOC scheme to solve some models of 2D excitable media. Then in chapter 4, we study the dynamics of spiral waves under the effect of obstacles through the Barkley model while in chapter 5, we perform numerical studies on the dynamics of spiral wave under the effect of straining through the Oregonator model. Chapter 6 is concerned with the development of an HOC finite difference scheme to solve the 3D dimensional unsteady R-D equations. Finally in the chapter 7, we summarize the achievements our whole work and provide an outline of possible future studies.

भारतीय प्रौद्योगिकी संस्थान गुवाहाटी • Indian Institute of Technology Guwahati •

Chapter 2

THE RECONSTRUCTED HOC FINITE DIFFERENCE SCHEME

In this chapter, we detail the process of reconstruction of a recently developed HOC finite difference scheme by Kalita [53], which has been used in all simulations carried out in the current dissertation for 2D pattern formation. In the process, we also provide a brief account of the different mechanisms available in existing literature for deriving HOC schemes.

An HOC finite difference scheme may be defined as one "which utilizes grid points located only directly adjacent to the node about which the difference are taken and have an order of accuracy greater than two" [50]. As stated above, several mechanisms have been adopted to obtain high order compactness for the finite difference schemes. For example, Gupta *et. al.* [42] use series expansion to the difference equations while Dennis and Hudson [26] exploit a transformation that involves expanding the exponential of a definite integral of the convective coefficient of the concerned partial differential equation (PDE). Besides the aforesaid mechanisms, high order compactness can also be achieved through substituting the leading truncation error (TE) terms of the standard central difference approximation by using the original differential equations. This was first effectuated by Lax and Wendroff [6, 44, 88] on the time dependent hyperbolic PDEs, where they raised the time accuracy from $O(\Delta t)$ to $O[(\Delta t)^2]$ by approximating the second order time derivative in a Taylors series expansion by exploiting the original PDE. The idea of Lax-Wendroff for enhancing the spatial accuracy was first implemented by Mackinnon

TH-2268_136123014

and Carey [68]. Abarbanel and Kumar [1], derived a temporarily second and spatially fourth order accurate scheme for the Euler equation. Furthermore, several research was performed by Mackinnon and Johnson to develop schemes for two dimensional (2D) steady state convection-diffusion equations. Moreover the idea of Macknnon and Johson [69] was further extended by Spotz and Carey [102, 103] for the stream function vorticity formulation of 2D the Navier-Stokes (N-S) equations.

In in past two decades, Kalita and his group have developed several HOC schemes for both steady and unsteady 2D and 3D convection-diffusion equations [50, 52, 53, 55, 56, 61, 74, 82, 96–98]. Most of these schemes were implemented to solve the problems arising out of the fluid flow with great success. However, very recently, Kalita [53] has developed an HOC scheme for the dual purpose of discretizing the two dimensional unsteady R-D and convection-diffusion equations. The Scheme was seen to efficiently handle the systems of R-D equations with appropriate boundary conditions emerging from the problems in the field of pattern formation. In the current work, we reconstruct the HOC scheme of Kalita [53] to simulate the models of 2D excitable media such as the Barkley, the Oregonator and the FHN models. Each of the component of the aforesaid models is the 2D unsteady R-D equation which can be written as,

$$\frac{\partial \psi}{\partial t} - D\left(\frac{\partial^2 \psi}{\partial x^2} + \frac{\partial^2 \psi}{\partial y^2}\right) + d(x, y, t)\psi = F(x, y, t). \tag{2.1}$$

Here d and D are the reaction and diffusion (positive) coefficients for the transport variable $\psi(x, y, t)$, whereas the function $F(x, y, t)$ is the forcing term.

In order to obtain the HOC scheme for equation (2.1), we first approximate it by the standard FTCS scheme at the $(i, j)^{\text{th}}$ grid point of a rectangular domain ($x_0 \leq x \leq x_m$, $y_0 \leq y \leq y_n$) with uniform Cartesian grid sizes h and k in the x- and y-directions respectively and time step Δt yielding

$$\left[\delta_t^+ - D\left(\delta_x^2 + \delta_y^2\right) + d_{i,j}^n\right]\psi_{i,j}^n - \tau_{i,j} = F_{i,j}^n, \tag{2.2}$$

where δ_t^+ is the first order forward difference operator for time t, δ_x^2 and δ_y^2 are the second order central difference operators in spatial directions x and y respectively; with ψ^n_{ij} denoting the value of ψ at grid point $(x_i(=x_0+ih), y_j(=y_0+jh))$ at the n^{th} time level. Here $\tau_{i,j}$ is the truncation error (TE) which is given by

$$\tau_{i,j} = \left[\frac{\Delta t}{2}\frac{\partial^2\psi}{\partial t^2} - \frac{Dh^2}{12}\frac{\partial^4\psi}{\partial x^4} - \frac{Dk^2}{12}\frac{\partial^4\psi}{\partial y^4}\right]_{i,j} + O((\Delta t)^2, h^4, k^4). \tag{2.3}$$

In order to accomplish the task of obtaining an $O((\Delta t)^2, h^4, k^4)$ HOC scheme for equation (2.1), we approximate each of the leading derivative terms of equation (2.3) using the original equation (2.1) as an auxiliary relation, which can be differentiated to give expressions for higher derivatives. All spatial derivatives are approximated by using central difference operators, forward time difference operator for ψ and backward temporal difference operator for d and F. The leading terms of the right hand side of equation (2.3) can be approximated as

$$\left[\frac{\partial^2\psi}{\partial t^2}\right]_{i,j} = \left(D\delta_x^2 + D\delta_y^2 - d^n_{i,j}\right)\delta_t^+\psi^n_{i,j} - \psi^n_{i,j}\delta_t^- d^n_{i,j} + \delta_t^- F^n_{i,j} + O((\Delta t), h^2, k^2), \tag{2.4}$$

$$-\left[D\frac{\partial^4\psi}{\partial x^4}\right]_{i,j} = \left(-\delta_x^2\delta_t^+ + D\delta_x^2\delta_y^2 - 2\delta_x d^n_{i,j}\delta_x - \delta_x^2 d^n_{i,j} - d^n_{i,j}\delta_x^2\right)\psi^n_{i,j} + \delta_x^2 F^n_{i,j} + O((\Delta t), h^2, k^2), \tag{2.5}$$

$$-\left[D\frac{\partial^4\psi}{\partial y^4}\right]_{i,j} = \left(-\delta_y^2\delta_t^+ + D\delta_x^2\delta_y^2 - 2\delta_y d^n_{i,j}\delta_y - \delta_y^2 d^n_{i,j} - d^n_{i,j}\delta_y^2\right)\psi^n_{i,j} + \delta_y^2 F^n_{i,j} + O((\Delta t), h^2, k^2), \tag{2.6}$$

where δ_x and δ_y are the first order central difference operator along x- and y-directions respectively, with δ_t^- being the first order backward difference operator for time t. Using the approximations (2.4)-(2.6) in equation (2.3), τ_{ij} can be written as

$$\begin{aligned}\tau_{i,j} = &\left[\frac{D\Delta t}{2}\left(\delta_x^2+\delta_y^2\right) - \frac{\Delta t}{2}d^n_{i,j} - \left(\frac{h^2}{12}\delta_x^2 + \frac{k^2}{12}\delta_y^2\right)\right]\delta_t^+\psi^n_{i,j} - \frac{\Delta t}{2}\delta_t^- d^n_{i,j}\psi^n_{i,j} + \frac{\Delta t}{2}\delta_t^- F^n_{i,j}\\ &+\left[\frac{D\left(h^2+k^2\right)}{12}\delta_x^2\delta_y^2 - d^n_{i,j}\left(\frac{h^2}{12}\delta_x^2 + \frac{k^2}{12}\delta_y^2\right) - \left(\frac{h^2}{6}\delta_x d^n_{i,j}\delta_x + \frac{k^2}{6}\delta_y d^n_{i,j}\delta_y\right)\right]\psi^n_{i,j}\\ &-\left(\frac{h^2}{12}\delta_x^2 d^n_{i,j} + \frac{k^2}{12}\delta_y^2 d^n_{i,j}\right)\psi_{i,j} + \frac{h^2}{12}\delta_x^2 F^n_{i,j} + \frac{k^2}{12}\delta_y^2 F^n_{i,j} + O(\Delta t^2_{h,k}, h^4, k^4),\end{aligned} \tag{2.7}$$

where $t^2_{h,k} = max(\Delta t^2, h^2\Delta t, k^2\Delta t)$. Substituting the value of $\tau_{i,j}$ from equation (2.7) in equation (2.2), we obtain the HOC scheme for equation (2.1), which can be written as

$$\begin{aligned}&\left[1 - \frac{D\Delta t}{2}\left(\delta_x^2 + \delta_y^2\right) + \left(\frac{h^2}{12}\delta_x^2 + \frac{k^2}{12}\delta_y^2\right) + \frac{\Delta t}{2} d^n_{i,j}\right]\delta_t^+\psi^n_{i,j} - \frac{D\left(h^2+k^2\right)}{12}\delta_x^2\delta_y^2\psi^n_{i,j}\\ &+ \left(\frac{h^2 d^n_{i,j}}{12} - D\right)\delta_x^2\psi^n_{i,j} + \left(\frac{k^2 d^n_{i,j}}{12} - D\right)\delta_y^2\psi^n_{i,j} + G^n_{ij}\psi^n_{i,j} + \frac{h^2}{6}\delta_x d^n_{i,j}\delta_x\psi^n_{i,j}\\ &+ \frac{k^2}{6}\delta_y d^n_{i,j}\delta_y\psi^n_{i,j} = H^n_{i,j} + O((\Delta t)^2, h^4, k^4), \qquad (2.8)\end{aligned}$$

where

$$H^n_{i,j} = \left(1 + \frac{h^2}{12}\delta_x^2 + \frac{k2}{12}\delta_y^2 + \frac{\Delta t}{2}\delta_t^-\right)F^n_{i,j}, \qquad (2.9)$$

$$G^n_{i,j} = \left(1 + \frac{h^2}{12}\delta_x^2 + \frac{k^2}{12}\delta_y^2 + \frac{\Delta t}{2}\delta_t^-\right)d^n_{i,j}. \qquad (2.10)$$

The operators δ_x, δ_x^2, δ_y, δ_y^2, δ_t^+ and δ_t^- are defined as follows:

$$\begin{aligned}&\delta_x\psi^n_{i,j} = (\psi^n_{i+1,j} - \psi^n_{i-1,j})/(2h),\ \delta_x^2\psi^n_{i,j} = (\psi^n_{i+1,j} - 2\psi^n_{i,j} + \psi^n_{i-1,j})/(h^2),\\ &\delta_y\psi^n_{i,j} = (\psi^n_{i,j+1} - \psi^n_{i,j-1})/(2k),\ \delta_y^2\psi^n_{i,j} = (\psi^n_{i,j+1} - 2\psi^n_{i,j} + \psi^n_{i,j-1})/(k^2),\\ &\delta_t^+\psi^n_{i,j} = (\psi^{n+1}_{i,j} - \psi^n_{i,j})/(\Delta t),\ \delta_t^-\psi^n_{i,j} = (\psi^n_{i,j} - \psi^{n-1}_{i,j})/(\Delta t).\end{aligned}$$

It is clear from equation (2.8) that this implicit scheme is second order accurate in t and fourth order accurate in both the spatial directions x and y. Note that the implicitness of the scheme is owing to the coefficient of $\delta_t^+\psi^n_{i,j}$ in the left hand side of the equation (2.8). The scheme (2.8) can be compactly written as

$$\sum_{K=-1}^{K=1}\sum_{K'=-1}^{K'=1} R_{i+K,j+K'}\psi^{n+1}_{i+K,j+K'} = \sum_{r=-1}^{r=1}\sum_{r'=-1}^{r'=1} R'_{i+r,j+r'}\psi^n_{i+r,j+r'} + \Delta t H^n_{i,j} \qquad (2.11)$$

where K, K', r r' are integers and at least one of K or K' is nonzero and the coefficients are given by:

$$R_{i\pm1,j} = \left(\frac{1}{12} - \frac{D\Delta t}{2h^2}\right),\ R_{i,j\pm1} = \left(\frac{1}{12} - \frac{D\Delta t}{2k^2}\right),\ R_{i,j} = \frac{2}{3} + D\Delta t\left(\frac{1}{h^2} + \frac{1}{k^2}\right) + \frac{\Delta t}{2}c_{i,j}, \qquad (2.12)$$

$$R'_{i\pm1,j\pm1} = D\Delta t\left[\frac{1}{h^2} + \frac{1}{k^2}\right],\ R'_{i,j} = \Delta t\left[-\frac{5D}{3h^2} - \frac{5D}{3h^2} + \frac{c^n_{i,j}}{3} - G^n_{i,j}\right] + R_{i,j}, \qquad (2.13)$$

$$R'_{i\pm1,j} = R_{i\pm1,j} + \Delta t\left[\frac{5D}{6h^2} - \frac{D}{6k^2} - \frac{c^n_{i,j}}{12} \pm \frac{1}{24}\left(c^n_{i+1,j} - c^n_{i-1,j}\right)\right], \qquad (2.14)$$

$$R'_{i,j\pm1} = R_{i,j\pm1} + \Delta t\left[\frac{5D}{6k^2} - \frac{D}{6h^2} - \frac{c^n_{i,j}}{12} \pm \frac{1}{24}\left(c^n_{i,j+1} - c^n_{i,j-1}\right)\right]. \tag{2.15}$$

The HOC scheme (2.11) uses nine points at the $(n)^{th}$ and only five points at the $(n+1)^{th}$ time level and as such is termed as a $(5,9)$ scheme. The finite difference scheme (2.11) can be easily verified to be unconditionally stable as in [53]. Equation (2.11) can be written in the matrix form as

$$A\psi^{n+1} = H(\psi^n), \tag{2.16}$$

where the coefficient matrix A is a pentadiagonal sparse matrix of dimensions $mn \times mn$ for grid size $m \times n$, whereas ψ^{n+1} and $H(\psi^n)$ are mn component vectors.

It is important to mention that, we perform all of our computations for the models of 2D excitable media exploiting the HOC scheme (2.11) by rewriting the equation (2.1) in the following form,

$$\frac{\partial\psi}{\partial t} = D(\frac{\partial^2\psi}{\partial x^2} + \frac{\partial^2\psi}{\partial y^2}) + F(u,v), \tag{2.17}$$

so that the coefficients $R_{i-1,j}$, $R_{i+1,j}$, $R_{i,j-1}$, $R_{i,j+1}$ and R_{ij} become constant for given values of D, h, k and Δt. Now it is clear from equation (2.12) that the matrix A is diagonally dominant and hence a unique solution for equation (2.16) exists. For solving the matrix equation (2.16), we have used an efficient BiCGStab [59] iterative method, which constitutes the inner iterations for each outer time step. All our computations were performed on an Intel Xeon Server E3-1280@3.9GHertz with 16GB RAM.

भारतीय प्रौद्योगिकी संस्थान गुवाहाटी • Indian Institute of Technology Guwahati •

Chapter 3

HOC SIMULATION OF THE MODELS OF EXCITABLE MEDIA

3.1 Introduction

There has been a lot of development in numerical studies on the spiral wave patterns in excitable media using the Barkley [9] and FHN [40] models. However most of earlier numerical results [5, 17, 28, 29, 40, 45, 79] through finite difference approach have been obtained by using Euler's forward time centered difference (FTCS) scheme which has order of accuracy at most two. Owing to their lower order accuracy, simulations resulting from these schemes might not have been able to accurately represent the actual physiological phenomenon. This aspect has been taken care of in the current study through the concept of modified differential equation (MDE) of the explicit scheme. Also, very few works can be seen in the existing literature on the use of HOC scheme [53, 63, 102] for such studies. This chapter endeavours to perform numerical simulations of pattern formation in 2D excitable media exploiting the Barkley and FHN models through the reconstructed HOC scheme in chapter 2 with appropriate boundary conditions. Moreover, in order to establish the efficiency of our reconstructed HOC scheme given by equation (2.8) for the aforesaid models of excitable media, we also perform convergence and grid independence analysis of the computed data. Further, we illustrate the results obtained from both explicit and

---

Some part of this chapter is published in [49].
Some part of this chapter is under review [47].

TH-2268_136123014

HOC schemes and compare them, pinpointing the deficiencies of Euler's Explicit scheme and substantiating how our reconstructed HOC scheme has been able to overcome them.

It is worth mentioning that most of the models of pattern formations in excitable media are studied by employing zero-flux boundary conditions [9, 40, 45]. However, periodic boundary conditions also play a vital role in the field of pattern formations, as seen by [30], who explored the possibility of spiral wave break up by imparting periodic boundary conditions on square computational domains. In 2007, Shen *et. al.* [100] simulated strip like pattern structures by solving a system of reaction-diffusion systems with periodic boundary conditions. Similar studies were carried out in 2017 by Yuri *et. al.* [106] by making use of a diffusion model through a lattice method. They concluded that when periodic boundary conditions are imposed on both directions of the square lattice, the system tends to a steady state resulting in diagonal stripe patterns; on the other hand imposing periodic boundary conditions along only one direction resulted in unstable stripes and a change in their spatial orientation. As such, accurate numerical implementation of them is very crucial for obtaining physically meaningful simulation of the pattern formation. Continuing in the same vein, we have derived a fourth order accurate finite difference approximations for periodic boundary conditions based on the parent HOC scheme given by equation (2.8). With the aid of the proposed algorithm, we simulate patterns in excitable media by solving a system of R-D equations. In the process, we also compare the effect of periodic and zero-flux boundary conditions on the evolution of the spiral wave patterns.

3.2 Simulations of patterns through Barkley model

3.2.1 Code validation

The famous Barkley model [9] which govern the movement of the spiral waves in 2D excitable media is given by

$$\frac{\partial u}{\partial t} = \frac{1}{\epsilon} u\,(1-u)\left(u - \frac{b+v}{a}\right) + D_u \nabla^2 u, \tag{3.1}$$

$$\frac{\partial v}{\partial t} = u - v + D_v \nabla^2 v, \tag{3.2}$$

where a and b are the parameters controlling the threshold and duration of excitability. Note that while a larger value of a enhances the duration of the excitable variable, a larger value of the ratio $\frac{b}{a}$ aids an increase in the excitation threshold [63, 101]. Throughout the course of the current study, the values of parameters a, b and ϵ are chosen in such a way that they adhere to the range found in [8], where spiral wave patterns are feasible.

Numerical computations are performed on a square domain $[-30, 30] \times [-30, 30]$ on grids of sizes 121×121, 241×241, 481×481 and 961×961 for a duration of $t = 8.0$ with temporal step length $\Delta t = 0.001$. The parameter values chosen are: $D_u = 1.0$, $D_v = 0$, $\epsilon = 0.005$, $a = 0.3$ and $b = 0.01$. The parameter values and the final time are chosen as such in order to compare our results with the recent simulations of [25]. No-flux conditions are employed for both the variables u and v at all the boundaries and the initial conditions are as in [25], which can written as,

$$u(x, y, 0) = \begin{cases} 0.0, & \text{if } x < 0 \cup y > 5 \\ (1 + exp(4(|x|-5)))^{-2} - (1 + exp(4(|x|-1)))^{-2}, & \forall y \quad otherwise \end{cases} \tag{3.3}$$

$$v(x, y, 0) = \begin{cases} 0.1, & \text{if } x < 1 \cap y < 10 \\ 0, & \text{otherwise.} \end{cases} \tag{3.4}$$

Before embarking on simulating the wave patterns in excitable media for the purpose of studying the dynamics of waves simulated through various models as would be seen in the subsequent chapters, we validate our code by comparing our results with available benchmark results and establishing the grid-independence of the obtained solutions. In the process, we also establish the theoretical rate of convergence of the reconstructed scheme of chapter 2.

Table 3.1: The CPU time to reach time $t = 8.00$ on different grid sizes.

Grid Size	121×121	241×241	481×481	961×961
Time (in sec)	10.544	46.736	244.292	1421.023

In figure 3.1(a), we present the values of u along the vertical centerline (i.e. $x = 0$ and $-30 \leq y \leq 30$) at time $t = 8.0$ on grids of size 121×121, 241×241, 481×481 and 961×961.

The CPU times to reach the final time used in this computation on those grids are presented in table 3.1. The corresponding contours for $u = 0.5$ are depicted in figure 3.1(b). The overlapping of the graphs on grid of sizes 481×481 and 961×961 on these figures clearly establishes the grid independence of our computed data on a grid of size 481×481.

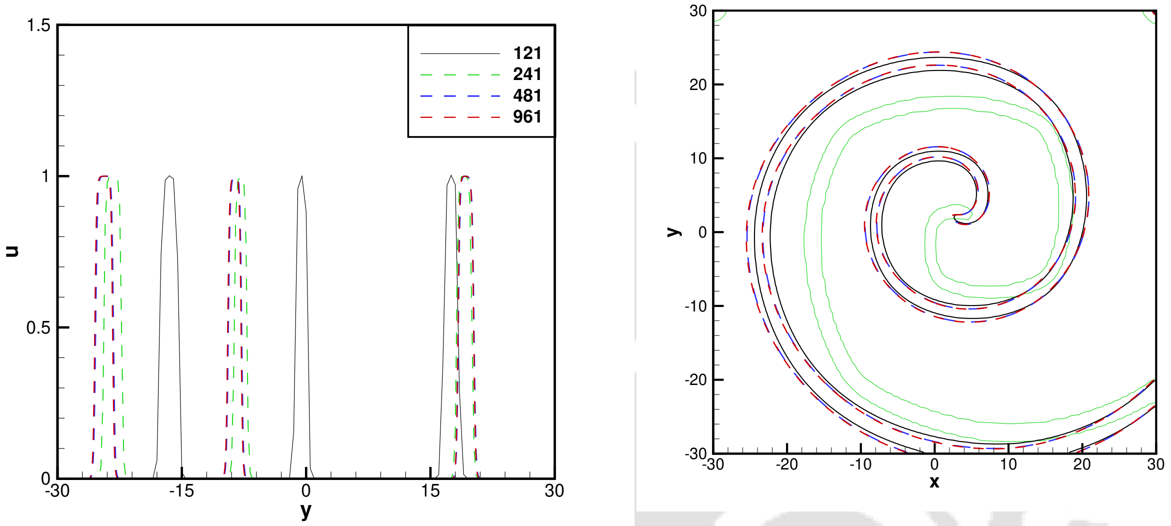

(a)

(b)

Figure 3.1: (a) Plots of u vs y $(-30 \leq y \leq 30)$ at $x = 0$ and (b) contour plots for $u = 0.5$ on different grid sizes 121×121 (green), 241×241 (black), 481×481 (blue) and 961×961 (red). All at time $t = 8.0$.

Now in figure 3.2, we depict the patterns obtained from our HOC scheme in the first column and the corresponding figures obtained from the element free Galerkin method based computation for test problem 5 of [25] in second column. The first column in the same figure depicts the contour of u (figure 3.2(a)), contour of v (figure 3.2(c)) and surface plot of u (figure 3.2(e)) on a grid of size 481×481, and in the second column, we present the corresponding figures obtained from the element free Galerkin method based computation for test problem 5 of [25]. From the comparison of figures 3.2(a)-(b), 3.2(c)-(d) and 3.2(e)-(f), one can clearly see that our results are excellent match with the ones obtained in [25].

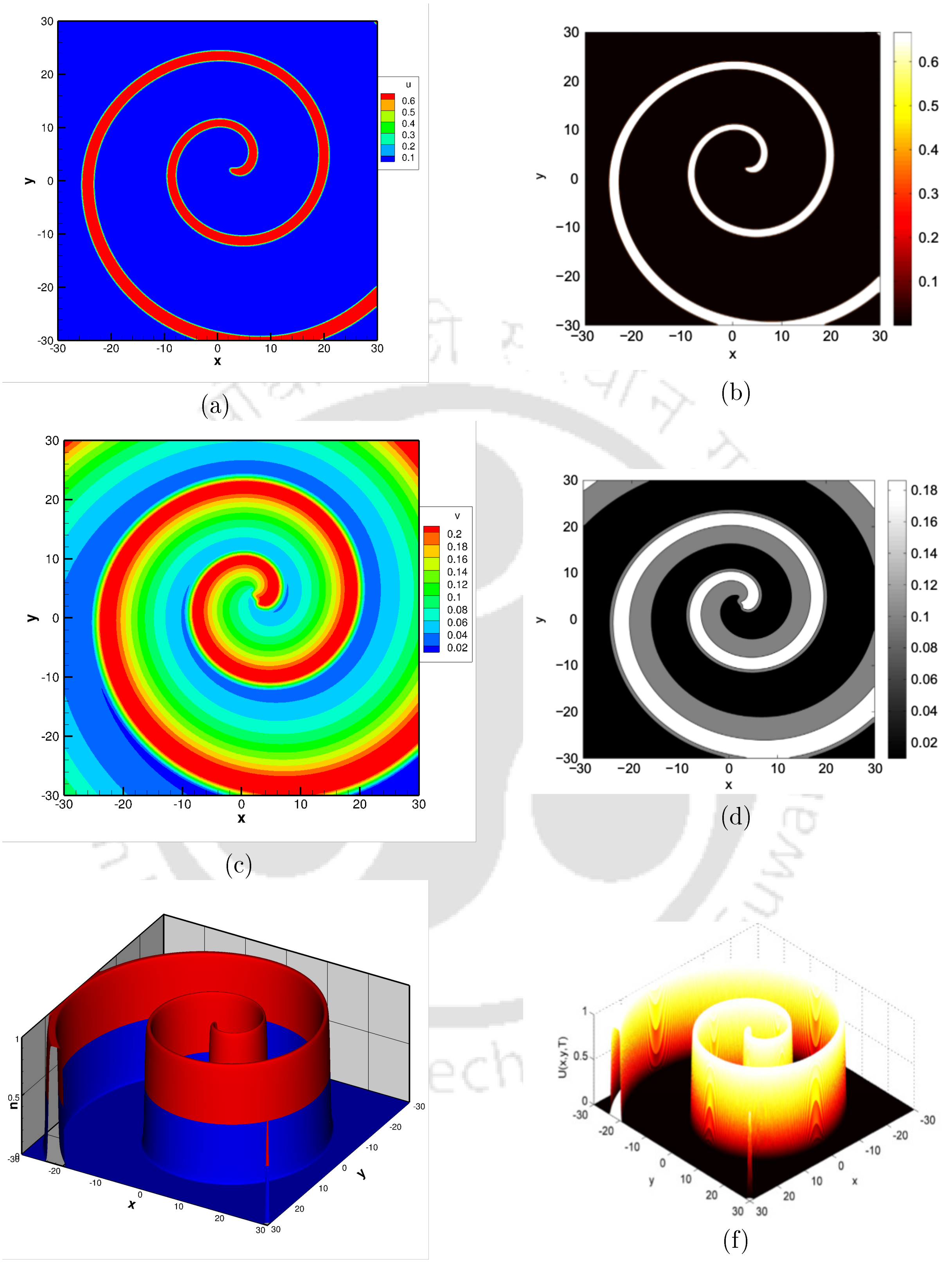

(a) (b) (c) (d) (e) (f)

Figure 3.2: (a)-(b) Contour plots of u, (c)-(d) contour plots of v and (e)-(f) surface plots of u . First column from our HOC computation and second column from [25] and all at time $t = 8.0$.

Next, we compute the rate of convergence of our computed data for equations (3.1)-(3.2) by defining the order of accuracy $O(A)$ as

$$O(A) = \frac{ln(E_c/E_f)}{ln2}, \tag{3.5}$$

where E_f and E_c are the relative errors based on root mean square on a fine and a coarse grid respectively. The coarse grid has half of the numbers of points in each direction than the finer one; and the root mean square (rms) relative error (say E_{rms}) can be defined as

$$E_{rms} = \frac{rms(\psi_{ana} - \psi_{num})}{rms(\psi_{ana})}. \tag{3.6}$$

Here $rms(\psi_{ana} - \psi_{num})$ is the root mean square value of the pairwise differences of the analytical and numerical solutions computed at each grid point, whereas $rms(\psi)$ is defined by

$$rms(\psi) = \sqrt{\sum_{i=0}^{i=K} \frac{{\psi_i}^2}{K}}, \tag{3.7}$$

where K is the total number of nodes.

Note that owing to the presence of the highly nonlinear reaction terms, the system of equations (3.1)-(3.2) does not possess an analytical solution. It is a common practice in the existing leterature to treat the computed solution in the finest grid as the referenced analytical solution (for example, [24,63]). In line with the same practice, we have considered the numerical solution obtained on the finest grid, viz., 961 × 961 as the analytical solution.

Further, we also exploit the method described in [72,81], where the perceived order of convergence has been defined as

$$O(A) = \frac{ln((\psi_M - \psi_C)/(\psi_F - \psi_M))}{ln2}. \tag{3.8}$$

Here ψ_F, ψ_M and ψ_C are the solutions on three successive grids with each ψ_M and ψ_C having half the number of grid points than their preceding grids in either directions. In the present case, they correspond to grid of sizes 961 × 961, 481 × 481 and 241 × 241 respectively. In tables 3.2 and 3.3, we present the convergence rates obtained through the methods given by equations (3.5) and (3.8) respectively. Both the methods predicts similar rate of convergence for both the variables and the errors are seen to decay slightly slower than the theoretical rate of convergence. It may be noted that the rate of convergence is problem dependent [24, 52] and ours is comparable with some of the test cases for similar problems in [24]. For example, on solving two-dimensional Brusselator reaction-diffusion system by discontinuous Galerkin methods, the convergence orders on finest grids used for test problem 1 in [24] were found to be 3.5994 and 3.6367 for u and v respectively (see Table 4, section 6.1 in [24]).

Table 3.2: Rate of convergence of the HOC scheme through method given by (3.5): root mean square (rms) relative error.

Variable	**Error rms** (241×241)	**Error rms** (481×481)	**Rate**
u	5.99765×10^{-1}	6.419185×10^{-2}	3.22
v	1.67565×10^{-1}	1.459007×10^{-2}	3.52

Table 3.3: Rate of convergence of the HOC scheme through method described by (3.8): root mean square (rms) relative error.

Variable	(241×241) **vs** (481×481)	(481×481) **vs** (961×961)	**Rate**
u	5.747642×10^{-1}	6.419185×10^{-2}	3.16
v	1.581713×10^{-1}	1.459007×10^{-2}	3.44

Now, we proceed to examine the betterment of our reconstructed HOC scheme over the explicit scheme. In order to do this, we first derive the MDE for the explicit scheme in the following section.

3.2.2 An analysis of the Modified Differential Equation (MDE)

The explicit finite difference scheme for equations (3.1) and (3.2) can be written as

$$u_{i,j}^{n+1} = u_{i,j}^{n} + \frac{\Delta t}{\epsilon} u_{i,j}^{n}\left(1 - u_{i,j}^{n}\right)\left(u_{i,j}^{n} - \frac{(v_{i,j}^{n} + b)}{a}\right) + \frac{\Delta t D_u}{h^2}\left(u_{i+1,j}^{n} - 2u_{i,j}^{n} + u_{i-1,j}^{n}\right)$$
$$+ \frac{\Delta t D_u}{h^2}\left(u_{i,j+1}^{n} - 2u_{i,j}^{n} + u_{i,j-1}^{n}\right), \tag{3.9}$$

$$v_{i,j}^{n+1} = (1 - \Delta t) v_{i,j}^{n} + \Delta t u_{i,j}^{n}, \tag{3.10}$$

where $u_{i,j}^{n+1}$ and $u_{i,j}^{n}$ denote the value of u at (x_i, y_j) at $(n+1)^{th}$ and n^{th} time levels respectively. *Expressing each term in the finite difference equation by a Taylor series at a particular base point, after simplification, we arrive at the so called modified differential equation (MDE) which is a partial differential equation (PDE) of infinite order.* The MDE also has the added advantage of explicitly extracting the truncation error and verifying the consistency of a finite difference equation. Note that the finite difference solution is actually the exact solution of the MDE. As such the physical phenomena exhibited by the numerical solution are in fact from one which would have arisen from a situation that has been mathematically modeled by the MDE [44].

The explicit schemes given by equations (3.9)-(3.10) are temporally first order and spatially second order accurate. It would be seen later that the spiral patterns generated by using the explicit method even on relatively finer grids do not actually match with the ones created in the laboratory experiments. Therefore, in order to provide an analytical explanation, we derive the MDE for the explicit scheme of 1D version of equation (3.1):

$$\frac{\partial u}{\partial t} = \frac{1}{\epsilon} u\left(1-u\right)\left(u - \frac{v+b}{a}\right) + D_u \frac{\partial^2 u}{\partial x^2}. \tag{3.11}$$

The FTCS discretization of the above results in

$$u_i^{n+1} = u_i^n + \frac{\Delta t}{\epsilon} u_i^n\left(1-u_i^n\right)\left(u_i^n - \frac{(v_i^n+b)}{a}\right) + \frac{\Delta t D_u}{h^2}\left(u_{i+1}^n - 2u_i^n + u_{i-1}^n\right). \tag{3.12}$$

Now we use Taylor's series expansion at the grid point (i, n) for each of the terms of equation (3.12) to yield

$$u_i^{n+1} = u_i^n + \sum_{k=1}\left[\frac{(\Delta t)^k}{k!}\frac{\partial^k u}{\partial t^k}\right]_i^n,\; u_{i+1}^n = u_i^n + \sum_{k=1}\left[\frac{(h)^k}{k!}\frac{\partial^k u}{\partial x^k}\right]_i^n,\; u_{i-1}^n = u_i^n + \sum_{k=1}\left[\frac{(-h)^k}{k!}\frac{\partial^k u}{\partial x^k}\right]_i^n. \tag{3.13}$$

Using the above Taylor's series from equation (3.13) in equation (3.12),

$$\begin{aligned}\left[\frac{\partial u}{\partial t}\right]_i^n - D_u\left[\frac{\partial^2 u}{\partial x^2}\right]_i^n - f_i^n = {} & \frac{D_u h^2}{12}\left[\frac{\partial^4 u}{\partial x^4}\right]_i^n + \frac{2D_u h^4}{6!}\left[\frac{\partial^6 u}{\partial x^6}\right]_i^n - \frac{\Delta t}{2!}\left[\frac{\partial^2 u}{\partial t^2}\right]_i^n \\ & - \frac{(\Delta t)^2}{3!}\left[\frac{\partial^3 u}{\partial t^3}\right]_i^n + O((\Delta t)^3, h^6),\end{aligned} \tag{3.14}$$

Indian Institute of Technology Guwahati

where $f_i^n = (1/\epsilon)u_i^n\,(1-u_i^n)\,(u_i^n - (v_i^n + b)\,/a)$. Hence MDE of FDE (3.12) is,

$$\begin{aligned}\frac{\partial u}{\partial t} - D_u\frac{\partial^2 u}{\partial x^2} - f = \frac{D_u h^2}{12}\left[\frac{\partial^4 u}{\partial x^4}\right] + \frac{2D_u h^4}{6!}\frac{\partial^6 u}{\partial x^6} - \frac{\Delta t}{2}\left[\frac{\partial^2 u}{\partial t^2}\right] - \frac{(\Delta t)^2}{3!}\frac{\partial^3 u}{\partial t^3}\\ + O((\Delta t)^3, h^6), \qquad (3.15)\end{aligned}$$

which is the first form of MDE, where $f(u,v) = (1/\epsilon)u\,(1-u)\,(u-(v+b)/a)$ and as Δt , $h \rightarrow 0$, we can retrieve (3.11) from (3.15). The second form of the MDE can be obtained by replacing $\partial^2 u/\partial t^2$, making use of the first form MDE equation itself. The second form of the MDE is given by

$$\begin{aligned}\frac{\partial u}{\partial t} &= D_u\,(1-\Delta t R_1)\,\frac{\partial^2 u}{\partial x^2} + \left(1 - \frac{\Delta t R_1}{2}\right) f + \left[\frac{D_u h^2}{12} - \frac{D_u^2 \Delta t}{2}\right]\frac{\partial^4 u}{\partial x^4}\\ &- \left[\frac{\Delta t D_u^2 h^2}{12}\right]\frac{\partial^6 u}{\partial x^6} - \frac{D_u \Delta t}{2} R_2\,(u_x)^2 - \frac{\Delta t D_u h^2}{4!}\frac{\partial^4 f}{\partial x^4} + O((\Delta t)^2, h^4), \quad (3.16)\end{aligned}$$

where $R_1 = (1/\epsilon)\,[(1-2u)\,(u-(v+b)/a) + (u-u^2)]$ and $R_2 = (1/\epsilon)\,[2 - 6u + 2(v+b)/a]$.

A close look at the equation (3.16) reveals that apart from retrieving all the terms of the equation (3.11), it contains terms which are primarily dominated by the even order derivatives of u, some form of artificial reaction (see the terms containing R_1 and R_2). Analogous to the implicit numerical diffusion and dispersion, we may term the additional reaction terms in the MDE as an implicit numerical reaction. Therefore, the numerical solutions resulting from the explicit scheme are likely to show non-physical patterns emanating from the extra terms in the MDE as would be seen in the section 3.2.3. Moreover, the lowest order exponentials of Δt and h on the right hand side of equation (3.16) reconfirms the $O(\Delta t, h^2)$ accuracy of the explicit scheme.

3.2.3 Explicit vis a vis HOC simulation

In order to demonstrate how the HOC scheme fares in comparison to the explicit scheme, we solve the system of equations (3.1)-(3.2) with parameter values $D_u = 1.58$, $D_v = 0$, $\epsilon = 0.02$, $a = 0.84$ and $b = 0.07$ on a grid of size 257×257 in the square defined by

$0 \leq x \leq 128, \; 0 \leq y \leq 128$ and the following initial conditions [17]

$$u(x,y,0) = \begin{cases} 0.9, & \text{if } \{60 < x < 61.5\} \cup \{y < 64\} \\ 0.7, & \text{if } \{61 < x < 62.5\} \cup \{y < 64\} \\ 0, & \text{otherwise} \end{cases} \tag{3.17}$$

$$v(x,y,0) = \begin{cases} 0.7, & \text{if } \{61 < x < 62.5\} \cup \{y < 64\} \\ 0.9, & \text{if } \{62 < x < 63.5\} \cup \{y < 64\} \\ 0, & \text{otherwise.} \end{cases} \tag{3.18}$$

In figure 3.3(a), we display the patterns ensuing from the experiments in B-Z reaction [10]. The simulation resulting from the computation employing the current HOC and Euler's explicit schemes at time $t = 300.0$ are presented in figures 3.3(b) and 3.3(c)-(d) respectively. It can be seen from the figure 3.3(c) that the shape of the spiral wave is more squarish than circular while our current HOC simulation (see figure 3.3(b)) was excellent match with the experimental ones even with a time step as large as 0.04. Note that in order to reach the level of resolution achieved by the current HOC simulation, much smaller time and space steps had to be used by the explicit scheme. As one can see from figures 3.3(b) and 3.3(d), in order to match the patterns computed on a grid of size 257×257 with $\Delta t = 0.04$ by the HOC scheme, the explicit scheme required a grid of size 513×513 with $\Delta t = 0.001$. As such the HOC simulation was computationally more efficient than the explicit one. The CPU times to reach the final time $t = 300.0$ by the explicit and HOC schemes corresponding to figures 3.3(d) and 3.3(b) are $444.560s$ and $129.156s$ respectively, a gain of more than 240% of computational time.

3.3 Simulations of patterns through FHN model

Next, we move towards carrying out simulations of 2D pattern formation in excitable media through the FHN model. Contrary to the use of only zero flux boundary condition in the Barkley model, we use both zero-flux and periodic boundary conditions in this model, which in turn, allows us to explore the effect of boundary conditions on the spiral wave dynamics. In order to accomplish this, we firstly derive HOC approximations of

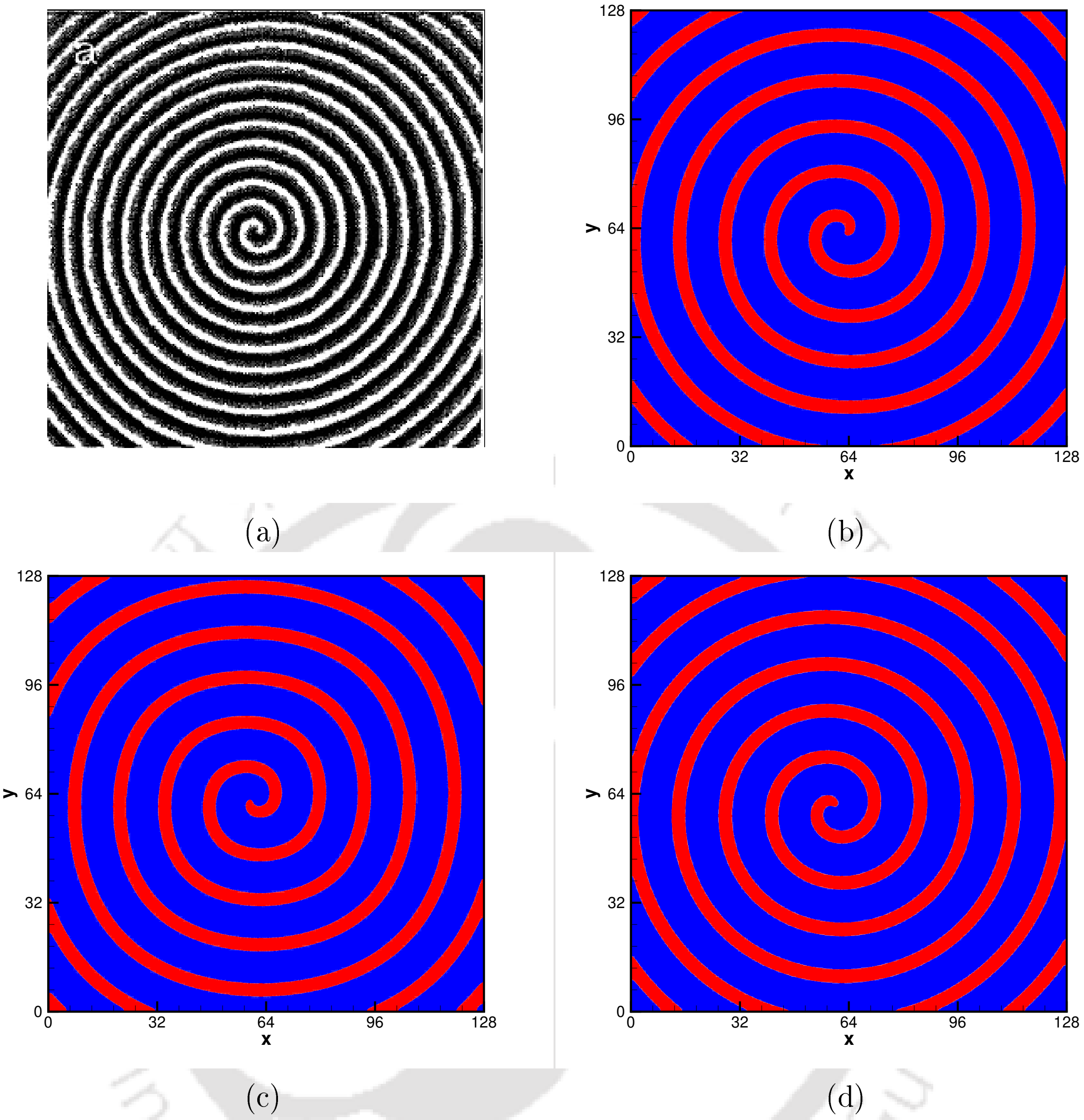

(a) (b) (c) (d)

Figure 3.3: Spiral wave patterns: (a) Experimental from B-Z reaction, [10], (b) $\Delta t = 0.04$ on grid 257×257 by HOC scheme, (c) $\Delta t = 0.001$ on grid 257×257 by explicit scheme and (d) $\Delta t = 0.001$ on grid 513×513 by explicit scheme at time $t = 300$.

the periodic boundary conditions based on the methodology adopted in the parent HOC scheme described by equation (2.11).

3.3.1 An HOC approximation of periodic boundary conditions

Periodic boundary conditions at a point (x, y) on a rectangular domain of length L_x and breadth L_y may be mathematically expressed as

$$\psi(x, y) = \psi(x + L_x, y), \tag{3.19}$$

$$\psi(x,y) = \psi(x,y+L_y). \tag{3.20}$$

Opposed to HOC boundary conditions in Dirichlet or Neumann form [53, 54], the implementation of the HOC scheme at the boundaries are not straight forward as they are periodic in nature. In the following, we discuss the development of HOC approximation for the periodic boundary conditions given by equations (3.19)-(3.20). In solving the systems of equations (2.16) by BiCGStab method, one essentially requires the same number of equations in same number of unknowns. However at the corners and the boundaries, implementing the $(5,9)$ HOC scheme would result in the addition of fictitious points (see figure 3.4). To circumvent this problem, we make use of the periodic boundary conditions as the auxiliary relations in order to substitute for the values of the unknowns at the fictitious points.

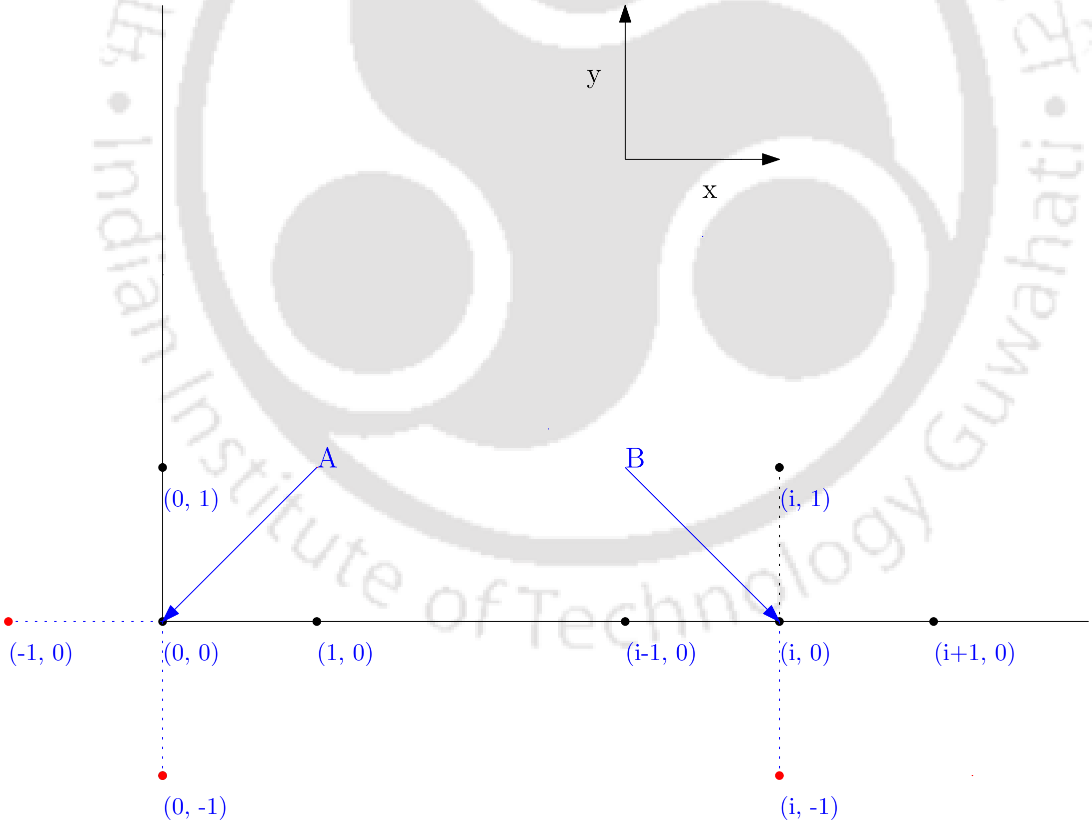

Figure 3.4: Geometric representation of the fictitious points (represented by red dots) at the grid points $(0,0)$ and $(i,0)$.

If the points in x- and y- directions ranges from 0 to i_{max} and 0 to j_{max} respectively, at the bottom left corner grid point *i.e.* $(0,0)^{th}$ the $(5,9)$ HOC scheme 2.11 in ψ would result in

$$a_1\psi^{n+1}_{-1,0} + a_2\psi^{n+1}_{1,0} + a_3\psi^{n+1}_{0,0} + a_4\psi^{n+1}_{0,-1} + a_5\psi^{n+1}_{0,1} = H(\psi^n), \tag{3.21}$$

where $a_1(=R_{i-1,j})$, $a_2(=R_{i+1,j})$, $a_3(=R_{i,j})$, $a_4(=R_{i,j-1})$ and $a_5(=R_{i,j+1})$ are the coefficients as in the left hand side of (2.11). It must be noted that the coefficients a_1, a_2, a_3, a_4 and a_5 are constant for a given space sizes h, k and time step Δt. Note that $\psi^{n+1}_{-1,0}$ and $\psi^{n+1}_{0,-1}$ are fictitious points (see point 'A' in figure 3.4) in equation (3.21), by the periodicity of ψ at the boundaries, we have $\psi^{n+1}_{-1,0} = \psi^{n+1}_{i_{max}-1,0}$ and $\psi^{n+1}_{0,-1} = \psi^{n+1}_{0,j_{max}-1}$; hence (3.21) reduces to

$$a_1\psi^{n+1}_{i_{max}-1,0} + a_2\psi^{n+1}_{1,0} + a_3\psi^{n+1}_{0,0} + a_4\psi^{n+1}_{0,j_{max}-1} + a_5\psi^{n+1}_{0,1} = H(\psi^n). \tag{3.22}$$

Similarly, for other three corner points, precisely $(i_{max},0)$, $(0,j_{max})$ and (i_{max},j_{max}) the $(5,9)$, HOC approximations are given by

$$a_1\psi^{n+1}_{i_{max}-1,0} + a_2\psi^{n+1}_{1,0} + a_3\psi^{n+1}_{i_{max},0} + a_4\psi^{n+1}_{i_{max},j_{max}-1} + a_5\psi^{n+1}_{i_{max},1} = H(\psi^n), \tag{3.23}$$

$$a_1\psi^{n+1}_{i_{max}-1,j_{max}} + a_2\psi^{n+1}_{1,j_{max}} + a_3\psi^{n+1}_{0,j_{max}} + a_4\psi^{n+1}_{0,j_{max}-1} + a_5\psi^{n+1}_{0,1} = H(\psi^n), \tag{3.24}$$

$$a_1\psi^{n+1}_{i_{max}-1,j_{max}} + a_2\psi^{n+1}_{1,j_{max}} + a_3\psi^{n+1}_{i_{max},j_{max}} + a_4\psi^{n+1}_{i_{max},j_{max}-1} + a_5\psi^{n+1}_{i_{max},1} = H(\psi^n). \tag{3.25}$$

Now at the bottom boundary excluding the end points, the $(5,9)$ HOC scheme (2.8) would result in

$$a_1\psi^{n+1}_{i-1,0} + a_2\psi^{n+1}_{i+1,0} + a_3\psi^{n+1}_{i,0} + a_4\psi^{n+1}_{i,-1} + a_5\psi^{n+1}_{i,1} = H(\psi^n) \tag{3.26}$$

Note that $\psi^{n+1}_{i,-1}$ (see point 'B' in figure 3.4) for $i = 1,2,\ldots,i_{max}-1$ are the fictitious points in (3.26), by the periodicity of ψ at the boundaries, we have $\psi^{n+1}_{i,-1} = \psi^{n+1}_{i,j_{max}-1}$ for $i = 1,2,\ldots,i_{max}-1$, hence (3.26) becomes,

$$a_1\psi^{n+1}_{i-1,0} + a_2\psi^{n+1}_{i+1,0} + a_3\psi^{n+1}_{i,0} + a_4\psi^{n+1}_{i,j_{max}-1} + a_5\psi^{n+1}_{i,1} = H(\psi^n) \tag{3.27}$$

Similarly, for the left, right and top boundaries excluding the corner points the $(5,9)$ HOC schemes are given by

$$a_1\psi^{n+1}_{i_{max}-1,j} + a_2\psi^{n+1}_{1,j} + a_3\psi^{n+1}_{0,j} + a_4\psi^{n+1}_{0,j-1} + a_5\psi^{n+1}_{0,j+1} = H(\psi^n) \tag{3.28}$$

$$a_1\psi^{n+1}_{i_{max}-1,j} + a_2\psi^{n+1}_{1,j} + a_3\psi^{n+1}_{i_{max},j} + a_4\psi^{n+1}_{i_{max},j-1} + a_5\psi^{n+1}_{i_{max},j+1} = H(\psi^n) \tag{3.29}$$

$$a_1\psi^{n+1}_{i-1,j_{max}} + a_2\psi^{n+1}_{i+1,j_{max}} + a_3\psi^{n+1}_{i,j_{max}} + a_4\psi^{n+1}_{i,j_{max}-1} + a_5\psi^{n+1}_{i,1} = H(\psi^n) \tag{3.30}$$

Note that the development of HOC approximations of the periodic boundary conditions as described above could be very useful in other fields of computational physics also. One may cite the field of computational fluid dynamics where periodic boundary conditions occur in many complex flow situations; for example, in the flow past circular cylinder problem, if a circular annulus is used as a physical domain in the (r, θ) plane, in order to maintain continuity of the solution, one must employ periodic boundary conditions at points corresponding to $\theta = 0^o$ and 360^o [51, 57].

3.3.2 Numerical results

Now we embark on implementing the reconstructed HOC scheme for simulating excitable media governed by the FHN [21,34] equations. In the process, we also employ the proposed HOC approximation of the periodic boundary conditions as well as the zero-flux one, which has been widely used to explore the qualitative behaviour of many excitable media such as B-Z reaction and cardiac tissues. The model is given by

$$\frac{\partial u}{\partial t} = \frac{1}{\epsilon}cu(u-a)(1-u) + D_u\left(\frac{\partial^2 u}{\partial x^2} + \frac{\partial^2 u}{\partial y^2}\right), \tag{3.31}$$

$$\frac{\partial v}{\partial t} = u - dv + D_v\left(\frac{\partial^2 v}{\partial x^2} + \frac{\partial^2 v}{\partial y^2}\right), \tag{3.32}$$

where a, c, d and ϵ are the positive parameters. Computations are performed on a square domain of size $[-20, 20] \times [-20, 20]$ in the two dimensional xy-plane. The parameter values are chosen as: $c = 1$, $a = 0.5$, $d = 1$, $\epsilon = 0.005$, $D_u = 1$ and $D_v = 0$ and the initial conditions is given by:

$$u(x,y,0) = \begin{cases} \dfrac{1}{(1 + exp\,(4\,(\mid x \mid -5)))^2} - \dfrac{1}{(1 + exp\,(4\,(\mid x \mid -5)))^2}, & \text{if } \{x < 1\} \cup \{y > 5\} \\ 0, & \text{otherwise} \end{cases} \tag{3.33}$$

$$v(x,y,0) = \begin{cases} 0.15, & \text{if } \{x < 1\} \cap \{y < -10\} \\ 0, & \text{otherwise} \end{cases} \tag{3.34}$$

First, we solve the system (3.31)-(3.32) with periodic boundaries conditions on a grid of size 201×201; the grid size and computational domain are chosen so as to match the results of [21]. The time step for all numerical computations is fixed at $\Delta t = 10^{-4}$.

In order to demonstrate the grid independence of our results, we compare our computed values of u along the vertical line $x = 0$ at time $t = 10.0$ on grid of size 201×201, 401×401, 601×601 and 801×801 in figure 3.5. While 3.5(b) depicts the results for the periodic boundary condition, the same for zero-flux boundary condition is depicted in 3.5(a). From both the figures it is clear that grid-independence is achieved on a grid of size 401×401.

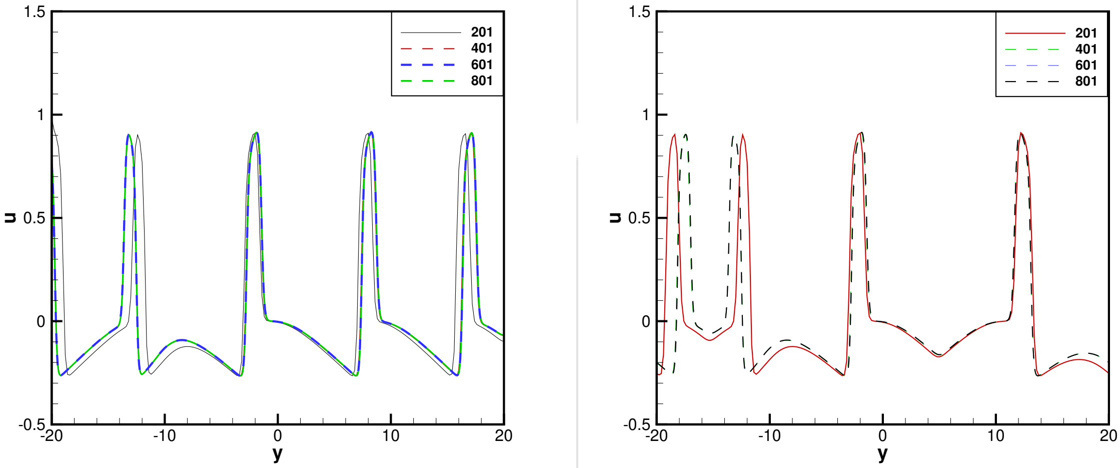

(a) (b)

Figure 3.5: Plots of u along a vertical line $-20 \leq y \leq 20$ for a fixed value of $x = 0$ at $t = 10.0$ with both boundary conditions: (a) zero flux (b) periodic.

Next, we present the pattern formations resulting from our numerical simulations with periodic boundary condition and compare them with the ones obtained the standard explicit scheme and those of [21]. Three time stations, namely $t = 2.0$, 5.0 and 10.0 are chosen for this purpose. The top, middle and bottom rows of figure 3.6 depict the results of [21], the current computations and the explicit scheme respectively. It is clear from figures 3.6(a1-a3) and 3.6(b1-b3) that our results are excellent match with those of [21]. One can see from figure 3.6(c1-c3) that at larger times, the patterns obtained from the lower order explicit scheme is deviating from the ones obtained from the higher order ones.

The reason for this could be the presence of implicit numerical diffusions and dispersions that are inherent to the explicit scheme discussed in section 3.2.2.

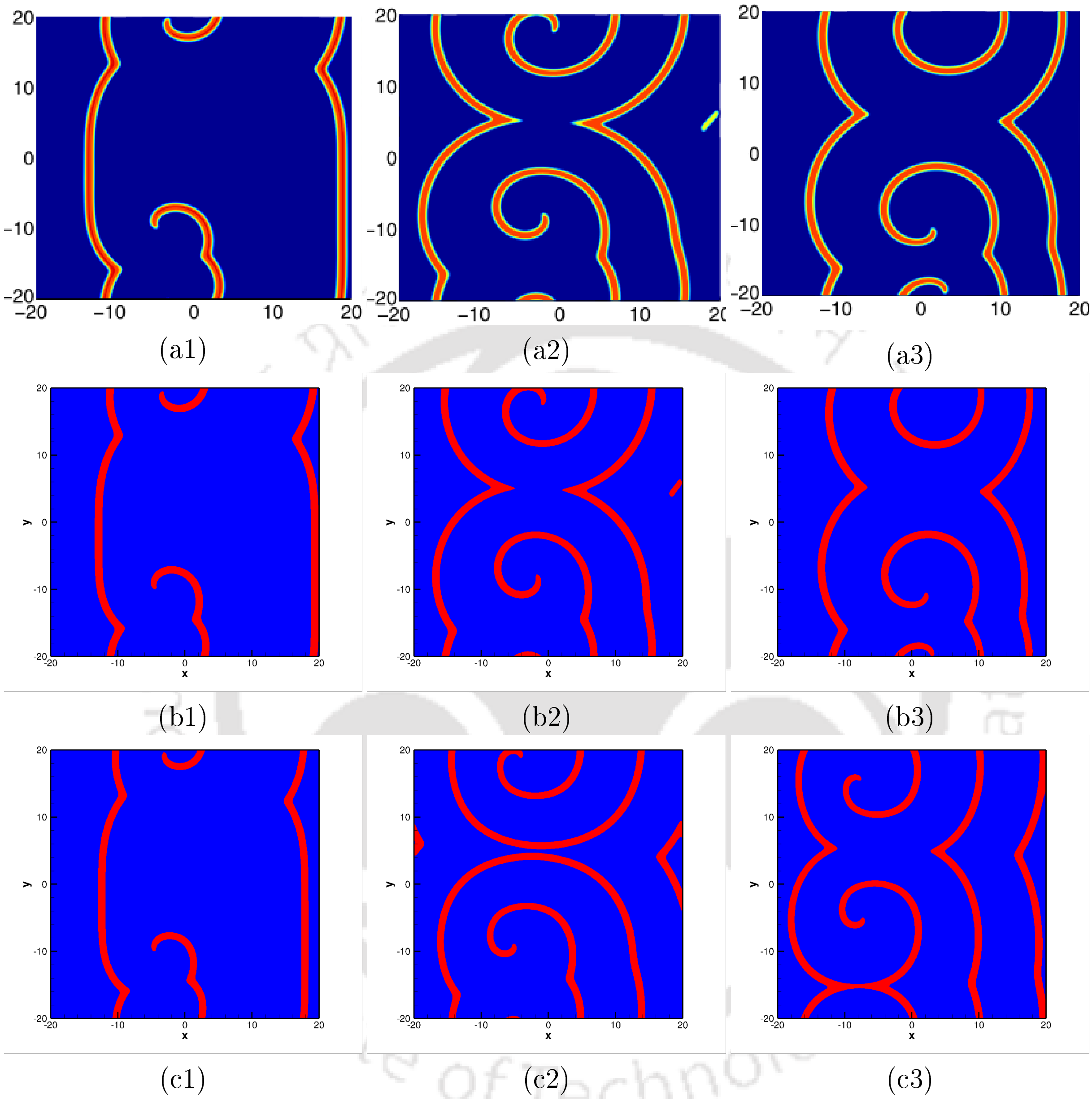

(a1) (a2) (a3)

(b1) (b2) (b3)

(c1) (c2) (c3)

Figure 3.6: Spiral wave patterns with periodic boundary conditions at times $t = 2$ (left), 5 (middle) and 10 (right): (a) from the scheme of [21], (b) from our HOC computation and (c) explicit scheme.

Now we compute the solutions of the system (3.31)-(3.32) with zero-flux boundary conditions by our reconstructed HOC scheme, keeping all the other parameters values in tact as in the periodic boundary condition case. We illustrate the evolution of the patterns during time $2 \leq t \leq 70$ in figures 3.7(a)-(f). One can clearly see from these figures that there is no break up in the spiral wave patterns which is evident even during the later stages of simulations obtained with the periodic boundary conditions (see figures 3.8(a)-(c)).

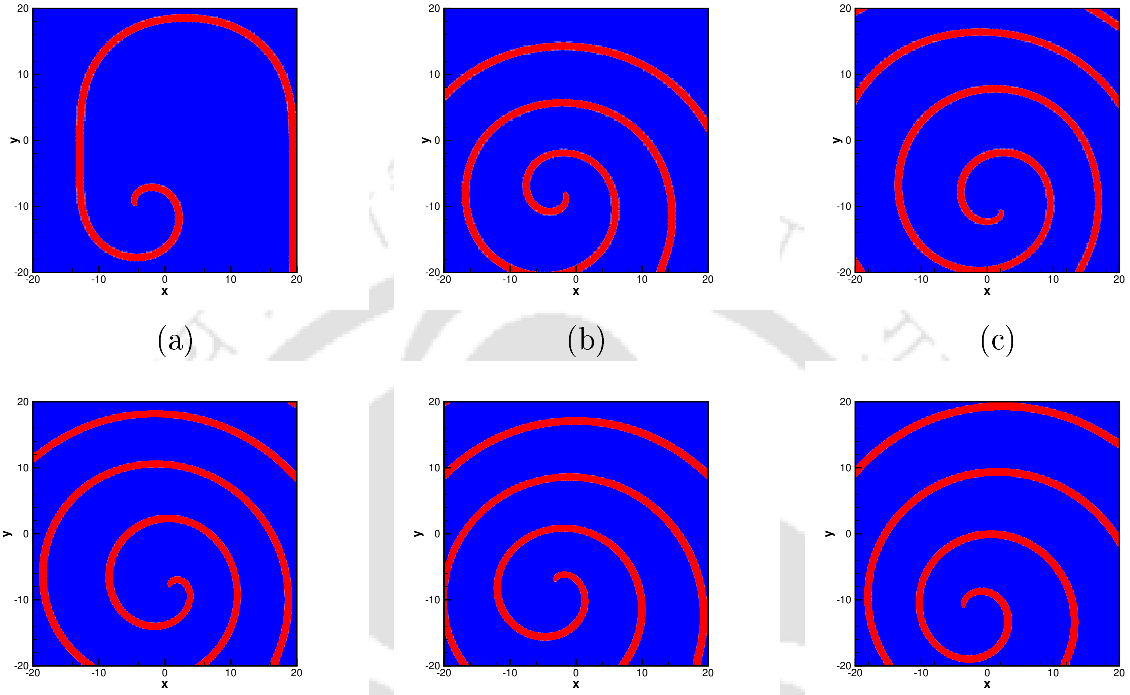

(a) (b) (c)

(d) (e) (f)

Figure 3.7: Evolution of spiral wave patterns with zero-flux boundary conditions: (a) $t = 2.0$, (b) $t = 5.0$, (c) $t = 10.0$, (d) $t = 50.0$, (e) $t = 60.0$ and (f) $t = 70.0$ ((a)-(c) grid size 201×201 and (d)-(f) on 401×401).

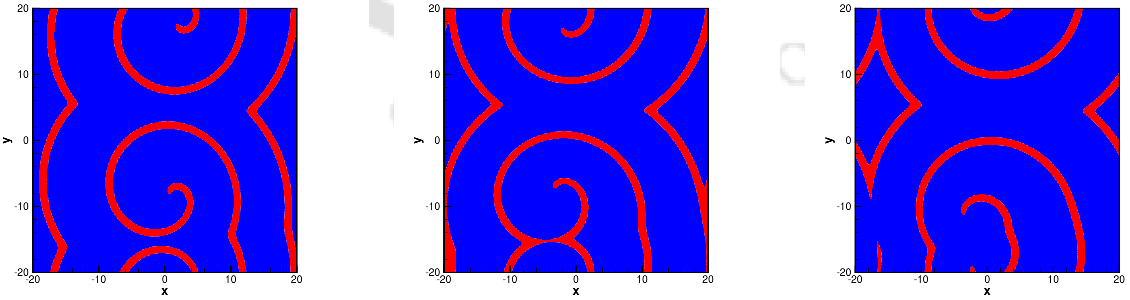

(a) (b) (c)

Figure 3.8: Spiral wave patterns with periodic boundary conditions at different times: (a) $t = 50.0$, (b) $t = 60.0$ and (c) $t = 70.0$ (on grid of size 401×401).

In figures 3.9(a)-(i), we show the evolution of the spiral waves at later stages demonstrating their break-up and merging at different locations of the domain. In figure 3.9(a), one can see two bigger waves approaching each other in the neighborhood of the line $y = 5.0$ around $x = 0.0$ at time $t = 70.60$, they are seen to merge with each other at time $t = 70.70$ (figure 3.9(b)) and then break again at time $t = 70.75$ (figure 3.9(c)). While these bigger waves are breaking apart further at subsequent times, the smaller waves at the bottom of the domain around $(x, y) = (0.0, -15.0)$ are seen to approach, merge and then break at times $t = 71.10$, 71.20 and 71.30 respectively as in figures 3.9(d)-(f). Interestingly at a much later time, one can see the merging and breaking-up of both the bigger and smaller waves simultaneously (figures 3.9(g)-(i)).

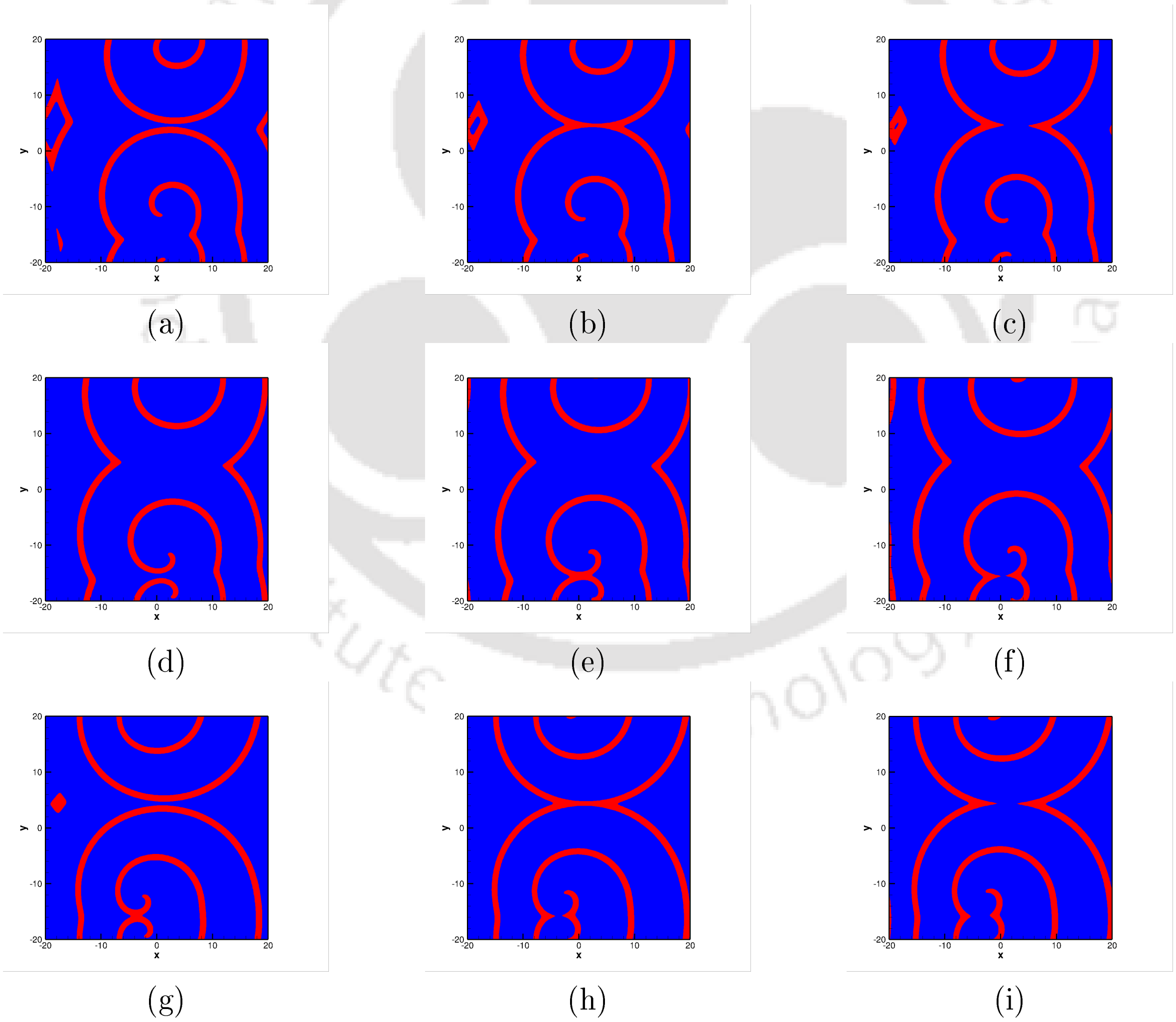

(a) (b) (c)

(d) (e) (f)

(g) (h) (i)

Figure 3.9: Breaking and merging of spiral wave patterns with periodic boundary conditions at later stages:(a) $t = 70.60$, (b) $t = 70.70$,(c) $t = 70.75$, (d) $t = 71.10$, (e) $t = 71.20$, (f) $t = 71.30$, (g) $t = 90.90$, (h) $t = 91.05$ and (i) $t = 91.10$.

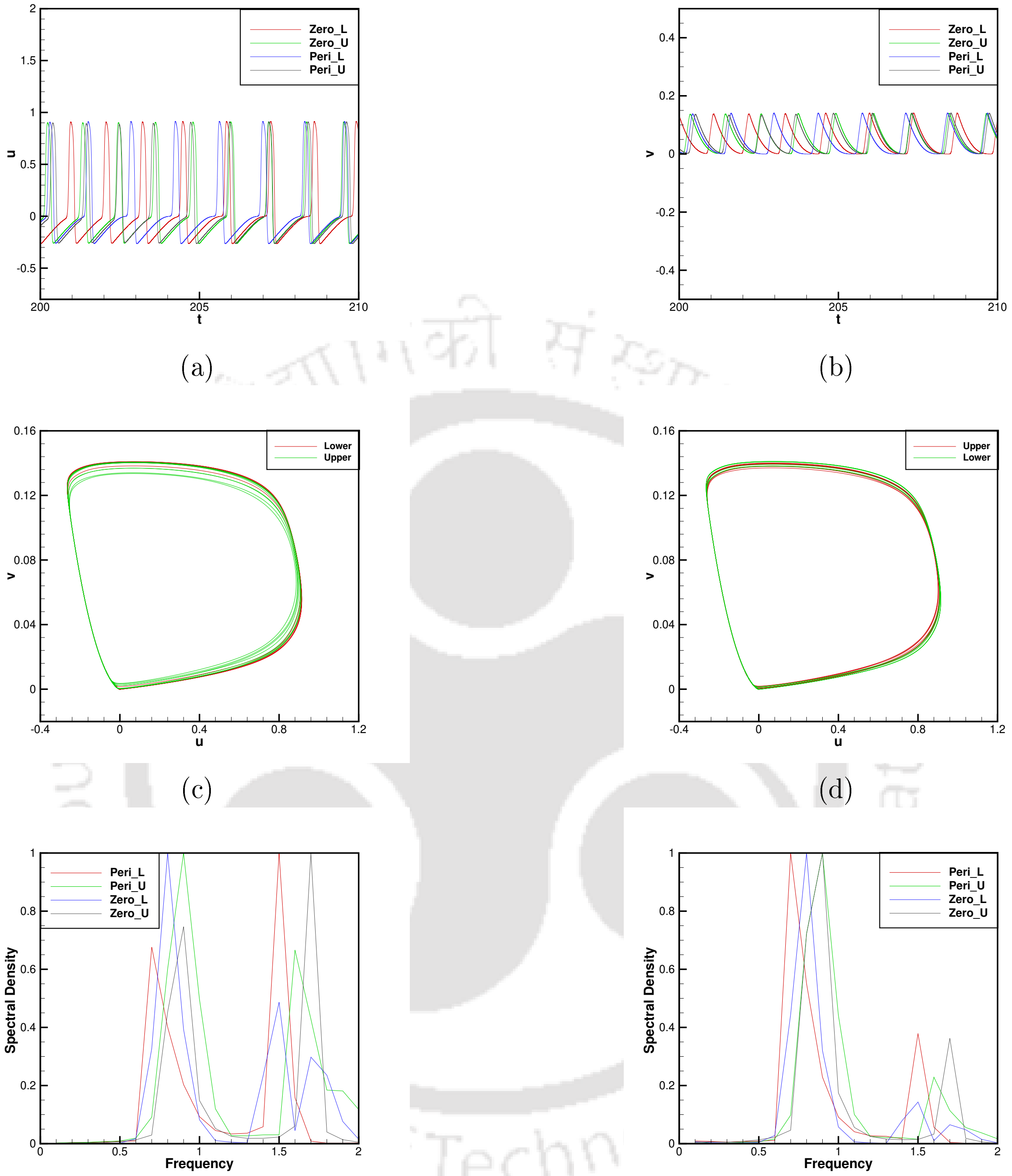

(a) (b)

(c) (d)

(e) (f)

Figure 3.10: (a)-(b Time history of plots of u and v respectively, monitored at locations $(0, -10)$ (Lower) and $(0, 10)$ (Upper) in the range $200 \leq t \leq 210$, (c)-(d) phase diagrams corresponding to periodic and zero flux boundary conditions respectively, and (e)-(f) power spectra plots corresponding to u and v respectively.

In figure 3.10(a)-(b), we plot the time histories of u and v respectively, monitored at two locations $(0, -10)$ and $(0, 10)$ in the lower and upper parts of the solution domain

TH-2268_136123014

computed by employing both zero-flux and periodic boundary conditions in the time interval $200 \leq t \leq 210$. The corresponding phase plots and the power spectra are presented in figures 3.10(c)-(d) and 3.10(e)-(f) respectively. One can clearly see a quasi-periodic nature of the solutions emerging out of the figures. The power-spectra analysis in figures 3.10(e)-(f) clearly indicates the existence of more than one dominant modes. The above set of observations is a clear demonstration of the fact that by invoking periodic boundary conditions, one can make the spiral waves break [30] and merge, and repeat the phenomenon at certain intervals of time.

3.4 Conclusion

In the current chapter, an already existing unconditionally stable, $O(h^4, (\Delta t)^2)$ implicit HOC scheme has been reconstructed to simulate the wave patterns resulting from the well known Barkley and FHN models in 2D excitable media with zero flux and periodic boundary conditions. In the process, we have also derived a fourth order accurate approximations to the periodic boundary conditions which has the potential to be employed in other fields of computational physics as well. Then, we have investigated the effect of the periodic boundary conditions vis a vis the zero-flux one and observed that the role of such boundary conditions is to inflict spiral wave break-up against the regular spiral wave patterns seen with the zero-flux boundary conditions. Moreover our numerical results are found to be grid independent and the patterns resulting from the newly proposed algorithm is found to be very close to the available numerical results. We have further compared our simulated spiral wave patterns with the ones obtained from the Euler's explicit scheme and our results were found to be more closer to the experimental and the available benchmark results. The discrepancies of explicit scheme results with experimental ones have been explained through the concept of the implicit reaction, dispersion and diffusion in its corresponding modified differential equation. Besides we have established the order of accuracy of the simulated data by applying the reconstructed scheme to a benchmark problem.

Chapter 4

DYNAMICS OF SPIRAL WAVES UNDER THE EFFECT OF OBSTACLES

4.1 Introduction

Having successfully accomplished the validation of the code resulting from the reconstructed HOC scheme for the Barkley model (3.1)-(3.2) in the previous chapter, we now endeavour to examine the dynamics of the spiral wave in and without the presence of obstacles through the same code. All numerical simulations in the present chapter are performed on a square of dimension $[0, 128] \times [0, 128]$ on a grid of size 257×257. Moreover for all simulations, we have employed the zero-flux boundary conditions and the initial conditions described by equations (3.17)-(3.18).

Winfree [115] observed that the rotating spiral waves, which are encountered in the famous chemical reaction known as B-Z reaction [11, 118], do not necessarily rotate periodically. His rigorous inspection led to the finding that these rotating spiral waves present in the B-Z reaction could also perform non-periodic rotation. For such non-periodic rotation, he coined a term called "meandering" of waves; and the movement of such spiral waves are characterized by tracing the position of the spiral tip. As such the spiral tip can execute either periodic (rigid) or non-periodic (meandering) rotation. Moreover, spi-

---

Some part of this chapter is published in [49].
Some part of this chapter is published in [27].

ral waves are also believed to be a major form of reentry underlying common cardiac arrhythmias [39, 93] which may lead to fibrillation, where monomorphic tachycardia may correspond to a stationary anchored spiral wave, and polymorphic tachycardia to a meandering spiral wave. This exemplifies the significance of the role played by the motion of spiral wave tip in the spiral wave dynamics. There are many numerical techniques to determine the spiral tip location [40, 65, 101], amongst which, we exploit the method of the intersection of the isocontours of the excitable and recovery variables.

In recent years, studies on the spiral wave dynamics have been of considerable interest among the scientists from diverse fields such as chemical, mathematical, physical and biological sciences [5, 9, 17, 28, 30, 40, 45, 105, 119]; and one such study is the transition of the spiral wave from rigid to the meandering rotation, which is characterized by the motion of the spiral tip. Such transition of the spiral wave in the heart plays a crucial role as it may correspond to the transition from a stable to polymorphic electric arrhythmias and then to fibrillation which some time may result in cardiac death. Barkley [9], studied the spiral wave dynamics by changing the reaction parameters; and explored that the transition of a spiral wave from simple to compound rotation occurs via a supercritical Hopf bifurcation. Further, in [5], Amdjadi proposed a numerical method to investigate the change in dynamics of the spiral wave; and this method is based on approximating the Euclidean norm of the state variables. It is surprising to note that in spite of the crucial role played by the spiral tip paths in the dynamics, almost all studies utilize only the state variables in order to examine the stability of the system. The current chapter envisages to use the spiral tip as a major tool to study the dynamics of the spiral waves through a comprehensive spectral density analysis. Besides, we depict some interesting patterns formed by the evolution of wave tips, viz., outward and inward petals. In the process, we have also compared these petals with the ones obtained from the explicit scheme. Besides, we provide a brief detail of the numerical method to evaluate the position of a spiral wave tip at a particular time. We further perform an analysis of the stability of the computed rotating spiral wave solutions through a numerical method explained in [5].

In addition to the above, there has also been a surge of studies of late amongst mathematicians and scientists alike on the interaction between rotating excitation waves and obstacle in excitable media [22, 60, 78, 79, 83, 99], leading to some very interesting observations. For example, in [99], Shajahan *et al.* studied the interaction of an obstacle to the spiral turbulence, which eventually leads to a simple rotating spiral wave; Panfilov and Keener [83], also discussed the possibility of spiral wave initiation due to the interaction of successive wavefront with an obstacle. Further, a meandering spiral wave is seen to perform a periodic rotation after being pinned to an obstacle which is very similar to the fibrillation like activity changes to tachycardia regime [60]. Moreover, interaction of meandering spiral waves with obstacles may result in the spiral wave break up [79]. Because of the above reasons, we also study the effect of an obstacle to the periodic rotating spiral waves and demonstrate how it affects the dynamics of the spiral wave.

4.2 Spiral tip computation

In the following, we provide an outline of numerically computing the tip of a spiral throughout the evolution of time. Firstly the spiral wave is allowed to develop to a recognizable shape which occurs around $t = 2.0$. We then explore the spiral tip path by exploiting the method of intersection of two isocontours of the variables u and v, precisely $u(= u_*) = 0.5$ and $v(= v_*)$ is given by $f(u_*, v_*) = 0$, where f is given in equation (3.1). In order to obtain the spiral tip location say (x^*, y^*) at a particular time t, we exploit Bi-Cubic Langrange interpolation polynomial [19] for the functions $u(x, y, t)$ and $v(x, y, t)$. Consider $P_u(x, y)$ and $P_v(x, y)$ to be the Bi-Cubic Langrange interpolation polynomials corresponding to the functions $u(x, y, t)$ and $v(x, y, t)$ respectively; mathematically these are given by

$$P_u(x, y) = \sum_{i=0}^{i=3} \sum_{j=0}^{j=3} u(x_i, y_j, t) L_{ij}(x, y), \tag{4.1}$$

$$P_v(x, y) = \sum_{i=0}^{i=3} \sum_{j=0}^{j=3} v(x_i, y_j, t) L_{ij}(x, y), \tag{4.2}$$

where

$$L_{ij} = L_i(x)L_j(y), \quad 0 \le i \le 3, \quad 0 \le j \le 3 \tag{4.3}$$

with

$$L_i(x) = \prod_{r=0, r\neq i}^{r=3} \frac{x - x_r}{x_r - x_i}, \quad L_j(x) = \prod_{r=0, r\neq j}^{r=3} \frac{x - x_r}{x_r - x_j} \tag{4.4}$$

and also

$$L_{ij}(x_r, y_s) = \begin{cases} 1, & \text{if } i = r, \quad j = s \\ 0 & \text{otherwise.} \end{cases} \tag{4.5}$$

Next, we solve the following nonlinear system of equations,

$$P_u(x, y) - u_* = 0, \tag{4.6}$$

$$P_v(x, y) - v_* = 0, \tag{4.7}$$

to locate the position of spiral wave tip (x^*, y^*) using the Newton-Method [20].

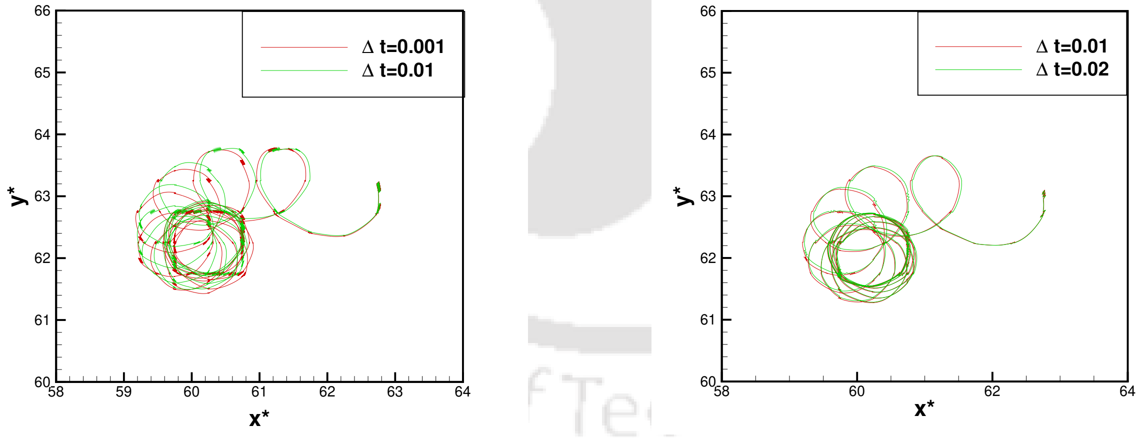

(a) (b)

Figure 4.1: Comparison of spiral tip path computed with different time steps by: (a) explicit scheme and (b) HOC scheme. While the the parameters values are $a = 0.84$, $b = 0.07$, $\epsilon = 0.02$, $D_u = 1.58$ and $D_v = 0$.

We exhibit the spiral tip paths obtained by both explicit and HOC schemes in figures 4.1(a) and (b) respectively, obtained with different time steps in the time range $2 \le t \le 50$. While a time step as large as $\Delta t = 0.02$ was good enough to obtain time grid independent results by our HOC scheme (see figure 4.1(b)), the trajectories obtained through the explicit scheme employing different time steps are distinctly different from each other even with a much smaller time step $\Delta t = 0.001$ (see figure 4.1(a)).

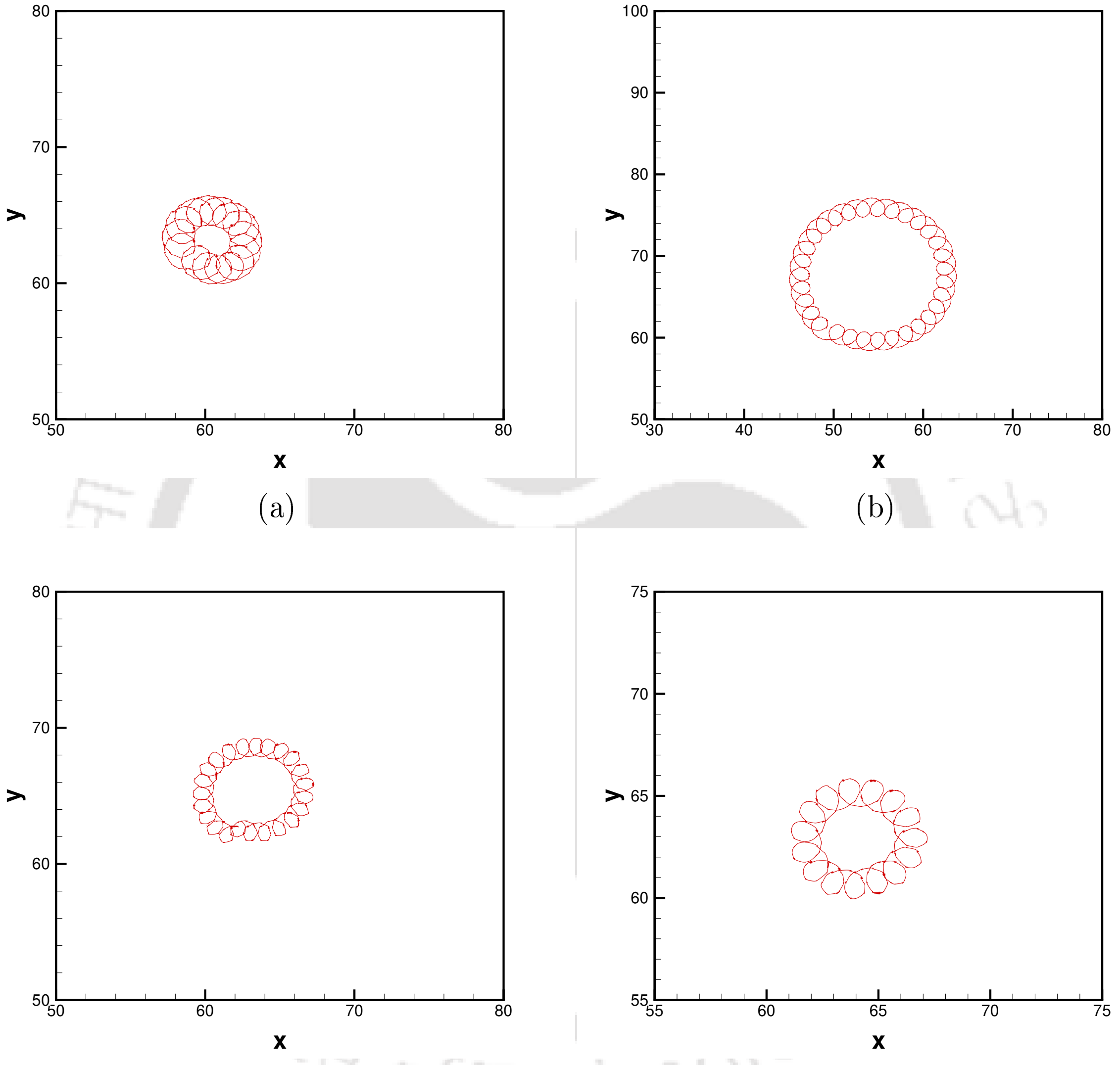

(a) (b)

(c) (d)

Figure 4.2: (a-b) Tip paths for exhibiting inward petals ($a = 0.60$), and (c-d) tip paths for exhibiting out ward petal ($a = 0.70$). Left panel (Explicit scheme) and right panel (HOC scheme).

Further, we depict some other interesting patterns traced by the spiral tips, specifically the outward and inward petals calculated by using the HOC scheme given by equation (2.11). Moreover, we also compare these petals with the ones obtained from the Euler's Explicit scheme. For this, we use the parameter values $D_u = 1.0$, $D_v = 0$, $b = 0.05$,

$\epsilon = 0.02$, $a(= 0.60, 0.70)$ in the system (3.1)-(3.2). Here the values of parameter a have been chosen from [8] in a such way that the spiral tips form an inward and an outward petals respectively corresponding to those values; the time step for all simulations is kept at $\Delta t = 0.01$.

We now exhibit the spiral tip paths for the different values of the parameter $a = 0.60$ in figures 4.2(a)-(b), and likewise for $a = 0.70$ in figures 4.2(c)-(d), computed by the reconstructed HOC and Explicit schemes. It can be seen from the figures 4.2(b) and (d), that the petals obtained from our HOC computation are very close to the results obtained in [8]. On the other hand, due the presence of the implicit numerical diffusion and dispersion in the data resulting from lower order accurate schemes discussed earlier in previous chapter 3, petals resulting from the Explicit scheme (shown in figures 4.2(a) and (c)) are distorted ones while the HOC simulation produces perfect petal shapes (as in [8]).

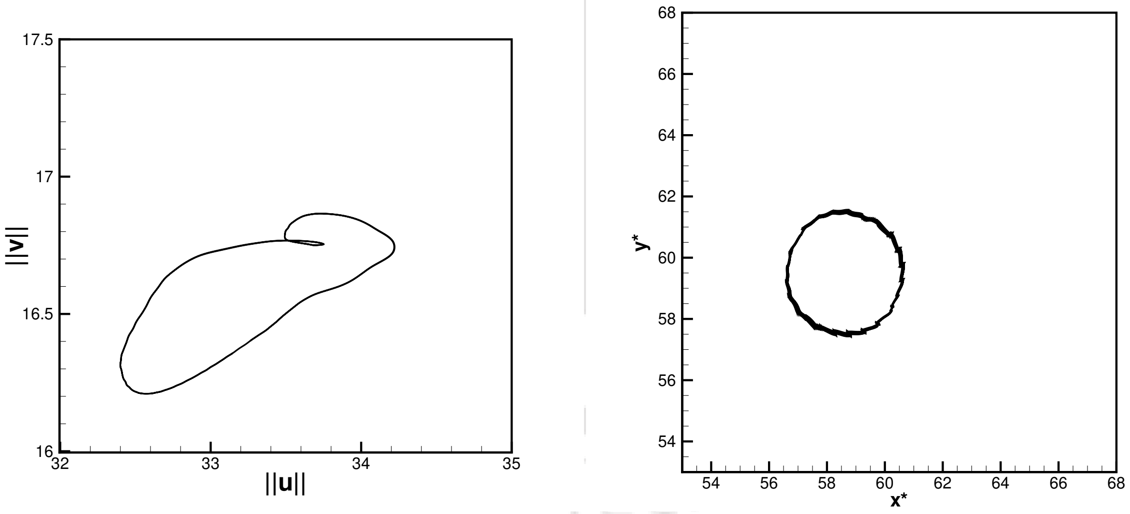

(a) (b)

Figure 4.3: Phase diagram from the explicit computation between $100 \leq t \leq 150$ for the value of $a = 0.33$: (a) Euclidean norms of the state variables and (b) the coordinates of the spiral tip.

Also because of the implicit numerical reaction, diffusion and dispersion mentioned in section 3.2.2, coupled with its lower order accuracy, for certain parameters (viz., $b = 0.001$, $\epsilon = 0.02$ $D_u = 1.0$ and $D_v = 0$ as in [5]) in the equations (3.1)-(3.2), the explicit scheme produces stable spiral till $a < 0.34$ as can be seen from figures 4.3(a)-(b). On the other hand, the HOC computation was able to track the second dominant frequency much earlier at $a = 0.324$ as would be discussed in the next section 4.3.

4.3 Spiral dynamics through spectral density analysis

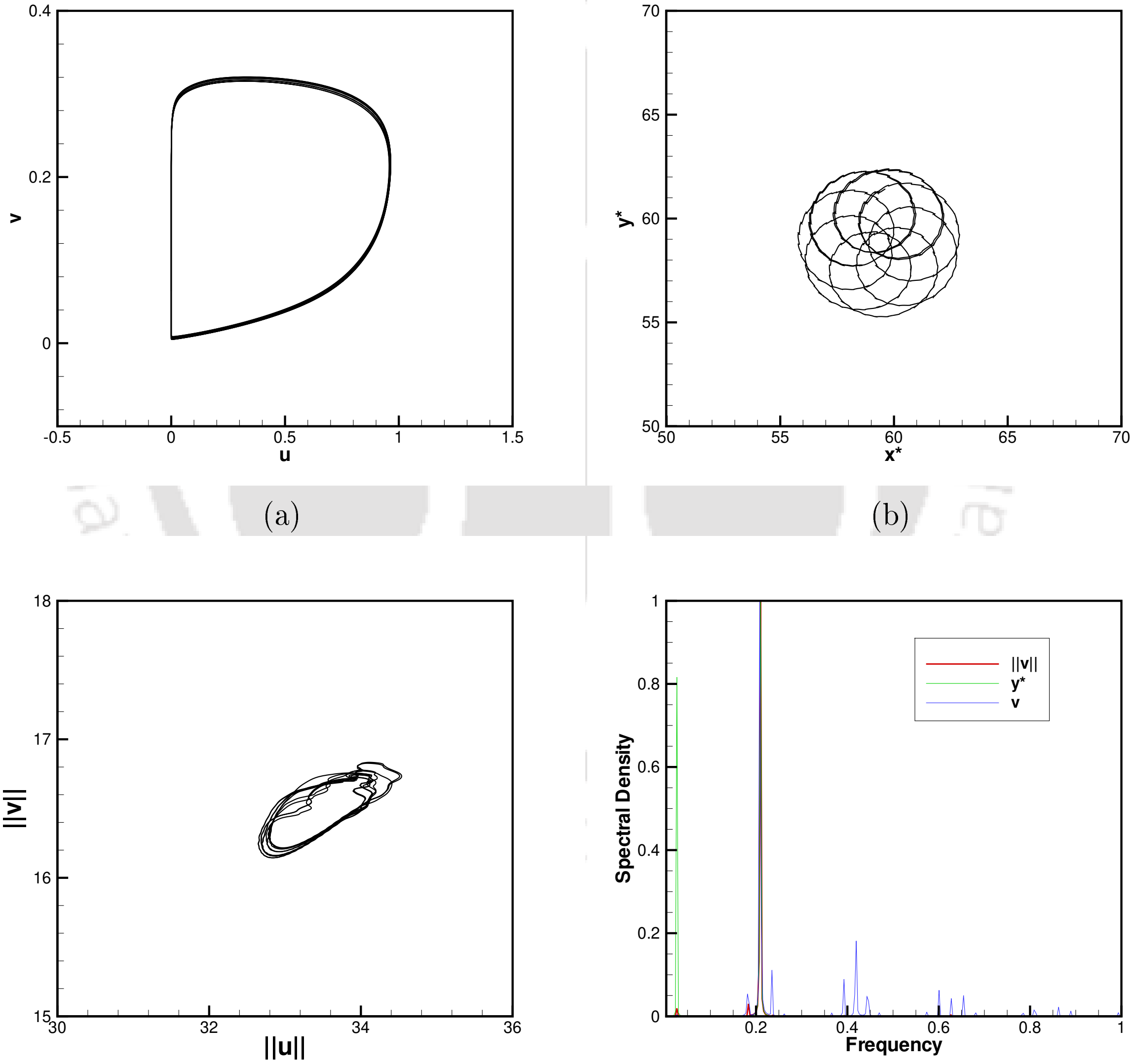

(a) (b)

(c) (d)

Figure 4.4: Phase diagram from the HOC computation: (a) state variables u and v, (b) the spiral tip coordinates, (c) the Euclidean norms of state variables u and v, and (d) power spectra of y^*, $||v||$, v for $a = 0.33$, $100 \leq t \leq 150$.

In this section, we study the change in dynamics of spiral wave in an excitable medium with the help of power spectral density analysis through fast Fourier transformation (FFT) by exploiting the spiral tip path. Note that in most of the earlier studies, the stability of a spiral was analyzed on the basis of the phase portrait of the two state variables under consideration. Some claims have also been made that the phase trajectories of the Euclidean norms of the state variables represent the actual trajectory of the tip [5], which our computation found otherwise (figure 4.4(c)). Many a time, the time interval spanning the initial and final time used in the computation was too narrow and the time range of the computation was not long enough for a comprehensive resolution of the entire process (eg. [5]). The spectral density analysis provides a clear picture of different modes of the frequencies, some of which may not be traceable by the sole use of phase portrait analysis. One can clearly see from figure 4.4(a) that for the parameters considered here, the phase portrait of the state variables yields a closed trajectory, indicating a stable spiral. On the other hand, the trajectory of the tip in figure 4.4(b) and the Euclidean norms of the state variable in figure 4.4(c), clearly indicate a spiral with non-periodic rotation which was also observed at later times $1400 \leq t \leq 1500$. These observations are consistent with power spectra analysis in figure 4.4(d), where one can see more than one dominant frequency for all the variables under consideration. Interestingly, the computation resulting from the explicit scheme predicted a periodic stable spiral (figures 4.3(a)-(b)) for the same parameter values.

For the analysis of the dynamics of the spiral wave, we again use the Barkley model given by the system of nonlinear partial differential equations (3.1)-(3.2). We employ the same initial and boundary conditions, but with different parameters (viz. $b = 0.001$, $\epsilon = 0.02$, $D_u = 1.0$ and $D_v = 0$) and vary the value of parameter a using a time step $\Delta t = 0.01$ for all simulations as in [5]. We exploit the method of intersection of the isocontours of fast ($u = 0.5$) and slow variables v given by $f(0.5, v) = 0$, to find the spiral tip location at a particular time as described in the previous section 4.2. We start from the value of $a = 0.27$ so that the spiral waves are feasible [8] and simulated up to the final time $t = 1500$ for satisfactory results. From figure 4.5(e), it can be seen that there exist only one mode of frequency confirming that the motion of spiral tip is periodic and the maximum density occurs at the frequency 0.076669, so that the time period of one complete cycle is its reciprocal (= 13.04), which is corroborated by time history plot of the coordinates x^* and y^* of the spiral tip shown in figure 4.5(a) and also that the spiral tip path is a closed curve (see figure 4.5(c)). From the figures 4.5(e)-(f) and 4.6(e)-(f), one can clearly see an increase in the value of dominating frequency as the value of a increases. This is expected as an increase in the value of a is accompanied by an enhanced excitability [101]. It has already been explored in literature that as the value of a advances, the spiral wave moves faster. As such the periodicity of motions of the spiral tip decreases, which is also evidenced from our computation. For $a = 0.30, 0.315, 0.323$ the maximum density occurs at frequencies $0.16, 0.190006, 0.203340$ respectively, resulting in reduced time periods approximately 6.25, 5.2623 and 4.9179 respectively as can be seen from the time history plots of the tip coordinates in figures 4.5(b), 4.6(a) and 4.6(b). From figures 4.5(f), 4.6(e) and 4.6(f) it is clear that there is only one mode of frequency for the values of parameter $a = 0.30, 0.315, 0.323$ and also spiral tip paths are closed curve (see figures 4.5(d) and 4.6(c)-(d)).

But as soon as the value of parameter a is increased from 0.323 to 0.324, a second mode of frequency surfaces up as seen in figure 4.7(e) which shows that the periodicity lost for $a = 0.324$, hence the spiral wave starts meandering *i.e.* the spiral tip path does not follow closed (described as circular in [5, 8]) motion which has been been reflected in figure 4.7(c). The same conclusions can be drawn from the time history plot of the tip coordinates in figure 4.7(a), where one can clearly see that the amplitudes of waves are varying for different time cycles (see the portion below the arrow). As we further increase the value of parameter a (*i.e* 0.325 and 0.327), the second mode of frequency becomes more prominent (figures 4.7(f) and 4.8(c)), which can also be observed from the time history plots (see figures 4.7(b) and 4.8(a)). The trajectory of the tip is shown in figures 4.7(d) and 4.8(b) for the values of $a = 0.325$ and 0.327 respectively which depict meandering behaviour. As a conclusion, we claim that the spiral wave starts meandering from the value of parameter $a = 0.324$.

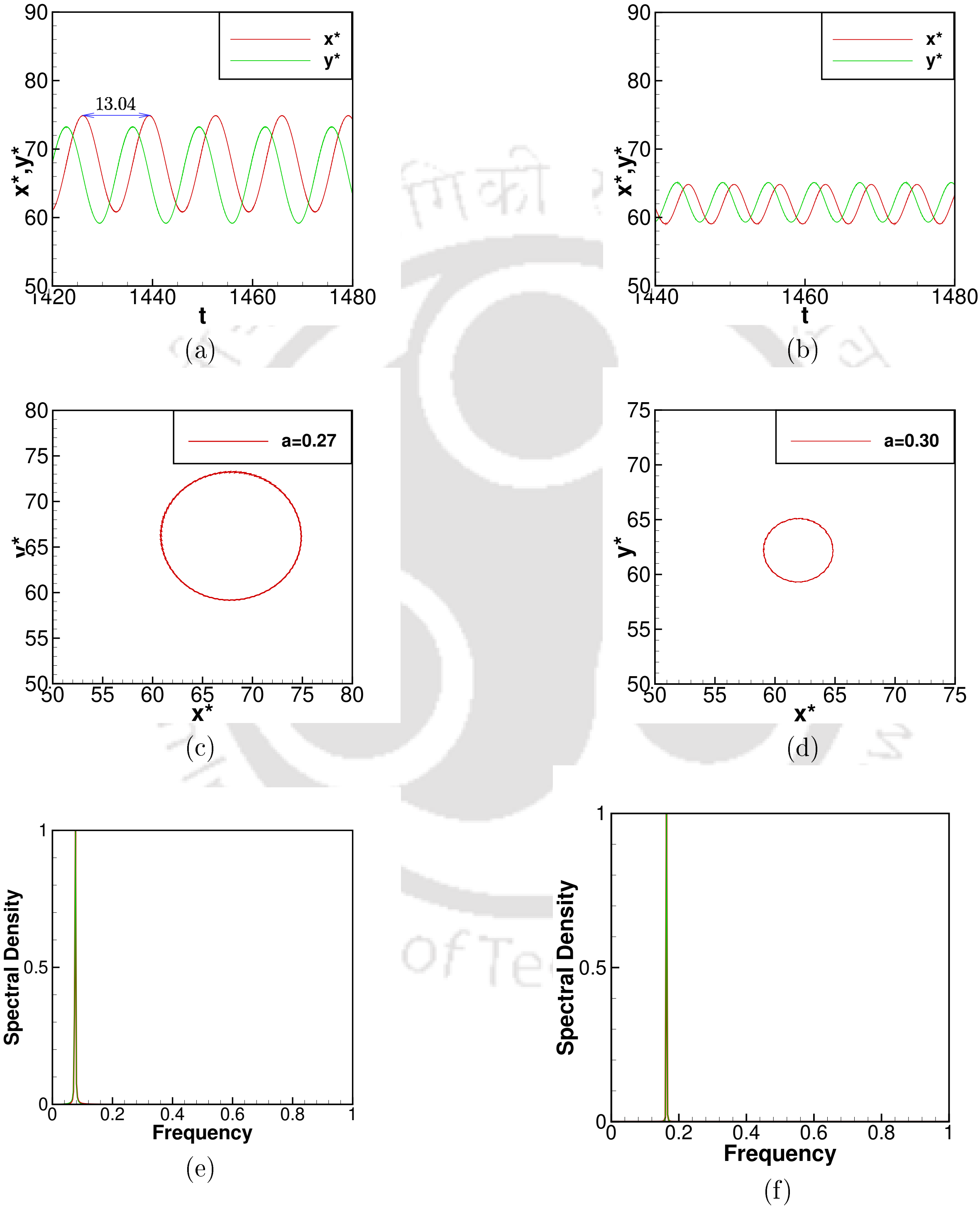

(a) (b)

(c) (d)

(e) (f)

Figure 4.5: For $a = 0.27$ (left panel) and $a = 0.3$ (right panel): (a)-(b) time history of the tip coordinates (x^*, y^*), (c)-(d) phase diagram of the tip $(x^{\cdot}y^*)$ for $1420 \leq t \leq 1480$, and $1440 \leq t \leq 1480$ respectively and (e)-(f) power spectra of (x^*, y^*) for $1201 \leq t \leq 1500$.

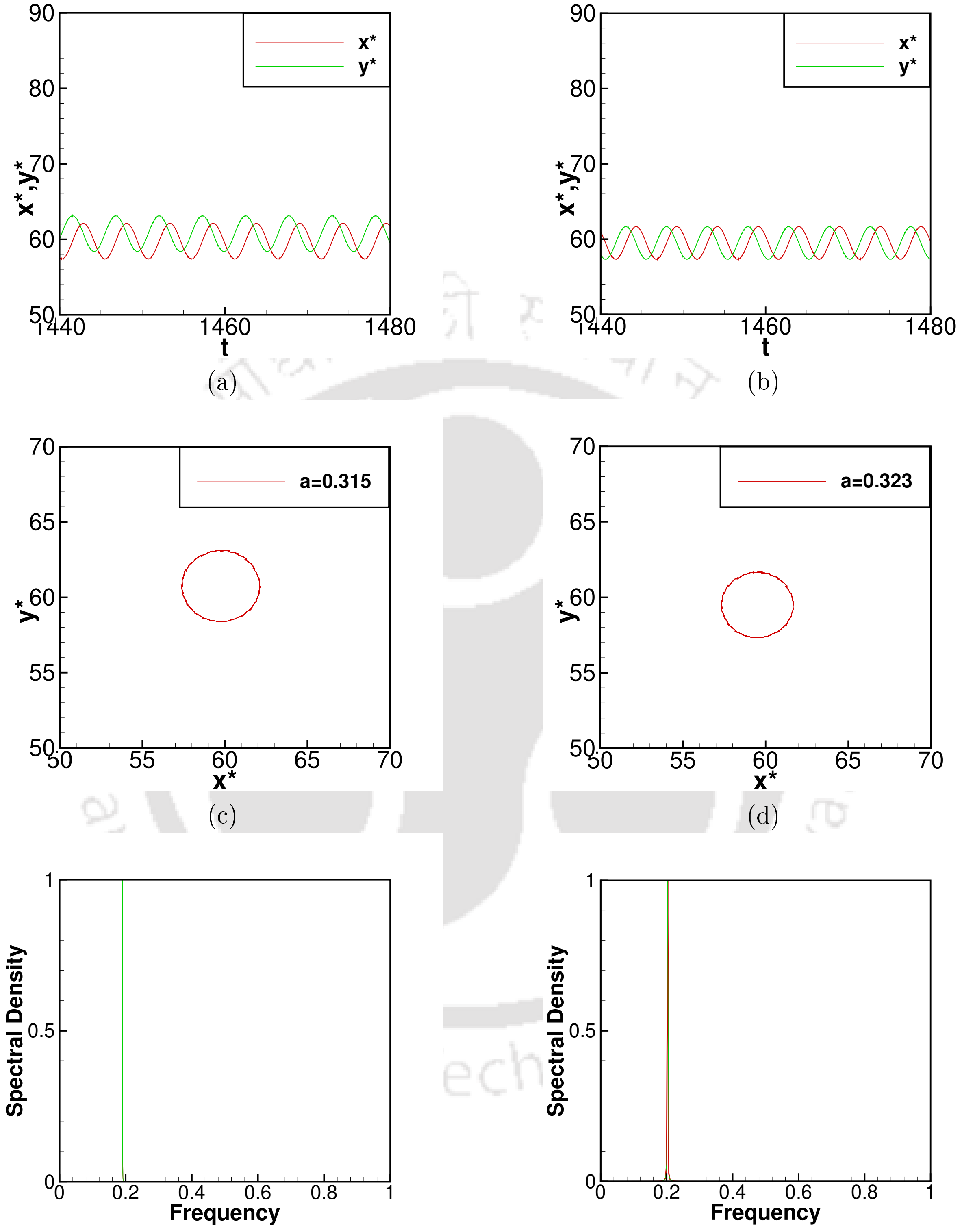

(a) (b)

(c) (d)

(e) (f)

Figure 4.6: For $a = 0.315$ (left panel) and $a = 0.323$ (right panel): (a,b) time history of tip (x^*, y^*), (c)-(d) phase diagram of tip coordinates the (x^*, y^*) in the range $1440 \leq t \leq 1480$ and (e)-(f) power spectra of the tip coordinates (x^*, y^*) for time range $(1201 \leq t \leq 1500)$.

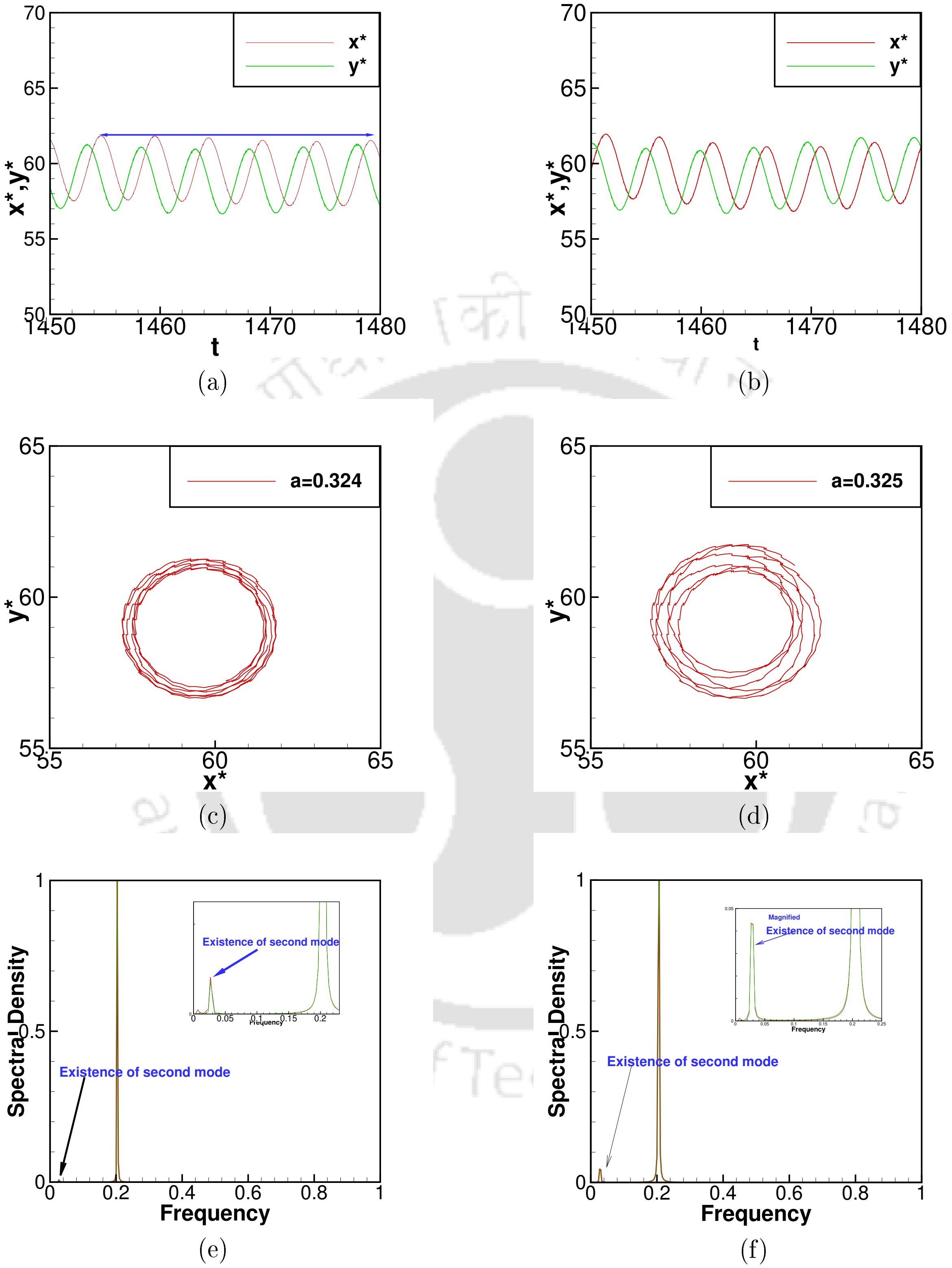

(a) (b)

(c) (d)

(e) (f)

Figure 4.7: For $a = 0.324$ (left panel) and $a = 0.325$ (right panel): (a)-(b) time history of tip coordinates (x^*, y^*), (c)-(d) phase diagram of the tip coordinates (x^*, y^*), and (e)-(f) power spectra of the tip coordinates (x^*, y^*) for the range $1201 \leq t \leq 1500$

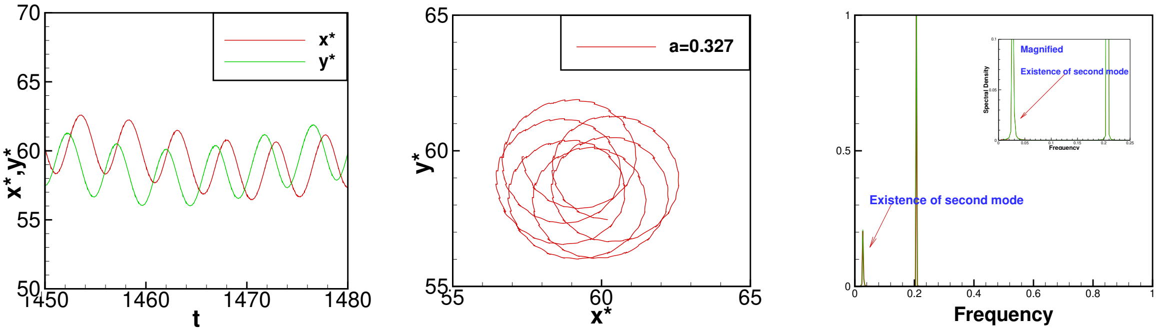

(a) (b) (c)

Figure 4.8: For $a = 0.327$: (a) time history of the tip coordinates $(x^{\cdot}y^{*})$, (b) phase diagram of the tip coordinates (x^{*}, y^{*}) in the range $1450 \leq t \leq 1480$ and (c) power spectra of the tip coordinates $(x^{\cdot}y^{*})$ in the range $1201 \leq t \leq 1500$.

4.4 A linear stability analysis of the computed solutions

Next, we investigate the stability of rotating spiral wave solutions resulting from the HOC simulations of the Barkley model through a numerical method explained in [5], which can be applied for both periodic and non-periodic (meandering) rotating spiral wave solutions. In the following, we briefly discuss this numerical method, which is based on the perturbation of the original state variables u and v, applied directly to the original partial differential equations. Let Δu and Δv be the perturbations introduced into the time dependent periodic (non-periodic) rotating spiral wave solutions $u = u(x, y, t)$ and $v = v(x, y, t)$ respectively for the system (3.1)-(3.2), i.e.

$$S(x, y, t) = u(x, y, t) + \Delta u(x, y, t) \tag{4.8}$$

$$T(x, y, t) = v(x, y, t) + \Delta v(x, y, t) \tag{4.9}$$

where S and T are perturbed solutions corresponding to the solutions u and v respectively. In order for the computed solutions to be stable, such small perturbations to the spiral wave solutions will die out or result in a mere phase shift [41]. Substituting (4.8)-(4.9) into (3.1)-(3.2),

$$\frac{\partial(u + \Delta u)}{\partial t} = D_u \nabla^2 (u + \Delta u) + \frac{1}{\epsilon} f(u + \Delta u, v + \Delta v), \tag{4.10}$$

$$\frac{\partial(v+\Delta v)}{\partial t} = g(u+\Delta u, v+\Delta v), \tag{4.11}$$

where $f(u,v) = u(1-u)\left(u-(v+b)/a\right)$ and $g(u,v) = u-v$. Now we expand the nonlinear reaction terms $f(u+\Delta u, v+\Delta v)$ and $g(u+\Delta u, v+\Delta v)$ using Taylor series about (u,v), yielding

$$\frac{\partial u}{\partial t} + \frac{\partial(\Delta u)}{\partial t} = D_u\nabla^2 u + D_u\nabla^2\Delta u + f(u,v) + \frac{1}{\epsilon}\frac{\partial f(u,v)}{\partial u}\Delta u + \frac{1}{\epsilon}\frac{\partial f(u,v)}{\partial v}\Delta v + \text{(higher order terms)} \tag{4.12}$$

$$\frac{\partial v}{\partial t} + \frac{\partial(\Delta v)}{\partial t} = g(u,v) + \frac{\partial g(u,v)}{\partial u}\Delta u + \frac{\partial g(u,v)}{\partial v}\Delta v + \text{(higher order terms)}. \tag{4.13}$$

Since u and v are known solutions to the system (3.1)-(3.2), hence we have the truncated linear system of equations after retaining only the linear terms:

$$\frac{\partial(\Delta u)}{\partial t} = D_u\nabla^2\Delta u + \frac{1}{\epsilon}\frac{\partial f(u,v)}{\partial u}\Delta u + \frac{1}{\epsilon}\frac{\partial f(u,v)}{\partial v}\Delta v \tag{4.14}$$

$$\frac{\partial(\Delta v)}{\partial t} = \frac{\partial g(u,v)}{\partial u}\Delta u + \frac{\partial g(u,v)}{\partial v}\Delta v \tag{4.15}$$

where $\partial f(u,v)/\partial u = (1-u)\left(u-(v+b)/a\right) - u\left(u-(v+b)/a\right) + u(1-u)$, $\partial f(u,v)/\partial v = -(1/a)u(1-u)$, $\partial g(u,v)/\partial u = 1$ and $\partial g(u,v)/\partial v = -1$. The stability of the spiral wave solutions $u(x,y,t)$ and $v(x,y,t)$ depends on the fact that $\Delta u,\ \Delta v \to 0$ (or perturbations remains very small as time progresses). If the solutions u and v are stable then the trajectories of perturbed solutions $S(x,y,t)$ and $T(x,y,t)$ defined by equations (4.8)-(4.9) either coincide with the trajectories of u and v respectively or remains extremely close to them. The trajectory of a function $U(x,y,t)$ could be obtained from its norm defined by [5]:

$$\|U\|_2 = \left\{\int_{a_x}^{b_x}\int_{a_y}^{b_y} |U(x,y,t)|^2 dxdy\right\}^{\frac{1}{2}} \approx \left\{h^2\sum_{i=0}^{m-1}\sum_{j=0}^{n-1}|U(x_i,y_j,t)|^2\right\}^{\frac{1}{2}} \tag{4.16}$$

In our numerical computations $a_x = a_y = 0$, $b_x = b_y = 128$, and $m = n = 257$ and space step $h = (b_x - a_x)/(m-1) = (b_y - a_y)/(n-1) = 0.5$. The parameter values that have been chosen here are: $b = 0.001$, $\epsilon = 0.02$, $D_u = 1.0$, and we choose the values of a (viz. $a = 0.30,\ 0.327$) in such a way that the original system yield both periodic ($a = 0.30$) and non-periodic ($a = 0.327, \quad 0.35$) rotating spiral wave solutions as discussed in previous section 4.3.

In order to study the stability, we first solve the perturbed system (4.14)-(4.15) to obtain the perturbation solutions S and T. Note that the solution of the system (4.14)-(4.15) has also been obtained by using the reconstructed HOC scheme of chapter 2. The following algorithm has been used to compute the perturbation:

1. Solve the original system (3.1)-(3.2) to obtain solutions $u_0(x, y, t_0)$ and $v_0(x, y, t_0)$ at time $t = t_0$.

2. Set the initial conditions for the perturb system (4.14)-(4.15), as $\Delta u_0 = u_0/50$ and $\Delta v_0 = v_0/50$.

3. Employing initial conditions u_0, v_0, Δu_0 and Δv_0 defined in steps 1 and 2, compute solutions u and v for the original system and Δu and Δv for the perturbed system at the next time step $t + dt$.

4. Calculate $S = u + \Delta u$ and $T = v + \Delta v$ and determine their norms by formula (4.16).

5. Set $u_0 = u$, $v_0 = v$, $\Delta u_0 = \Delta u$ and $\Delta v_0 = \Delta v$.

6. Repeat steps 3 to 5 up to time $t = 150$.

We depict the original solution along with their perturbed counterpart in figure 4.9. From figures 4.9(a)-(b), it is clear that the trajectories of u and v and the corresponding perturbation solutions S and T are very close to each other for the value of $a = 0.30$, confirming that the periodic rotating spiral wave solutions are stable. Likewise, from figures 4.9(c)-(d) and 4.9(e)-(f), it can be clearly seen that the trajectories of u and v and their corresponding perturbation solutions S and T are very close to each other for $a = 0.327$ and $a = 0.35$ respectively, confirming that the non-periodic (meandering) rotating spiral wave solution is also a stable one.

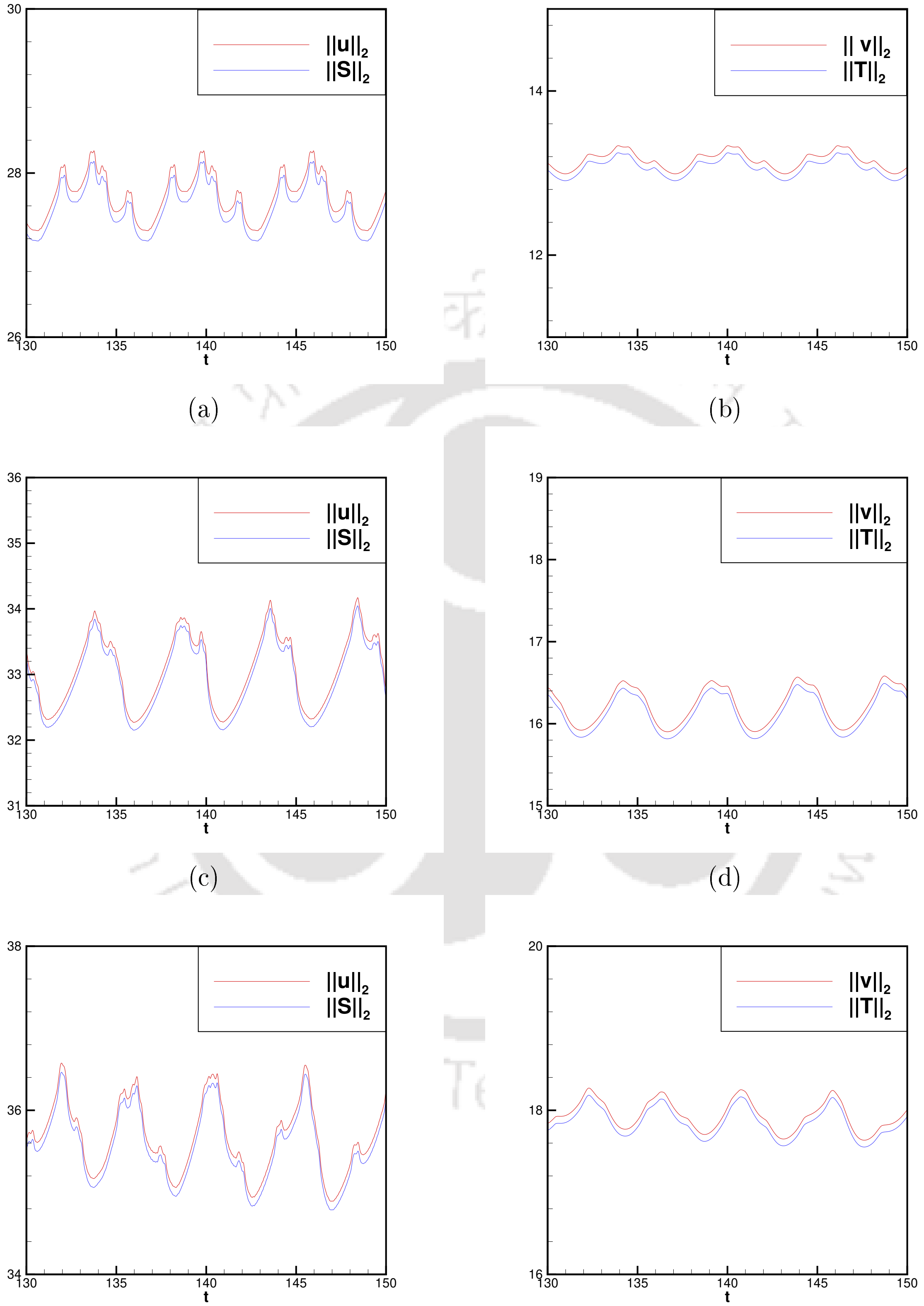

(a) (b)

(c) (d)

(e) (f)

Figure 4.9: Stability analysis: Comparison of the original and the perturbed solutions for different values of a: (a)-(b) $a = 0.30$, (c)-(d) $a = 0.327$ and (e)-(f) a=0.35.

TH-2268_136123014

4.5 Effect of placing an obstacle in the problem domain

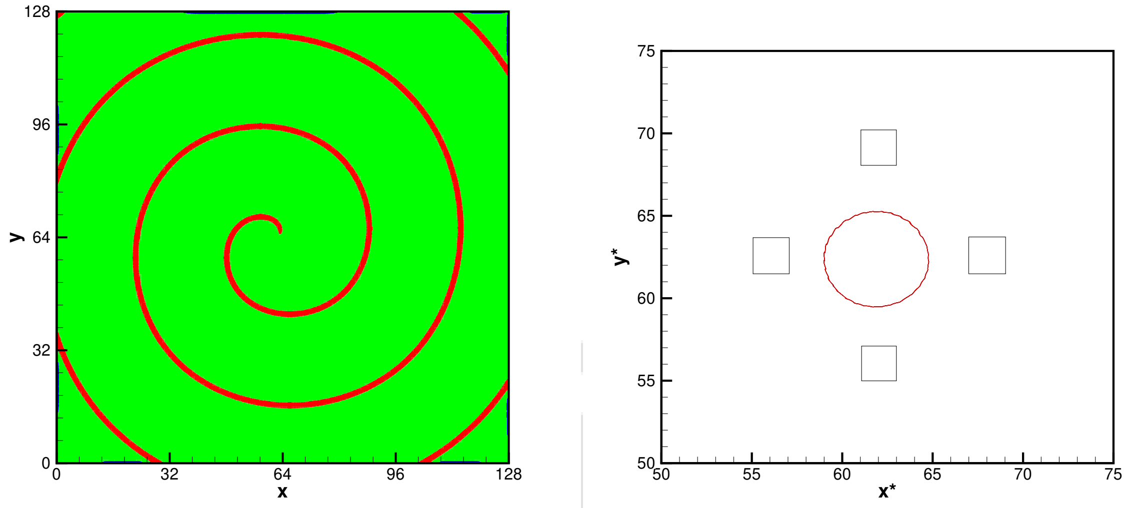

(a) (b)

Figure 4.10: (a) Spiral wave pattern at time $t = 100$ for variable u without the obstacle and (b) Geometrical representation of the obstacle at different locations in domain along with the tip trajectory corresponding to 4.10(a) as $t \to \infty$.

This section is concerned with the study of the behaviour of the periodic rotating spiral waves in the presence of an obstacle (rectangular box) placed at different locations of the problem domain. In order to do so, we choose an already tested value $a = 0.30$ resulting in periodic motion of the spiral waves keeping the values of other parameters same as in the previous section 4.3 (see figures 4.5(b), (d) and (f)). The geometric configuration of the situation can be seen in figure 4.10(b) where the obstacles are placed either on the left ($110 \leq i \leq 114, \quad 123 \leq j \leq 127$), right ($134 \leq i \leq 138, \quad 123 \leq j \leq 127$), top ($122 \leq i \leq 126, \quad 136 \leq j \leq 140$) or bottom ($122 \leq i \leq 126, \quad 110 \leq j \leq 114$) where i and j are the grid indices in horizontal and vertical directions respectively. This was accomplished computationally by setting $u = v = 0$ in those regions. The locations of the obstacles are chosen in such a way that they remain outside the tip trajectory of the spiral waves when no obstacle is present. Simulations are carried out by placing one obstacle at a time during a particular run. Computations are performed after placing the obstacle at time $t = 2$.

In figures 4.11(a)-(d), we exhibit the effect of the obstacle on the wave patterns at time $t = 100$ when it is placed at different locations of the domain, viz., bottom, top, left and right respectively. The effect of placing the obstacles are quite obvious from these figures as they are markedly different from the one without obstacle (figure 4.10(a)) and each other.

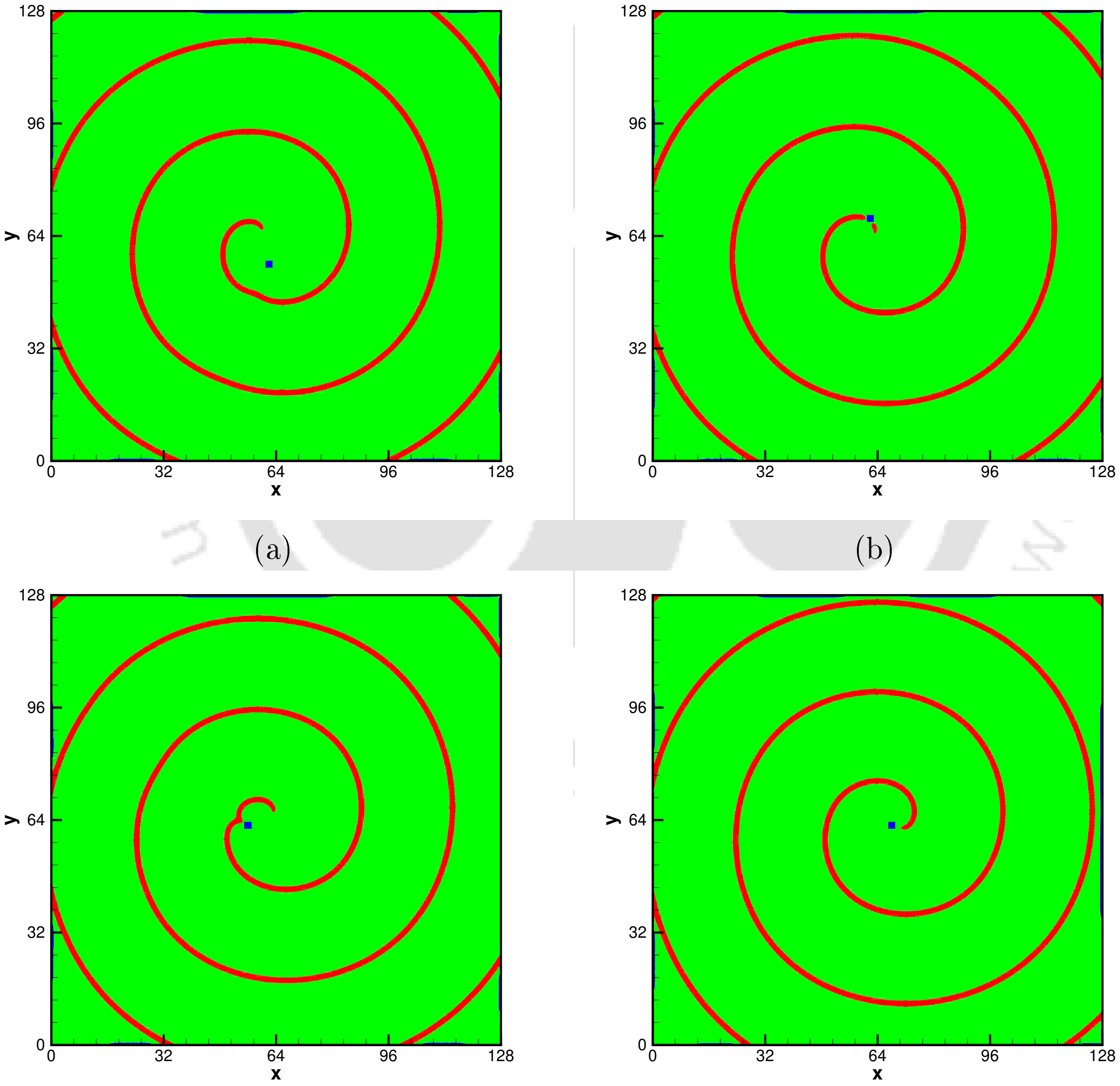

(a) (b)

(c) (d)

Figure 4.11: Spiral wave patterns at time $t = 100$, with obstacles placed at different locations as shown in figure 4.10(b), at: (a) bottom, (b) top, (c) left and (d) right.

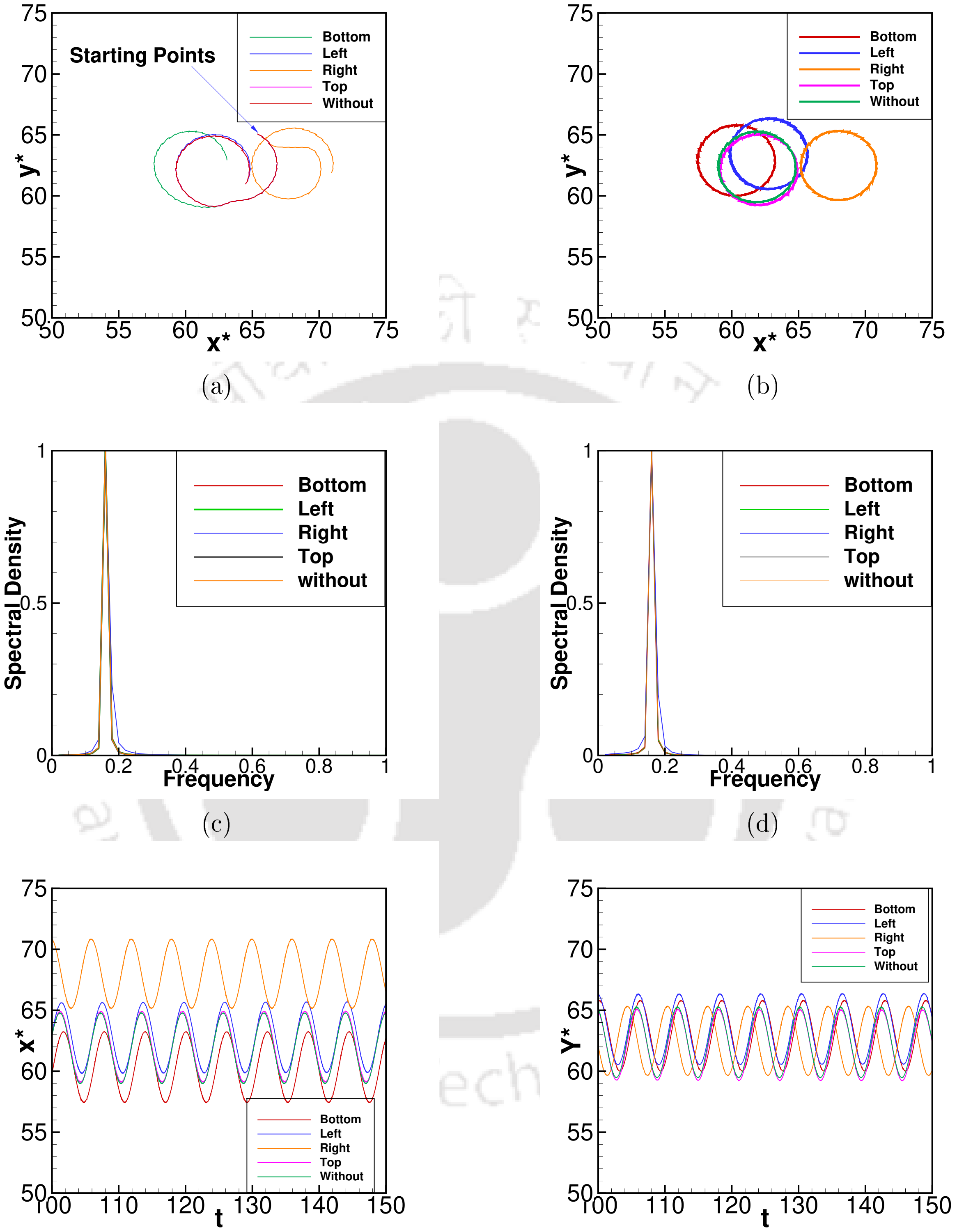

(a) (b)

(c) (d)

(e) (f)

Figure 4.12: Effect of obstacle on the dynamics spiral wave dynamics:(a) tip path for $2 \leq t \leq 10$, (b) tip paths for $100 \leq t \leq 150$ (c) -(d) power spectra of x^* and $y*$ respectively in the range $100 \leq t \leq 150$, and (e)-(f) time history of tip coordinates (x^*, y^*) respectively.

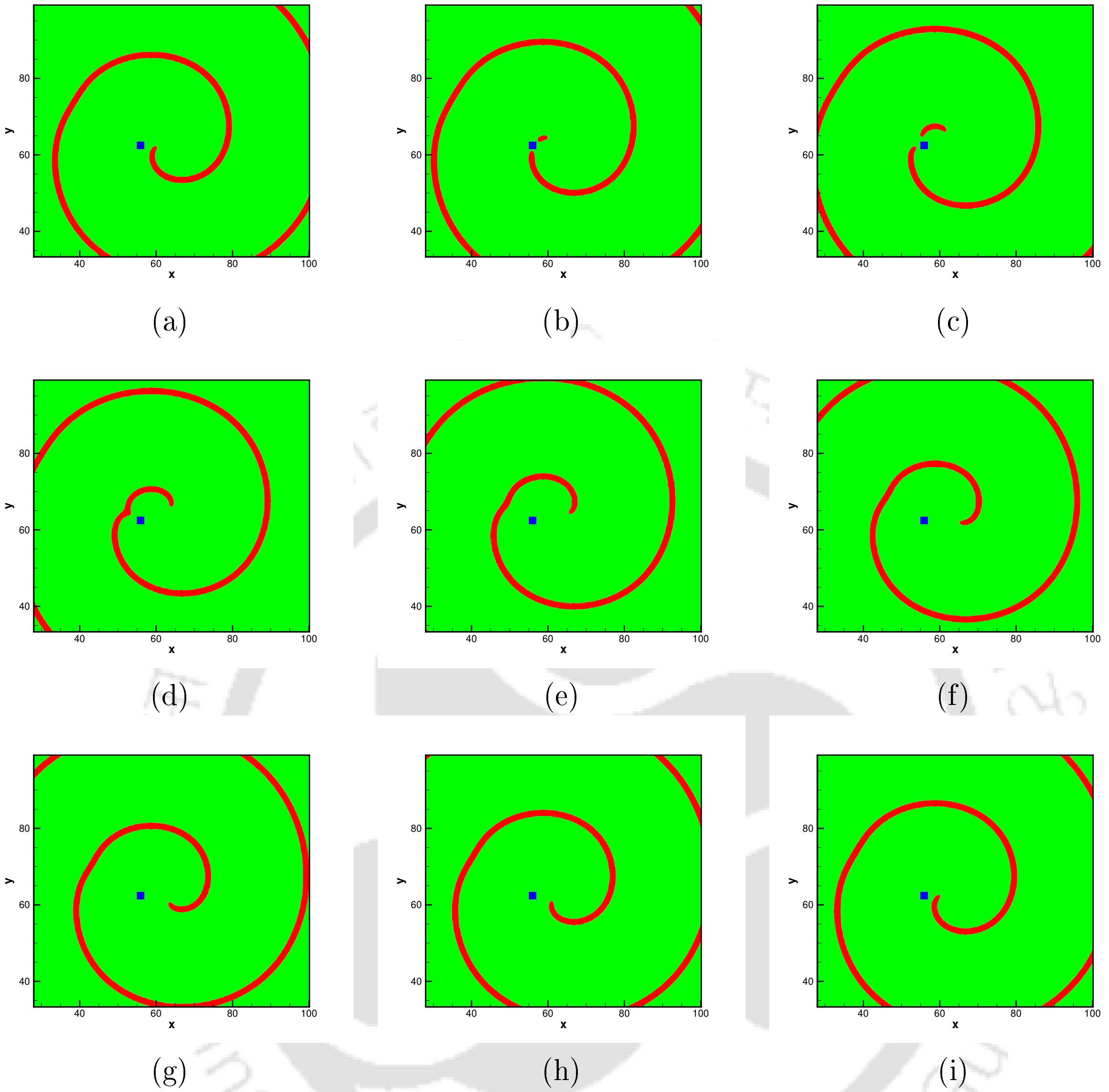

(a) (b) (c)

(d) (e) (f)

(g) (h) (i)

Figure 4.13: Spiral wave patterns while the obstacle placed at left showing one complete periodic cycle with period $T \approx 6.25$ starting at $t_0 = 97.1$: (a) $t = t_0$, (b) $t = t_0 + \frac{T}{8}$, (c) $t = t_0 + \frac{T}{4}$, (d) $t = t_0 + \frac{3T}{8}$, (e) $t = t_0 + \frac{T}{2}$, (f) $t = t_0 + \frac{5T}{8}$, (g) $t = t_0 + \frac{3T}{4}$, (h) $t = t_0 + \frac{7T}{8}$ and (i) $t = t_0 + T$.

Next, in figures 4.12(a)-(b) we show the tip trajectories of the spiral waves in and without the presence of the obstacles at the initial period $2 \leq t \leq 10$ and then at a later time $100 \leq t \leq 150$ respectively. As can be seen from figures 4.12(a)-(b), though all of them originates at the same point, as time progresses, depending upon the position of the obstacle in place, they start following different routes. However, they eventually settles into a periodic motion as can be seen from figure 4.12(b). Remarkably, the time period of rotation for all of them remains unchanged, which can be seen from the power spectra graph of the tip coordinates (x^*, y^*) (see figures 4.12(c)-(d)); there is only one dominant mode of frequency which corresponds to a frequency value 0.16 in all cases. As such the rotation period is independent of the location of the obstacles which turns out to be $T = 1/0.16 = 6.25$. This is further reconfirmed by time history data plot of the coordinates x^* (see figure 4.12(e)) and y^* see figure 4.12 (f)) of the tip.

After establishing the periodicity of the spiral waves, we show the close up view of the evolution of the spiral wave for a fixed obstacle location on the left for one complete periodic cycle in figures 4.13(a)-(i), where each figure is separated by a time interval of length $T/8$. One can clearly see the spiral wave front hitting the obstacle laterally, breaking up and merging again, and then replicating the same patterns after one complete period as can be seen from figures 4.13(a) and 4.13(i).

From the above observations, we conclude that the role of the obstacle is to change the trajectory of the tip whose path will depend upon the position of the surface of the obstacle where the spiral wave meets it. They will eventually relocate themselves as closed orbits different from the one without obstacle (of figure 4.10(b)).

4.6 Conclusions

We have computed the spiral tip trajectories from our post processed HOC data by exploiting the method of intersection of the isocontours of the state variables. Then, we have demonstrated that our computed spiral tip path with different time steps for the same set of parameters follow the same path and as such is time grid independent. Moreover, we have considered two different situations corresponding to the inward and outward petal formation of the tip trajectories. Also, we have compared our simulated petal formations with the ones obtained from Euler's explicit scheme and our results were found to be more closer to the available benchmark results.

Furthermore, for the first time, a comprehensive spectral density analysis of the spiral tip path has been performed to explore the effect of the parameters in changing the dynamics of a spiral wave. We have also established the computed rotating spiral wave solutions to be stable for both the periodic or non-periodic cases. We further study the effect of an obstacle to the periodic rotating spiral waves and demonstrate how it affects the dynamics of spiral wave. The obstacle was seen to change the trajectory of the spiral tip which eventually settled into a periodic motion again.

Indian Institute of Technology Guwahati

Chapter 5

STRAINING EFFECT ON THE SPIRAL WAVE DYNAMICS

5.1 Introduction

The application of the study of spiral waves in excitable media in many practical fields have already been discussed in the previous chapters, which in a way justifies the spurt of development in the numerical and experimental investigation in this field over the past few decades. However, all of them sidelined the effect of medium motion on the spiral wave dynamics. One of the well-known example of a moving excitable medium is the cardiac muscle, where the motion of heart is a concomitant of muscle contraction which is triggered by excitation, and another example of a moving excitable medium is the B-Z chemical reaction [3].

It must be noted that the medium motion can have a significant impact on the spiral wave dynamics; for example, the muscle motion can significantly alter the excitation propagation patterns. Only very few studies have been carried out under the conditions, where the excitable medium with recovery goes through relative straining motion [3,14–16,94,95]. Note that, the effect of medium motion is induced by adding an advection (convection) term into the system of equations (1.1)-(1.2), which yields a system of advection -reaction-diffusion equations. In a laboratory experiment, Agladze [3] has observed that the inter-

---

This chapter is published in [48].

TH-2268_136123014

action between the waves and dissipative structure in the B-Z reaction not only trigger in chaos, but also the break-up of the excitation waves due to strong convective motions. Interestingly, similar chaotic phenomenon leading to spiral wave break up is also considered to be most likely mechanism underlying ventricular fibrillation [7, 39, 58, 109]. Further, Biktashev et.al. [16], examined the effect of constant linear shear flows on the waves of excitation and concluded that the excitation waves may break-up due to the presence of the medium motion. Again in [15], Biktashev et.al., investigated the effect of medium motion on the excitation waves by implementing a linear shear or sinusoidal flow, where they observed that the shear can deform and then break spiral waves, which results in a chain of process of spiral wave formation and annihilation. Further, in [14], they studied the straining effect on an excitable medium and showed that repetitive wave trains break up for arbitrarily small velocity gradient, while the breaking of solitary waves needs the velocity gradient to exceed a certain threshold. It is noteworthy that the velocity fields assumed in their numerical studies are not irrotational, and also they do not satisfy the no-slip boundary conditions at the boundaries of the domain. Later in [94, 95], Ramos explored the effect of straining constituted by the additional convective terms in system (1.1)-(1.2), and characterized the range of strain rate into the following three different regimes: no break-up, transitional and break-up regimes; and the velocity field considered in his studies are irrotaional, solenoidal and also satisfy the no-slip conditions at the boundaries of the domain so that the velocity fields do not have any effect on reaction rate. Ramos has performed his numerical studies through the Oregonator model, which has been used to describe the many important features of the excitable media based on the B-Z chemical reaction [45,94,110]. The Oregonator model for the 2D excitable media, can be written as

$$\frac{\partial u}{\partial t} = \frac{1}{\epsilon}\left(u - u^2 - av\frac{u-b}{u+b}\right) + D_u\nabla^2 u, \tag{5.1}$$

$$\frac{\partial v}{\partial t} = u - v + D_v.\nabla^2 v. \tag{5.2}$$

Here a, b and ϵ are positive constants, D_v and D_v are diffusion coefficients corresponding to the excitable u and recovery v variables respectively with ∇^2 being the 2D dimensional Laplacian operator in Cartesian coordinates. The parameter b is the ratio of several reaction rate constants, whose value is $0 < b << 1$ and is independent of chemical concentration; the parameter a is the coefficient of stoichiometry.

The current chapter delves into the effect of straining on the stable rotating spiral waves, which can potentially trigger the spiral wave drift, enabling more insight into spiral wave dynamics. Our study was able to document such drifts along with deformation and stretching, resulting in extremely complex behaviour of the patterns. Based on the characteristics of the patterns, our study confirms all the three regimes observed in the earlier studies, viz., the no break-up, the transitional, and the break-up, but with an entirely different time range from the earlier ones reported in the literature [94], essentially for each of those regimes. Besides, we have investigated the effect of the reaction parameter on the dynamics of the spiral waves in the absence of the straining, employing the Oregonator model. Once again, the spiral wave tip path has been exploited as a major tool in order to put through a comprehensive spectral density analysis. Moreover, apart from performing a stability analysis of computed solutions, we have also carried out a grid independence and the convergence analysis of reconstructed HOC scheme (2.11), now for the Oregonator model.

5.2 Numerical results and discussions

5.2.1 Grid independence and order of convergence

Herein, we first establish the accuracy of the reconstructed HOC scheme (2.11) by performing a grid independence and convergence study for computed solutions obtained from the simulations of the Oregonator model (5.1)-(5.2). Throughout this chapter, values of parameters ϵ, b, D_u and D_v have been kept fixed, which are $\epsilon = 0.01$, $b = 0.002$, $D_1 = 1$ and $D_2 = 0.6$. The numerical computations of the system (5.1)-(5.2) has been performed on a square domain of size $[-7.5, 7.5] \times [-7.5, 7.5]$, while keeping the time step Δt for all numerical computations fixed at 10^{-4}. Zero-flux boundary conditions are applied on all the boundaries of the domain, which mathematically translates into $\nabla c \cdot \mathbf{n} = 0$, where $\mathbf{n}$ is the unit vector normal to the boundaries and c stands for either u or v. The initial conditions are set as:

$$u(x, y, 0) = \begin{cases} 0.8, & \text{if } 0 < \theta < 0.5, \\ b\dfrac{a+1}{a-1}, & \text{otherwise.} \end{cases} \tag{5.3}$$

$$v(x, y, 0) = \begin{cases} b\dfrac{a+1}{a-1} + \dfrac{\theta}{8\pi a}, \end{cases} \tag{5.4}$$

where θ is the angle (radians), measured counter-clockwise from the positive x-axis with respect to origin.

In order to establish the grid independence of our HOC simulations, computations are performed on grids of size 121 × 121, 241 × 241 and 481 × 481 up to final time $t = 50$. We depict the graphs of variables u and v along the vertical centerline in figures 5.1(a) and 5.1(b) respectively. From these figures, one can clearly see that the graphs of the both variables u and v, on grids 241 × 241 and 481 × 481 are overlapping, confirming that a grid of size 241 × 241 is good enough for a grid-independent solution. Similarly, the same conclusions can also be extracted from the contour plots of variables u and v, demonstrated in figures 5.2(a) and 5.2(b) respectively.

Next, we embark on computing the perceived rate of convergence of our computed data resulting from the system (5.1)-(5.2). Note that, because of the presence of highly nonlinear reaction terms in equation (5.1), finding analytical solution of the system (5.1)-(5.2) is extremely difficult. As such, we have adopted similar techniques as in chapter 3 in order to calculate the errors arising out of our computation. While in the chapter 3, we have only used root mean square relative errors, but here, we also used the maximum (E_{max}) error in addition to that, which can be defined as follows:

$$E_{max} = \max_{i,j} |\psi_{ana_{i,j}} - \psi_{num_{i,j}}|, \tag{5.5}$$

where the analytical (ξ_{ana}) and numerical (ξ_{num}) solutions are calculated at each grid point of the domain.

Now, we present the numerical rate of convergence of the computed data at time $t = 10$, resulting form HOC scheme (2.11) in tables 5.1-5.2 and 5.3-5.4 through the methods given by equations (3.5) and (3.8) respectively. In these tables, we can clearly see that the error decays with similar convergence rates for both u and v. The rates of convergence obtained from the current computation are slightly lower than that of theoretical convergence rates for u and v, which was also seen for the Barkley model of excitable media in the chapter 3.

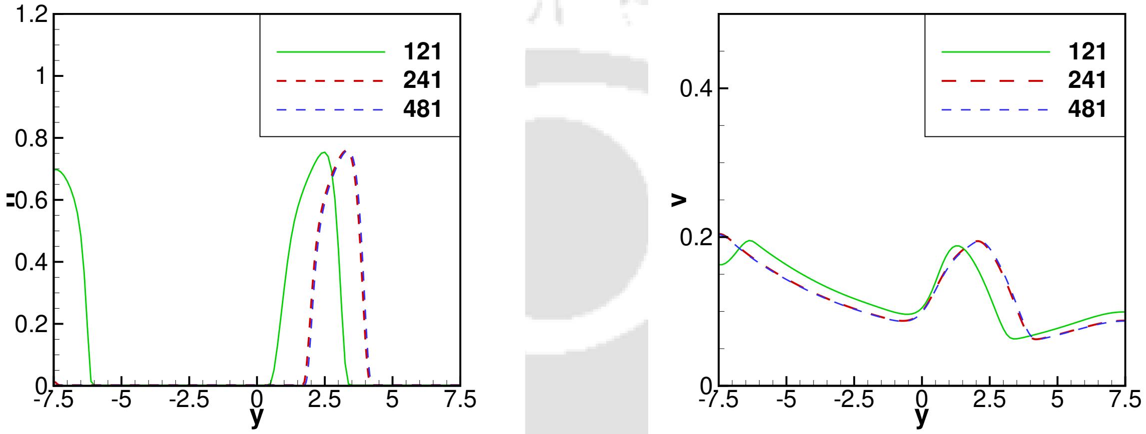

(a) (b)

Figure 5.1: (a)-(b) Plots of variables u and v respectively vs $-7.5 \leq y \leq 7.5$ at $x = 0$ with the value of $a = 1.4$ and final time of simulation is $t = 50$.

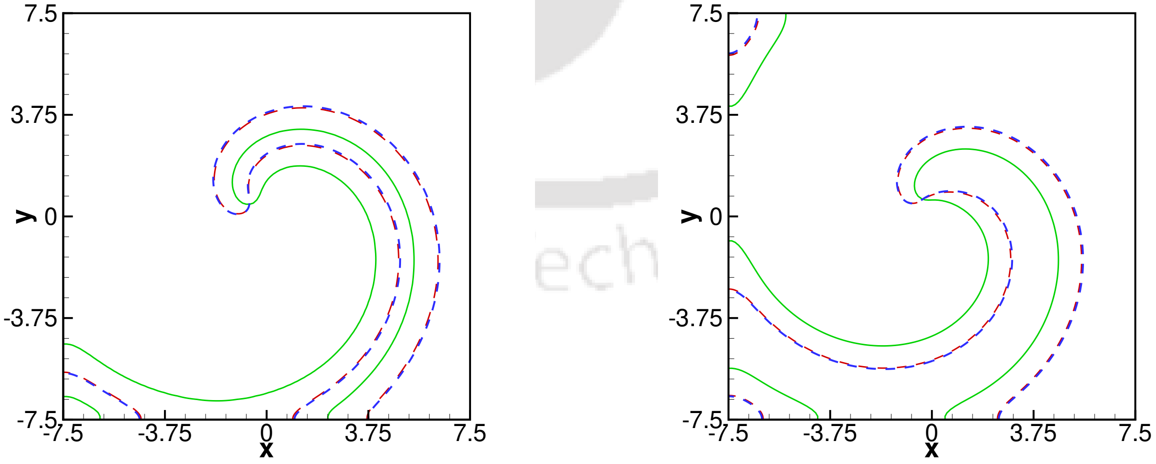

(a) (b)

Figure 5.2: (a)-(b) Contour plots of $u(= 0.5)$ and $v(= 0.15)$ respectively, on grids: 121×121 (green), 241×241 (red), 481×481 (blue) with the value of $a = 1.4$ and final time of simulation is $t = 50$.

Table 5.1: Convergence rate of the HOC scheme (2.11) by method (3.5): maximum error.

variables	**max error** (241×241)	**max error** (121×121)	**rate**
u	5.389430×10^{-2}	5.633189×10^{-1}	3.39
v	2.975500×10^{-3}	2.821950×10^{-2}	3.24

Table 5.2: Convergence rate of the HOC scheme (2.11) by method (3.5): rms relative error.

variables	**rms error** (241×241)	**rms error** (121×121)	**rate**
u	3.108324×10^{-2}	2.876955×10^{-1}	3.21
v	6.159897×10^{-3}	6.120675×10^{-2}	3.31

Table 5.3: Convergence rate of the HOC scheme (2.11) by method (3.8): maximum error.

variables	(481×481) **vs** (241×241)	(241×241) **vs** (121×121)	**Rate**
u	5.389430×10^{-2}	5.319291×10^{-1}	3.30
v	2.975500×10^{-3}	2.640359×10^{-2}	3.15

Table 5.4: Convergence rate of the HOC scheme (2.11) by method (3.8): rms relative error.

Variables	(481×481) **vs** (241×241)	(241×241) **vs** (121×121)	**Rate**
u	3.108324×10^{-2}	2.619301×10^{-1}	3.07
v	6.159897×10^{-3}	5.569677×10^{-2}	3.17

Having established the mesh independence of numerical results of the above example on a spatial mesh of size 241 × 241, all the computations that follow and are reported in the subsequent sections of this chapter, have been performed on a grid of the same size.

5.2.2 Spiral wave dynamics in the absence of straining

In the current chapter, we envisage to study the straining effect on periodically rotating spiral waves resulting from the B-Z reactions represented by the system (5.1)-(5.2). However, it would be interesting to study the role of the parameters in sustaining the stability of the rotating waves without the straining effect. It is important to note that only the parameter value "a" can be adjusted by calibrating the recipe parameters and/or temperatures, whose value can not exceed 4.0 [45]. As such, we vary the value of parameter a starting from 1.4 keeping the other parameters fixed as stated in section 5.2.1.

Contrary to almost all the earlier works using state variables, we exploit the evolution of tip coordinates as a major tool through power spectral density analysis in order to study the dynamics of the spiral waves. Here, we numerically locate the position of spiral tip (denote (x^*, y^*)) by determining the intersection of contours $u(= u_*) = 0.15$ and $v = v_*$, where v_* is obtained by solving $f(u_*, v_*) = 0$ and $f(u, v)$ is given in equation (5.1).

In figures 5.3(a), 5.3(b), 5.4(a) and 5.4(b), we demonstrate the power spectra plots of the tip coordinates (x^*, y^*) corresponding to the values of $a = 1.4$, 1.6, 1.70 and 1.72, respectively. From these figures, we can clearly see that there exist only one dominant mode of frequencies, which confirm the periodicity of the spiral wave tip paths for these values of $a = 1.4$, 1.6, 1.70 and 1.72. Also for the all these values of a, the maximum density occur at the frequency value 0.650003, as such the time period for one complete cycle becomes $1/(0.650003) \approx 1.5384$, which are further demonstrated by the time history plots of tip coordinates (x^*, y^*) in figures 5.3(c), 5.3(d), 5.4(c) and 5.4(d), corresponding to the values of $a = 1.4$, 1.6, 1.70 and 1.72 respectively. Moreover, figures 5.3(e), 5.3(f), 5.4(e) and 5.4(f) confirm that the spiral wave tips follow closed paths.

As we increase the value of parameter a from 1.72 to 1.725, one can see from the power spectra plots of tip positions (x^*, y^*) in figure 5.5(a), a secondary frequency mode surfaces up (see the spectral density corresponding to the frequency in the range $[0, 0.2]$ in close up in the top right of the figure), which confirms that the spiral wave starts following the non-periodic motion i. e. spiral wave tip path does not follow a closed trajectory, which has also been reflected in figure 5.5(e). Further, the plot of x^* and y^* with time t, presented in figure 5.5(c) gives a similar conclusion, where one can clearly see that the amplitudes of waves are varying for different time cycle (see the portion below the straight line). A slight increase in the value of a from 1.725 to 1.75, makes the existence of the second mode of dominant frequency (figure 5.5(b)) more clear, which can also be observed from the time history plots (figure 5.5(d)). Also the tip trajectory shown in figure 5.5(f), depicts meandering behaviour for the value of $a = 1.75$. Hence we conclude that the spiral waves start following non-periodic (meandering) motion from the value $a = 1.725$.

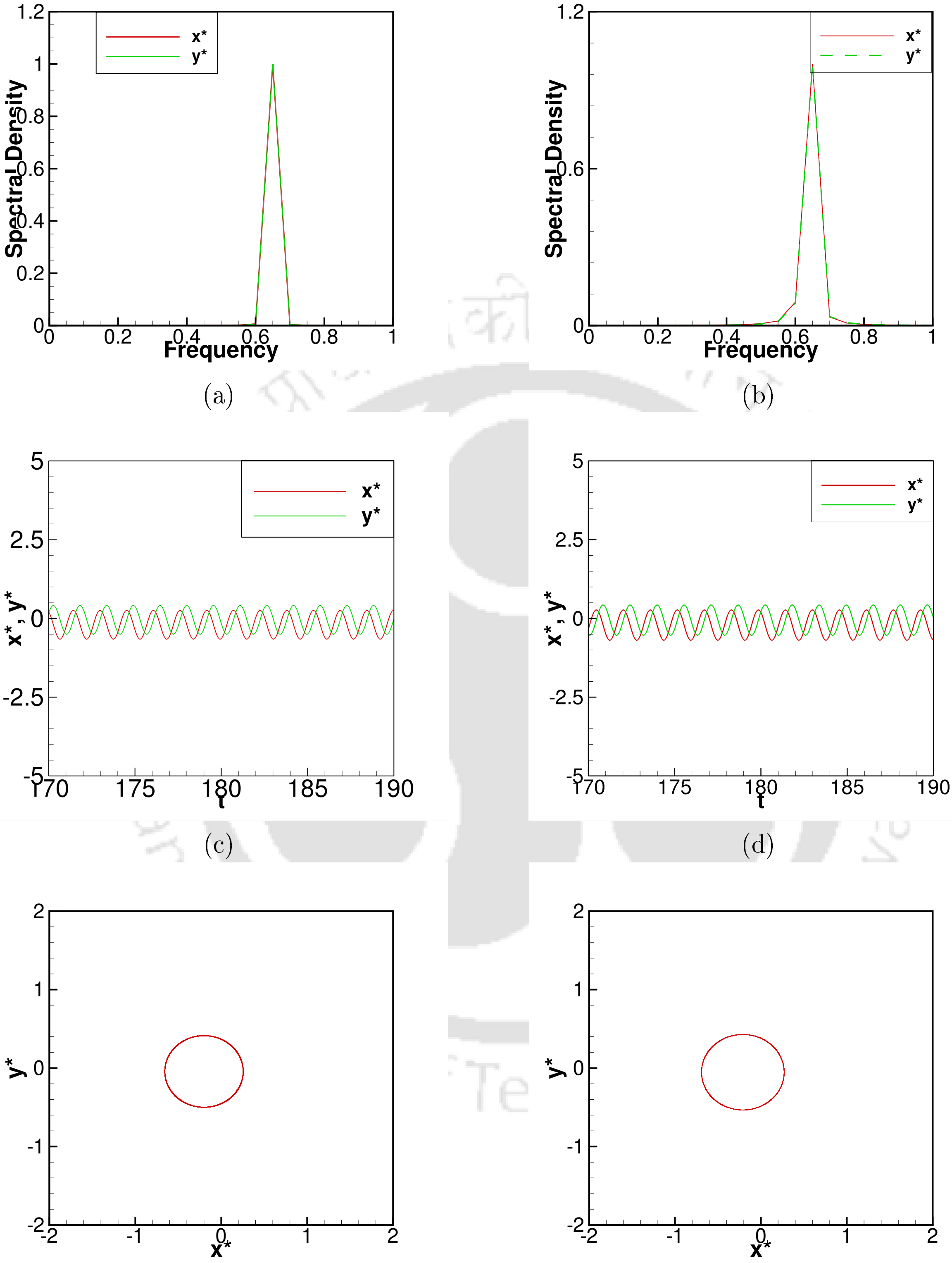

(a) (b)

(c) (d)

(e) (f)

Figure 5.3: Spiral dynamics for the value of $a = 1.4$ (left panel) and $a = 1.6$ (right panel) in the range $170 \leq t \leq 190$, for the tip coordinates (x^*, y^*): (a)-(b) power spectra, (c)-(d) time history plots, and (e)-(f) tip paths.

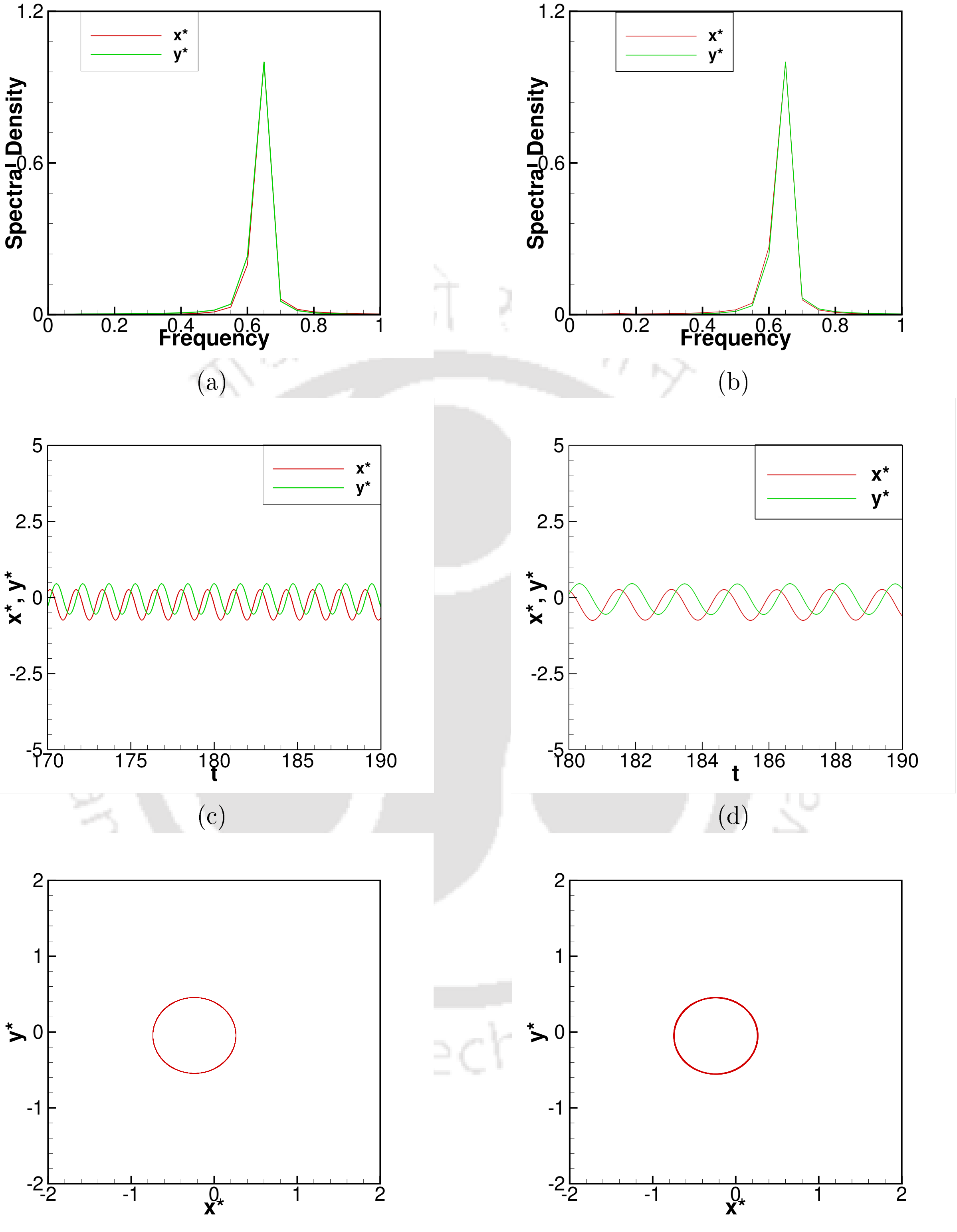

(a) (b)

(c) (d)

(e) (f)

Figure 5.4: Spiral dynamics for the value of $a = 1.70$ (left panel) and $a = 1.72$ (right panel) for the tip coordinates x^* and y^*: (a)-(b) power spectra in the range $170 \leq t \leq 190$, (c)-(d) time history plots and (e)-(f) tip paths in the range $170 \leq t \leq 190$.

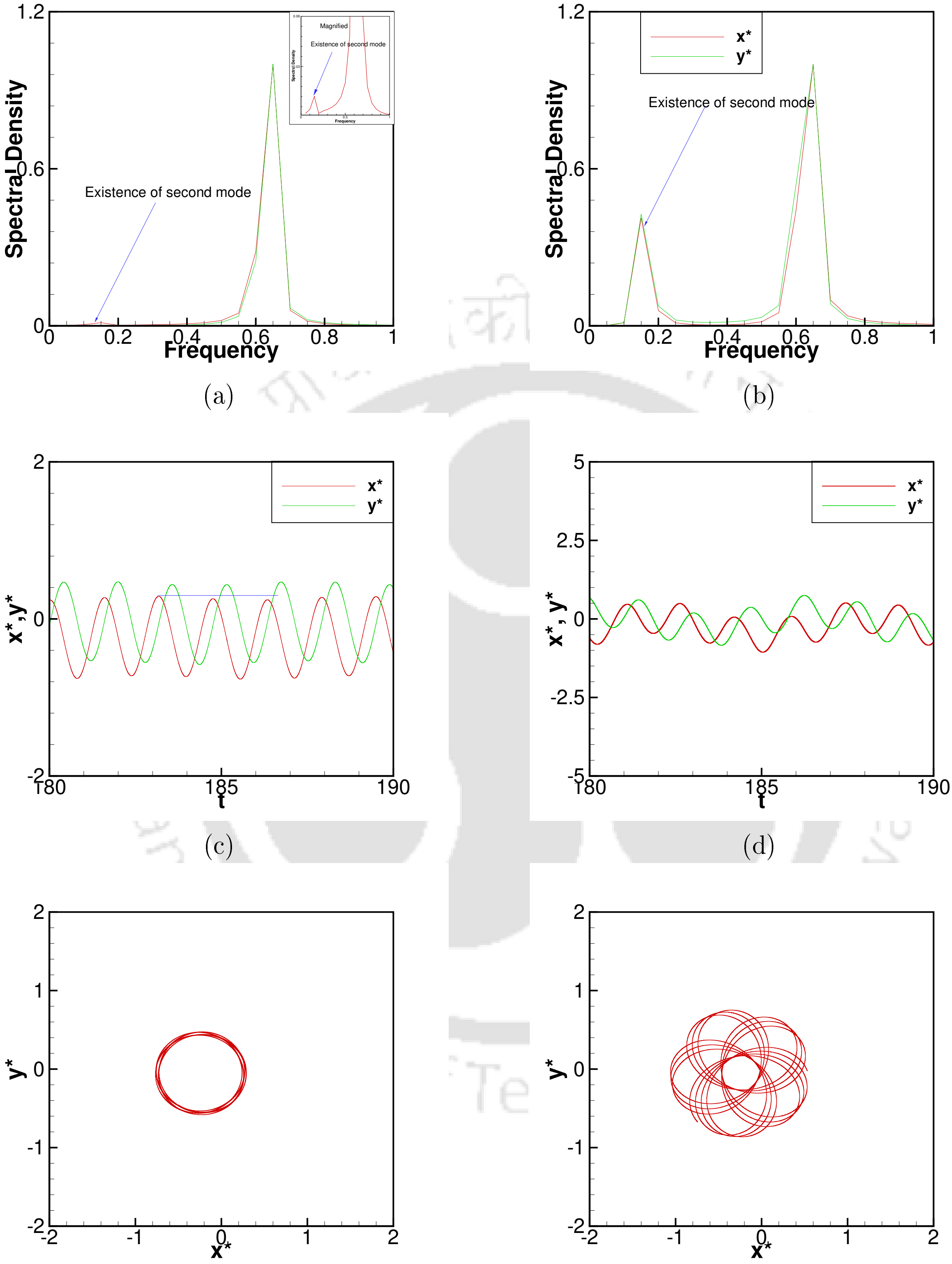

(a) (b)

(c) (d)

(e) (f)

Figure 5.5: Spiral dynamics for the value of $a = 1.725$ (left panel) and $a = 1.75$ (right panel) tip coordinates x^* and y^*: (a)-(b) power spectra in the range $170 \leq t \leq 190$, (c)-(d) time history plots and (e)-(f) tip paths in the range $170 \leq t \leq 190$.

5.2.3 Stability of the computed results

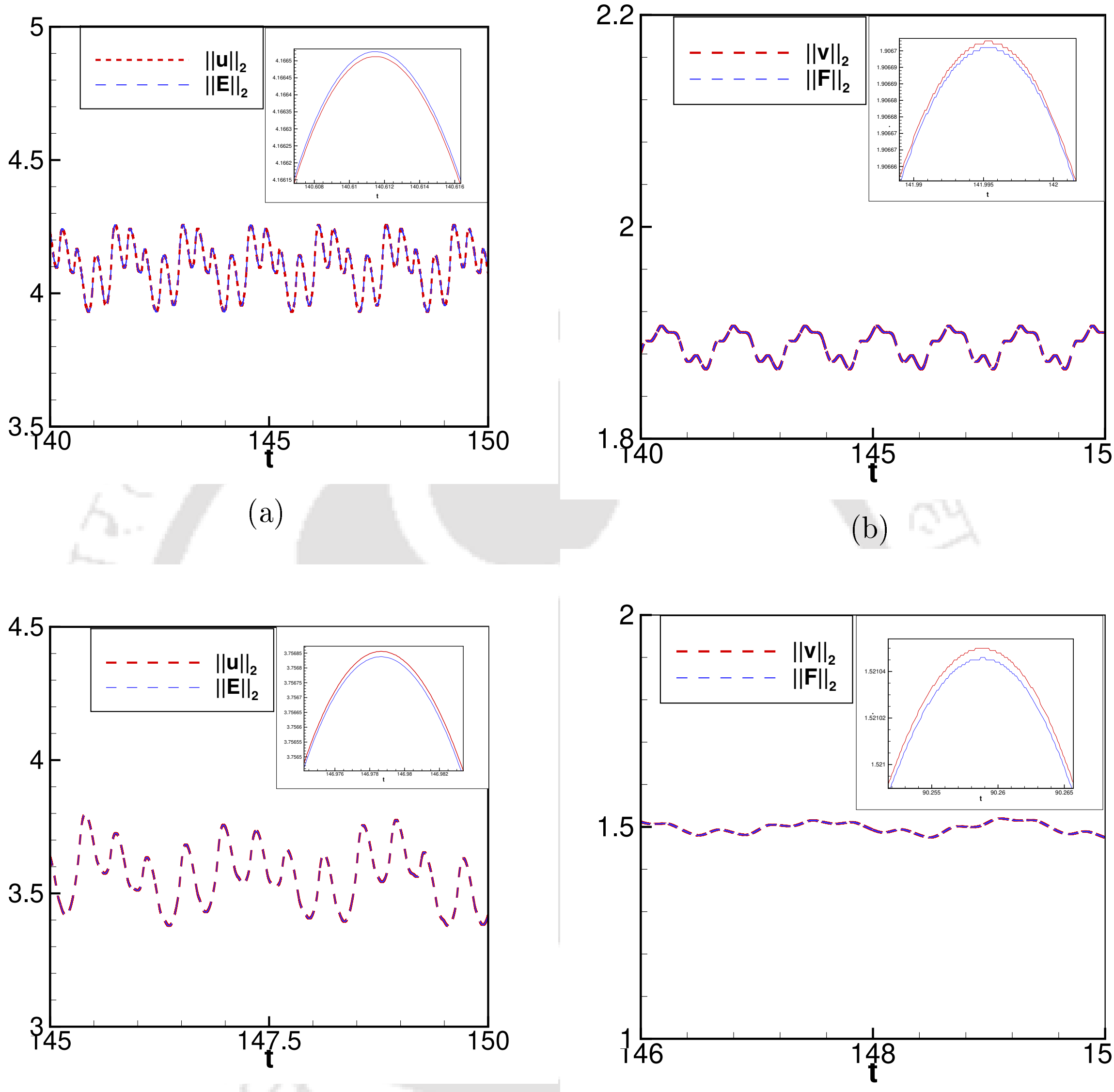

(a) (b) (c) (d)

Figure 5.6: Comparison between the trajectories of the original solution u and v and corresponding to their perturbed solutions E and F respectively for values of: (a)-(b) $a = 1.4$ and (c)-(d) $a = 1.75$.

In this section, we perform a stability analysis of the simulated rotating wave solutions resulting from the numerical computations of the Oregonator model given by equations (5.1)-(5.2), by the numerical approach described in section 4.4. Here the numerical computations are performed on the square domain $[-7.5, 7.5] \times [-7.5, 7.5]$ on a mesh of size

241×241, with the parameter values: $b = 0.002$, $\epsilon = 0.01$, $D_1 = 1.0$ and $D_2 = 0.6$. We choose two different value of $a = 1.4$ and 1.75, so that the system (5.1)-(5.1) yields both stable ($a = 1.4$) and meandering ($a = 1.75$) spiral wave solutions as documented in section 5.2.2.

The trajectories defined by equation (4.16) of the solutions u and v, along with trajectories of their corresponding perturbed solutions E and F respectively, have been depicted in the figure 5.6. It can be seen from the figures 5.6(a) and (b), that the trajectories of u and v are almost coinciding with the trajectories corresponding to their perturbation solutions E and F respectively, for value of $a = 1.4$, which confirms the stability of periodically rotating wave solutions. Similar conclusion can be drawn from figures 5.6(c)-(d), corresponding to value of $a = 1.75$, which affirms the stability of the non-periodic (meandering) rotating wave solution as well.

5.2.4 Spiral wave dynamics under the straining effect

Now, we proceed to investigate the effect of medium motion on the dynamics of stable rotating spiral waves. For this, an advection term is added for variables u and v in equations (5.1) and (5.2). The rationale behind adding this advection term is to mathematically model the effect of medium motion. For example, this advection term is equivalent to an external application of an electric field in the BZ solutions, that manipulates the dynamics of spiral waves since it causes advective motions of the ionic species in the reaction [67]. With the addition of this advection term equations (5.1) and (5.2) become,

$$\frac{\partial u}{\partial t} + V \cdot \nabla u = D_1 \nabla^2 u + u - u^2 - av\frac{u-b}{u+b}, \tag{5.6}$$

$$\frac{\partial v}{\partial t} + V \cdot \nabla v = D_2 \nabla^2 v + u - v, \tag{5.7}$$

where ∇ is the two dimensional gradient operator and $V = (V_x, V_y)^T$ is the velocity field consisting of components V_x and V_y in coordinate directions x and y respectively. We employ an irrotational ($\nabla \times V = \mathbf{0}$) and a solenoidal ($\nabla \cdot V = 0$) velocity field so that the convective terms do not instigate compressible effect, which can affect the reaction rate. Following [94], we have chosen the components of velocity field as: $V_x = -\gamma y$ and $V_y = -\gamma x$, where γ is strain rate (constant).

Note that in the thin layers of the BZ reaction, an electric field introduced through the advection terms forces the rotation centers of free spiral waves to drift along a straight path, and the drift speed increases with the increase in the magnitude of γ [2,75,104], as would be seen in the subsequent discussions. Another application of the introduction of this shear strain rate is in the study of the anomaly in heart. Interestingly, most of the experiments on the propagation of excitation in cardiac muscle are made on immobilised preparations. On the other hand, cardiac muscle could also be considered as a moving excitable medium, as excitation propagation may depend on the motion of the muscle [14–16], which corresponds to $\gamma \neq 0$. It is worth mentioning that for $\gamma \neq 0$, in equations (5.6)-(5.7), the convection terms are transposed to the right hand side so that they reduce to the form (2.1) as

$$\frac{\partial u}{\partial t} = D_1 \nabla^2 u + F_1(u, v), \tag{5.8}$$

$$\frac{\partial v}{\partial t} = D_2 \nabla^2 v + F_2(u, v), \tag{5.9}$$

where $F_1(u,v) = u - u^2 - av(u-b)/(u+b) - V \cdot \nabla u$ and $F_2(u,v) = u - v - V \cdot \nabla v$. Simulations are carried out adopting the same strategy as in [53], where a convection-diffusion-reaction equation was discretized by converting it into a purely diffusion equation.

In order to study the effect of strain rate on the periodic rotating spiral wave, we first solve the system (5.6)-(5.7) up to the time $t = 100$ by keeping $\gamma = 0$ and set the values of other parameters as $a = 1.4$, $b = 0.002$ and $\epsilon = 0.01$, so that spiral waves exhibit periodic rotation as documented in section 5.2.2. Immediately after that, for $t > 100$, straining effect is switched on by setting $\gamma \neq 0$. It is worth mentioning that for $\gamma \neq 0$, in equations (5.6)-(5.7), the convection terms are transposed to the right hand side so that they reduce to the form (2.17). The zero-flux boundary conditions for such cases reduce to $(Vc - D\nabla c) \cdot \mathbf{n} = 0$ (c stands for either u or v), where $\mathbf{n}$ is the unit normal vector to the boundaries.

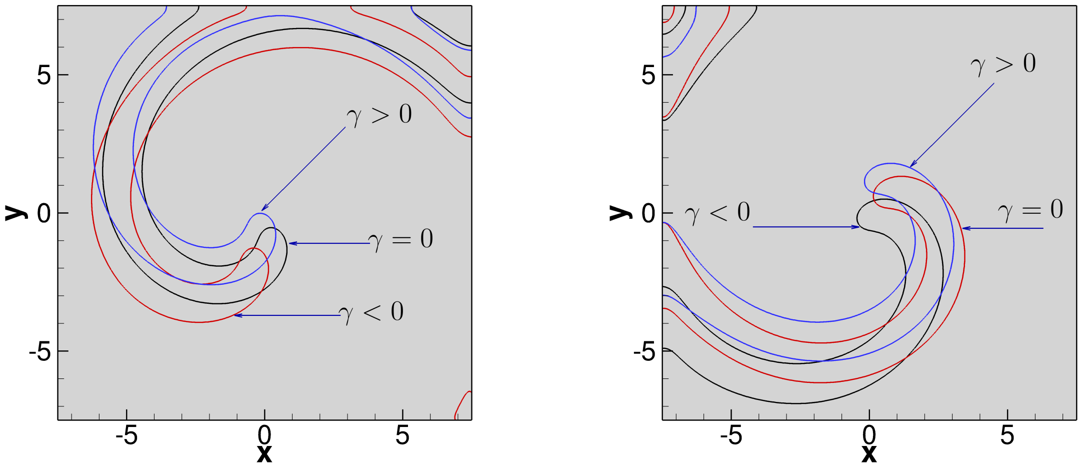

(a) (b)

Figure 5.7: (a)-(b) Deformations and stretching under the effect of strain rate at different times $t = 162.0$ and $t = 164.0$ respectively; for the values of $\gamma = 0$, $-0.03, 0.03$.

Immediately after imposing the strain rate, the spiral waves start deforming and stretching in the principal directions $(-1, 1)$ for $\gamma > 0$ and $(-1, -1)$ for $\gamma < 0$. In figures 5.7(a) and (b), we depict the contours of $u = 0.5$ for $\gamma = -0.03$, 0 and 0.03 at two time stations $t = 162.0$ and $t = 164.0$ respectively. It can be observed from the these figures that with respect to the patterns obtained corresponding to $\gamma = 0$, the pattern is deforming and stretching in the principal directions $(-1, -1)$ and $(-1, 1)$ of the strain rate tensor, corresponding to a negative (viz. $\gamma = -0.03$) and a positive value of γ (viz. $\gamma = 0.03$) respectively.

Moreover, under the effect of strain rates the spiral tip trajectories start performing non-periodic motions as seen from the phase diagrams plotted in figures 5.8(a)-(b). One can clearly see that the tip trajectories corresponding to non-zero values of γ are not closed which affirms their non-periodic motion. The presence of strain does not have any effect on the direction of rotation as the tip trajectories are always seen to perform an anticlock-wise rotation for all the values of γ. Besides, when the magnitude of γ is increased, it prompts more deviations of the tip trajectories towards the left corners of the computational domain: to the bottom left for negative (see figures 5.8(a) and top left for positive (see figures 5.8(b) values of γ.

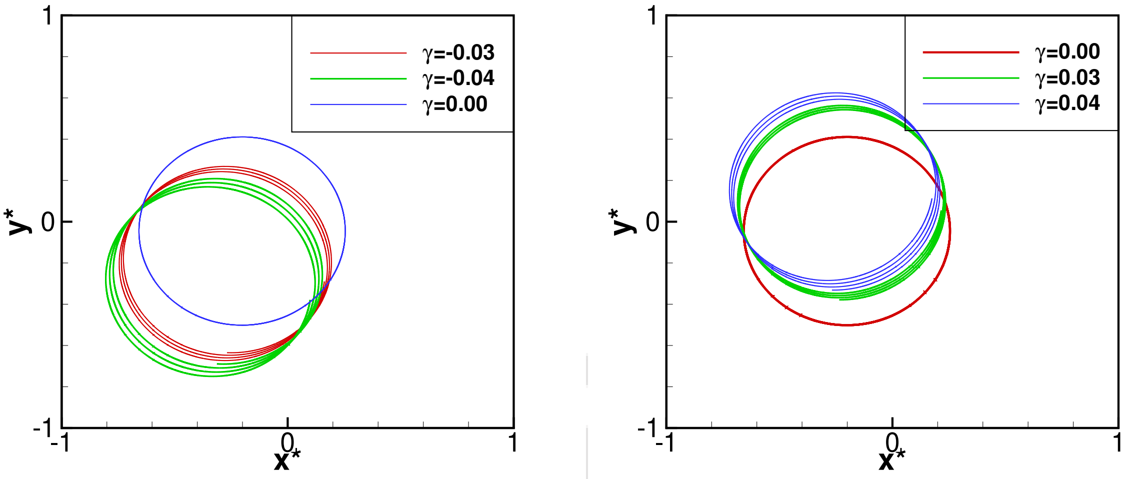

(a) (b)

Figure 5.8: (a)-(b) Spiral tip paths for different values of γ in the range $120 \leq t \leq 125$.

Further, we have explored the effect of strain rate γ on the dynamics of spiral waves by incrementally changing its values with a step size $\Delta\gamma = 0.005$ and arrive at the following three regimes after examining the computed data.

First, the no break-up regime which occurs for the values of $0 < |\gamma| \leq 0.01$ as opposed to the range $0 < |\gamma| \leq 0.05$, found in [94]. One of the obvious reasons for this discrepancy could be attributed to the very small final time, up to which computations are carried out; on the other hand, in our studies, simulations are carried out till $t = 1500$.

In figures 5.9 (e)-(f), we illustrate the effect of the strain rate on the spiral wave tip paths for different value of $|\gamma| \leq 0.01$. From these figures it is quite evident that while the tips start from the same point, but as time progresses, for a non zero values of γ, tips start drifting in different directions. For a positive values of γ the tips drift towards the top left corner, while for negative values of γ they drift towards the bottom left corner. After some finite interval time for all values $|\gamma| \leq 0.01$, spiral waves were seen perform the periodic motions; as such the tip trajectories eventually end up as closed curves. Further the graphs of x^* and y^* with time t displayed in figures 5.9(a)-(d), yield similar conclusion. For a more clear view, we analyse the data at a later time for very short time ranges in figure 5.10. The time history plots of the tip coordinate x^* in figure 5.10(a) in the interval $1465 \leq t \leq 1480$ clearly exhibits the periodicity of the tip coordinate x^*. Next, in figure 5.10(b), we present the tip trajectories for the different values of $|\gamma| \leq 0.01$, at later time range $1400 \leq t \leq 1480$ where one can clearly see that they are closed curves for all the values of $|\gamma| \leq 0.01$. Furthermore, the existence of only one dominant mode of frequencies in the power spectrum plots of x^* and y^* in figures 5.10(c) and 5.10(d) respectively, for all the values of γ considered here reaffirm the periodicity of the spiral waves at later times.

We observe that the spiral waves settle into periodic motions for the whole range of γ values $0 < |\gamma| \leq 0.01$ at later times. However, each of their tip follows different trajectories from each other and one's obtained with $\gamma = 0$. Remarkably, all of them have the same time period of rotation as demonstrated by the power spectrum plots of x^* and y^* in figures 5.10(c) and (d) respectively. Here, we can see the presence of a single mode of dominating frequency corresponding to a frequency 0.650001.

In order to demonstrate the behaviour of spiral waves within one complete periodic cycle without and with the straining effect, a proximate view of spiral waves evolution corresponding to $\gamma = 0.0$ and 0.01 are presented in figures 5.11(a1)-(a6) and 5.11(b1)-(b6) respectively. In both sequences of the figures 5.11(a1)-(a6) and 5.11(b1)-(b6), each pair of consecutive figures in the sequence is separated by the time step $T/5$, where $T = 1/0.650001 \approx 1.5384$ is the time period. As stated earlier, the introduction of straining effect has clearly induced drift and deformation into the spiral wave patterns (figures 5.11(b1)-(b6)) which is absent in the case of $\gamma = 0.0$.

From the above discussions, we conclude that in the no break-up regime $0 < |\gamma| \leq 0.01$, initially the spiral waves drift towards either top left ($\gamma > 0$) or bottom left ($\gamma < 0$) for a certain duration of time under the straining effect. Then they slightly change tracks and eventually start performing periodic rotations exactly with the same period for $\gamma = 0$. For different values of γ spiral wave tip paths follow different paths. Throughout the whole duration, the rotating spiral waves remain in tact, in other words, there is no break-up in them.

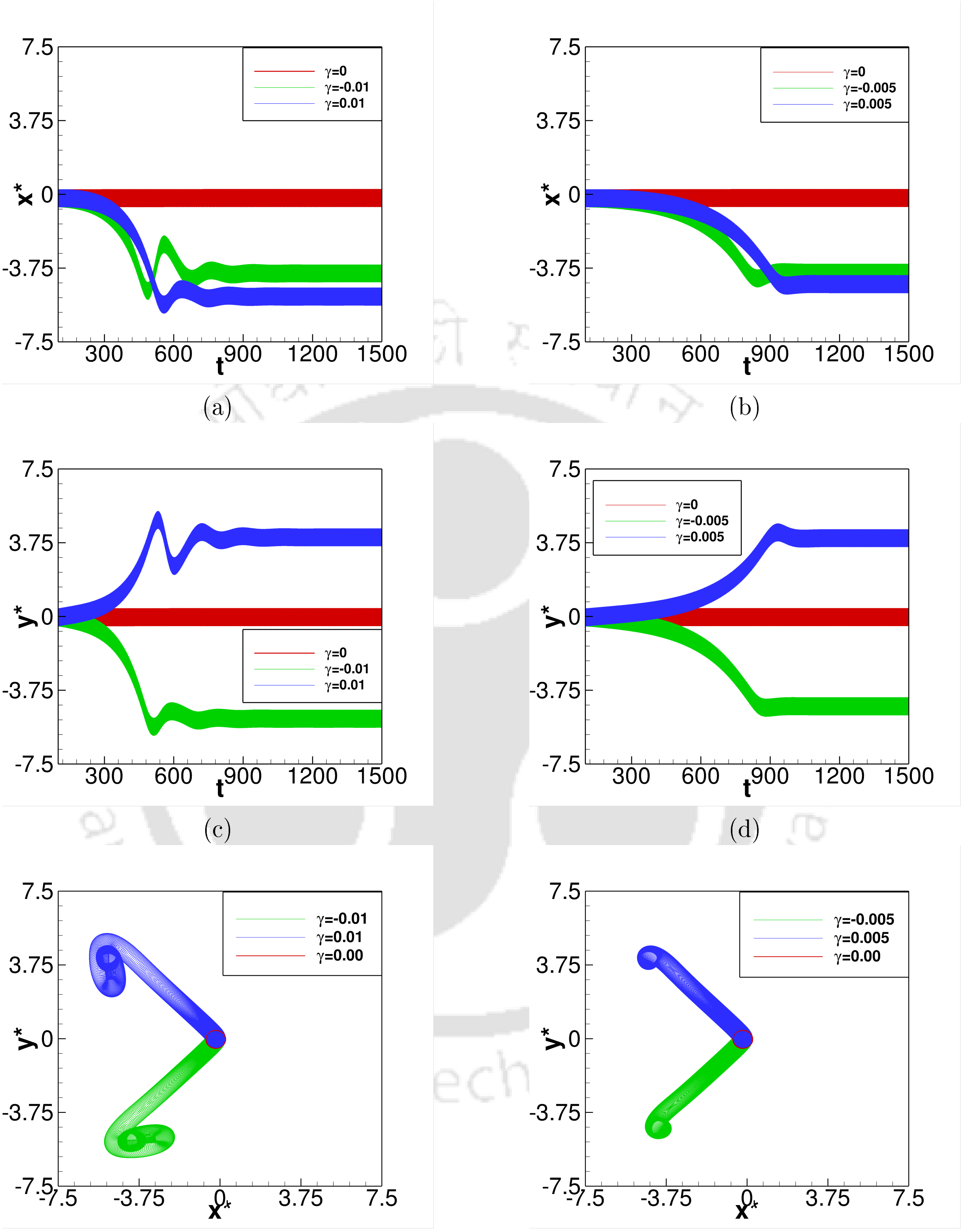

(a) (b)

(c) (d)

(e) (f)

Figure 5.9: Dynamics of spiral wave in no break up regime: (a)-(b) time history of tip coordinate x^* in the range $100 \leq t \leq 1500$, (c)-(d) time history of tip coordinate y^* in the range $100 \leq t \leq 1500$ and (e)-(f) phase diagram of tip coordinates (x^*, y^*) in time $100 \leq t \leq 1500$.

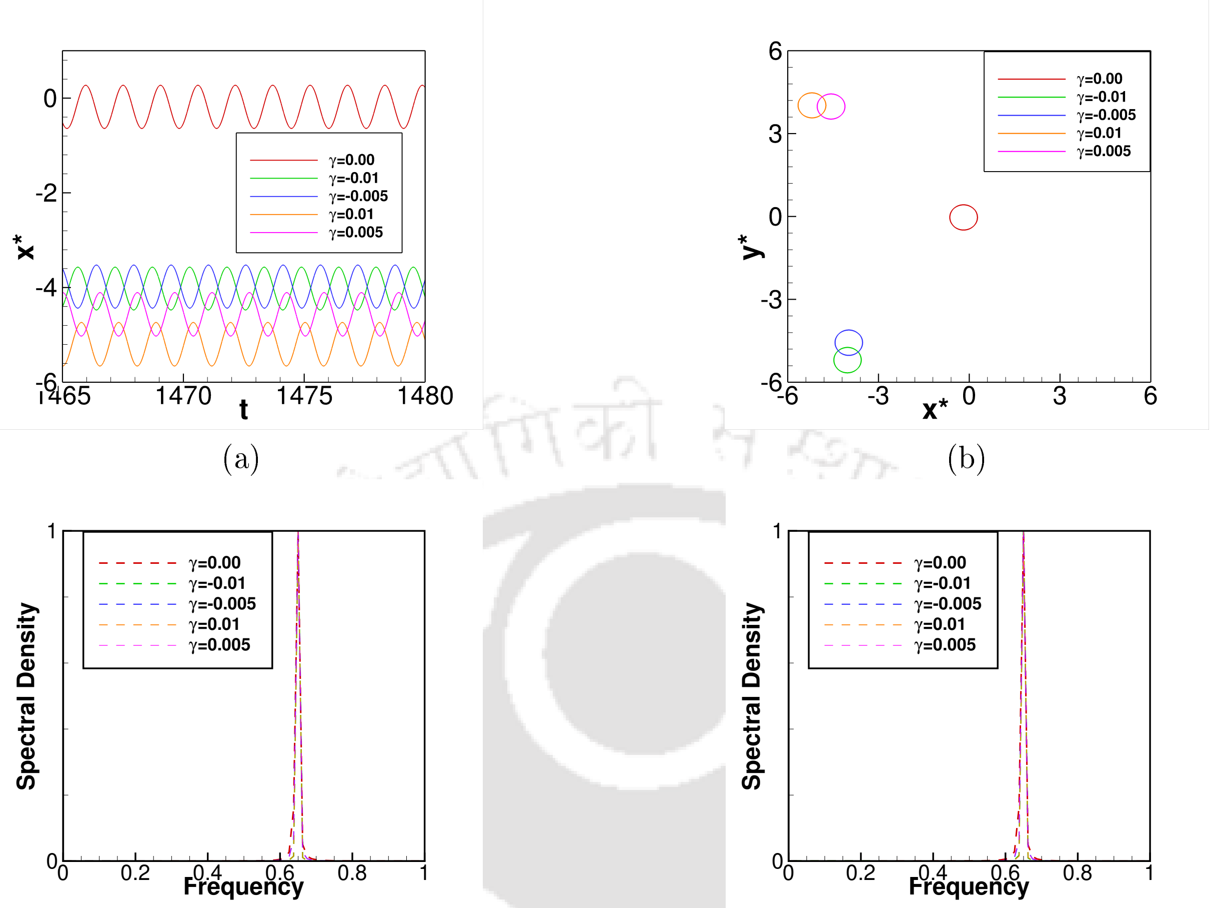

(a) (b)

(c) (d)

Figure 5.10: Dynamics of spiral wave in the no break regime: (a) time history plot of tip coordinate x^* in the range $1465 \leq t \leq 1480$, (b) phase diagram of tip coordinates (x^*, y^*) in the range $1400 \leq t \leq 1480$, (c)-(d) power spectrum for x^* and y^* respectively for time $1400 \leq t \leq 1480$.

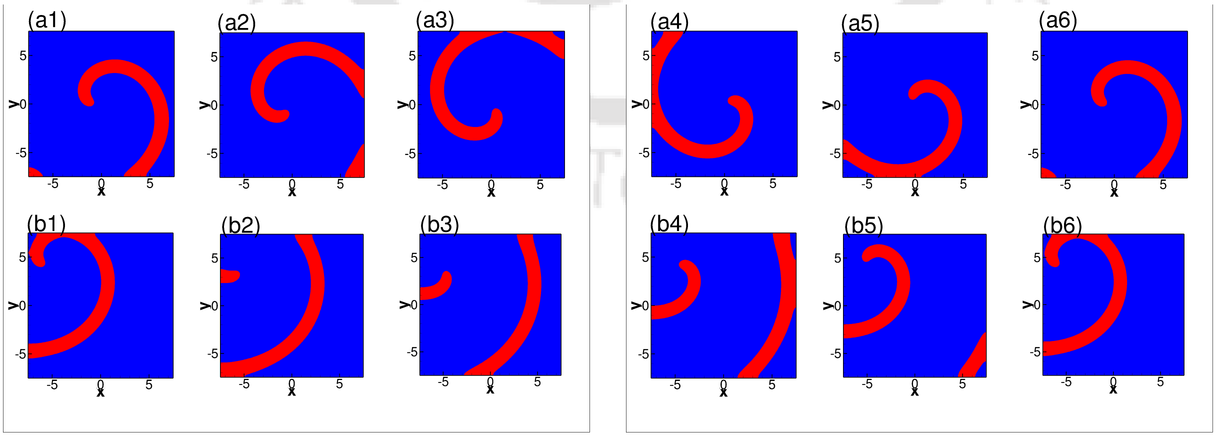

Figure 5.11: Evolution of spiral patterns $(u = 0.5)$ for one complete periodic cycle starting from $t_0 = 1400.3076$ for the values $\gamma = 0.00$ (top row) and $\gamma = 0.01$ (bottom row): (a1)-(b1) t_0, (a2)-(b2) $t_0 + T/5$, (a3)-(b3) $t_0 + 2T/5$, (a4)-(b4) $t_0 + 3T/5$, (a5)-(b5) $t_0 + 4T/5$ and (a6)-(b6) $t_0 + 5T/5$.

The next regime is characterized as the transitional regime. Our study reveals that the transitional regime starts from a value $|\gamma| = 0.015$ contrary to the the earlier studies [94] which claimed it to have started from $|\gamma| = 0.06$. Clear evidence of this can be found from figure 5.12 where one can see the spiral waves stretching and deforming in the direction (-1, 1) for the value $\gamma = 0.015$. The deformation of the spiral waves continues till the curved arm located at the top left corner of the domain (see figures 5.12(a), (c)) approaches the bottom right corner the domain (see figures 5.12(f)-(h)) and no pattern was observed in the computational domain at time 393.50. Subsequently, no spiral wave was observed in the computational domain. Instead, patterns like the ones depicted in figures 5.13(a)-(b), plotted in sequence at time intervals $dt = 0.1$ apart, were seen to repeat at later times. This fact is affirmed by the remarkable similarity between the sequence of patterns shown in 5.13(c)-(d) in the time interval $411.00 \leq t \leq 412.10$ and their counterparts in figures 5.13(a)-(b) for $407.20 \leq t \leq 408.30$. From the sequence of events depicted in figures 5.13(a)-(b) and 5.13(c)-(d), one can clearly see that the high concentration curved fronts are initially formed at the bottom left corner and after a while at the corner in top right, each moving towards the opposite corner to interact with each other and then merge, forming a front along the direction of the vector $(-1, 1)$. Eventually the front splits into two islands moving towards the top left and bottom right corners. Interestingly, they are much thicker than the spiral wave fronts seen earlier without the draining effect (see figures 5.11(a1)-(a6). This phenomenon is seen to repeat again at much later time which can be seen from the figures 5.13(e)-(f), made for the time range $502.30 \leq t \leq 503.4$ with time step 0.01, indicating that straining leads to intermittent break ups of the initial wave.

Exactly similar behaviour of the patterns are observed for the negative values of γ (e.g $\gamma = -0.015$) from the sequence of events depicted in figures 5.14(a)-(b) and 5.14(c)-(d). The only difference here is that the initial curved fronts start from the bottom right and top left corners, eventually splitting into two islands moving towards the opposite corners, viz., the bottom left and the top right corners. The sequence of events depicted in figures

5.14(a)-(b) and 5.14(c)-(d) are almost mirror images of the ones in figures 5.13(a)-(b) and 5.13(c)-(d) about the vertical mid-line of the computational domain. This phenomenon is also seen to repeat again at much later time which can be seen from the figures 5.14(e)-(f), made for the time range $502 \leq t \leq 507.4$ with time step 0.01, indicating that straining leads to intermittent break ups of the initial wave. Note that before reaching the stage as shown in figures 5.13-5.14, the spiral wave was seen to drift in the directions of either the top left or bottom left corners with simultaneous stretching and deforming. This fact can also be seen from figures 5.15(a) and (b), where the spiral wave tip paths have been depicted for $\gamma = 0.015$ and -0.015 respectively, for a certain time span. The same drift phenomenon of the spiral wave induced by the effect of excitability gradients and external fields were are also observed in notable works of [13, 64, 76].

A higher value of $|\gamma|$ aids the spiral waves to cover a longer distance for the same duration of time. This can be seen from the tip trajectories for different $|\gamma|$ values in figures 5.15(c)-(d) for time duration $100 \leq t \leq 130$. Another important observation coming out of our study is that for the values of $0.015 \leq |\gamma| \leq 0.115$, the behaviour of the wave fronts are not exactly periodic as claimed by [94]. Our claim is corroborated by the spectral density analysis of the time history of u at the center of the computational domain as seen in figure 5.16. The occurrence of a second dominant mode of frequency for these values of γ confirms this fact. The reason for the discrepancy of the results in [94] and ours could be the final time considered in their study, which is much smaller the one considered here, viz., $t = 500.00$.

In order to substantiate our claim that the transitional regime exists for values of $|\gamma| = 0.115$, we show the wave patterns for the value of $\gamma = -0.115$ in figures 5.17(a1)-(a32). One can see from these figures 5.17(a1)-(a16) and 5.17(a17)-(a32), corresponding to the time intervals $155.70 \leq t \leq 157.20$ and $157.50 \leq t \leq 159.00$ respectively, that the repetitions take place much faster than the previously seen patterns for smaller values of γ. For example, while there was a gap of $\Delta t = 3.8$ for $\gamma = -0.015$ (see figure 5.13), this gap was only $\Delta t = 0.3$ for $\gamma = -0.115$. Similar behaviour was observed for the corresponding positive value of $\gamma = 0.115$.

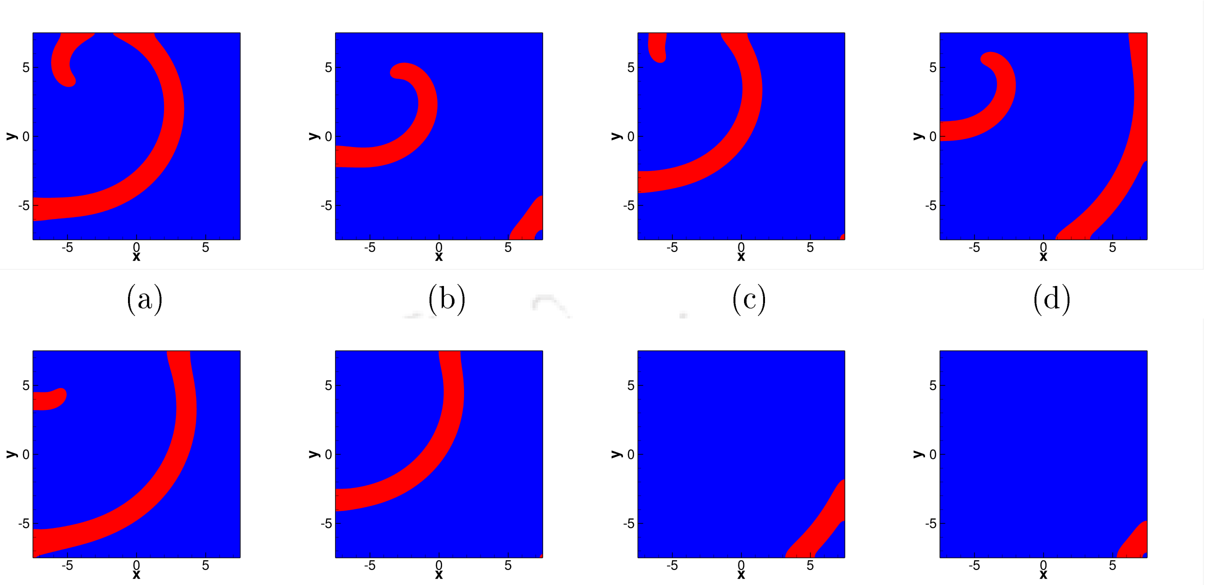

(a) (b) (c) (d)

(e) (f) (g) (h)

Figure 5.12: Patterns for the concentration of $u(= 0.5)$ for the value of $\gamma = 0.015$ at different time stations: (a) $t = 361.00$, (b) $t = 362.00$, (c) $t = 381.00$, (d) $t = 382.00$, (e) $t = 383.00$, (f) $t = 392.00$, (g) $t = 393.20$ and (h) $t = 393.40$.

Finally, we explore the break-up regime, starting our computation with a value of $|\gamma| = 0.12$, results of which are displayed in figure 5.18. One can see from figures 5.18(a)-(h) that, opposed to the merging and break-up taking place from one corner to the opposite one for $0.015 \leq |\gamma| \leq 0.115$ (figures 5.13-5.14), the spiral wave break-up occurs for the values of $\gamma = 0.12$ and $\gamma = -0.12$ in no particular direction. Moreover, unlike the transitional regime, no repetition of the patterns is seen in these cases.

Thus, based on our computation, we conclude the existence of three regimes and their corresponding ranges: no break, the transitional and break up regimes are $0 < |\gamma| \leq 0.01$, $0.015 \leq |\gamma| \leq 0.115$ and $|\gamma| \geq 0.12$ respectively.

The importance of the above findings can be gauged by the fact that a stationary (periodic) and a meandering spiral wave may correspond to monomorphic and polymorphic tachycardia respectively, which has been conjectured by several clinical studies [39,86,93]. These studies further observe that ventricular fibrillation, which is the single most common cause of sudden cardiac death, is always preceded by ventricular tachycardia. Thus the transition from a stationary to a drifting or meandering tip and then to spiral wave break-up may correspond to the transition from monomorphic to polymorphic arrhythmia and then to fibrillation and sudden cardiac death [40, 65]

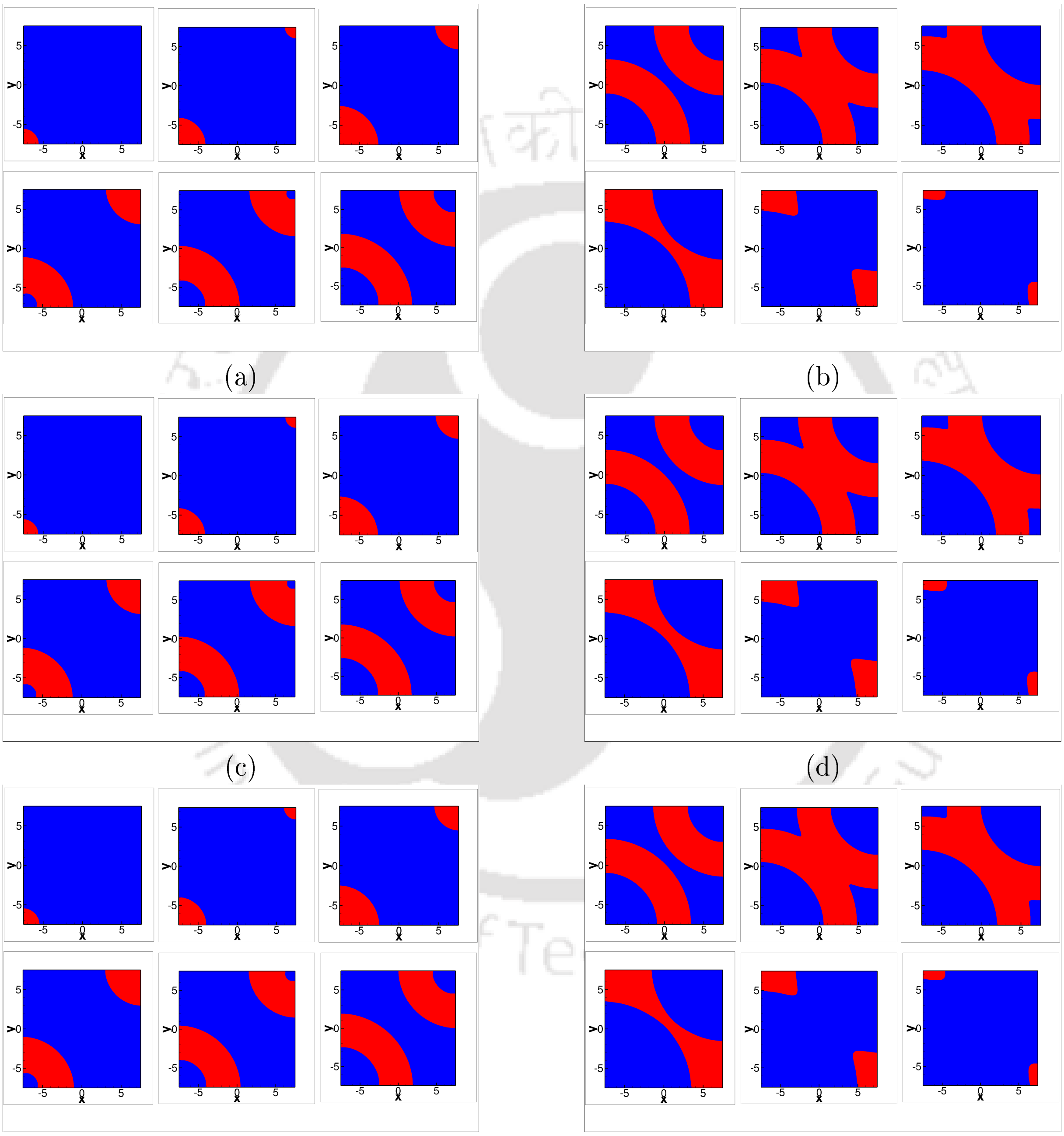

(a) (b) (c) (d) (e) (f)

Figure 5.13: Wave patterns for $u(=0.5)$ for the value of $\gamma = 0.015$ at time stations: (a) $t = 407.20-407.70$, (b) $t = 407.80-408.30$, (c) $t = 411.00-411.50$, (d) $t = 411.60-412.10$, (e) $t = 502.30 - 502.80$ and (f) $t = 502.90 - 503.40$. In each figure, figures are separated by the time difference 0.10, left to right and then top to bottom.

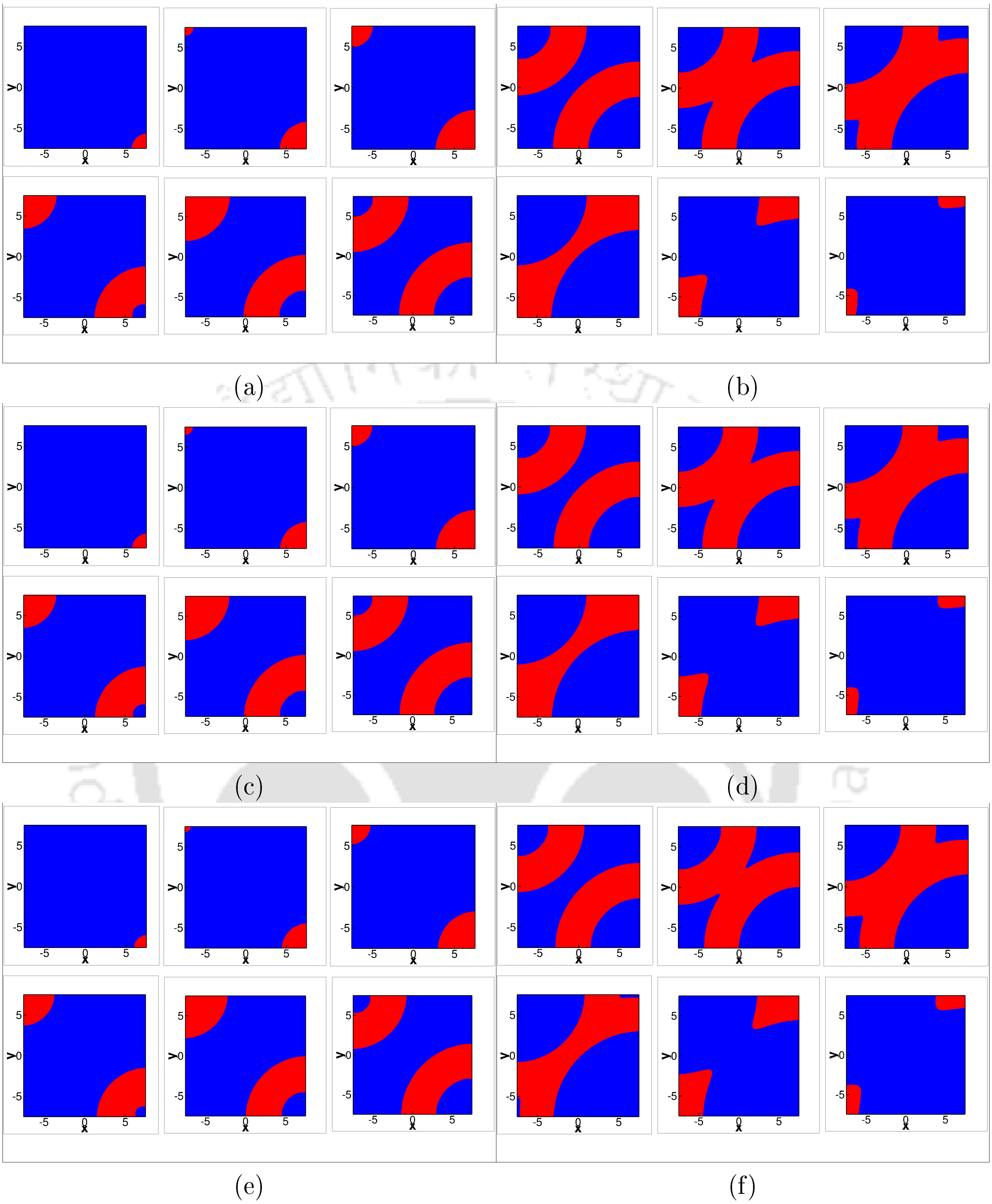

(a) (b)

(c) (d)

(e) (f)

Figure 5.14: Wave patterns for $u(=0.5)$ for the value of $\gamma = -0.015$ at time stations: (a) $t = 379.90 - 380.40$, (b) $t = 380.50 - 381.00$, (c) $t = 383.70 - 384.20$, (d) $t = 384.30 - 384.80$, (e) $t = 501.60 - 502.10$ and (f) $t = 502.20 - 502.70$. In each figure, figures are separated by the time difference 0.10, left to right and then top to bottom.

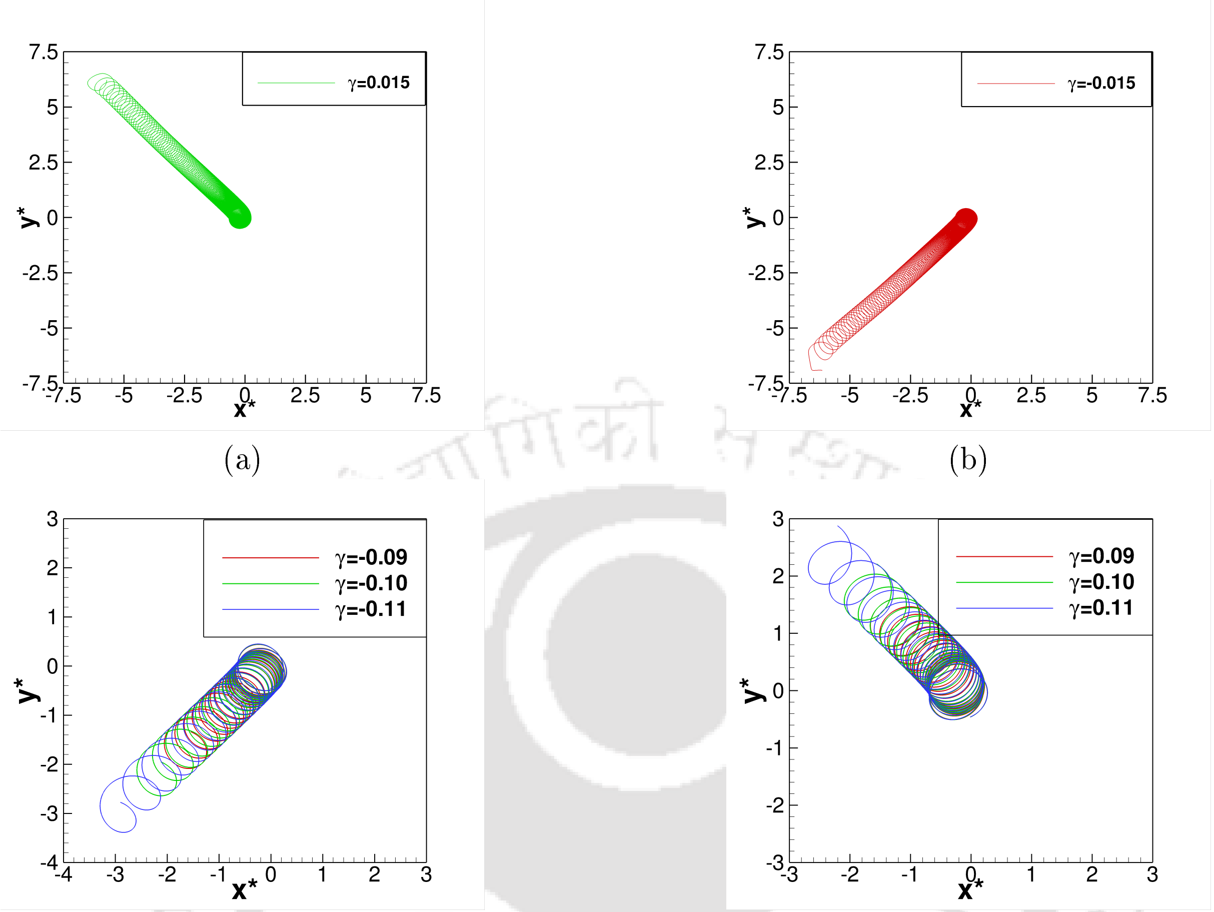

(a) (b)

(c) (d)

Figure 5.15: Spiral tip paths for the values of γ:(a) $\gamma = 0.015$ for $100 \leq t \leq 363$, (b) $\gamma = -0.015$ for $100 \leq t \leq 391$ and (c)-(d) for the time range $100 \leq t \leq 130$..

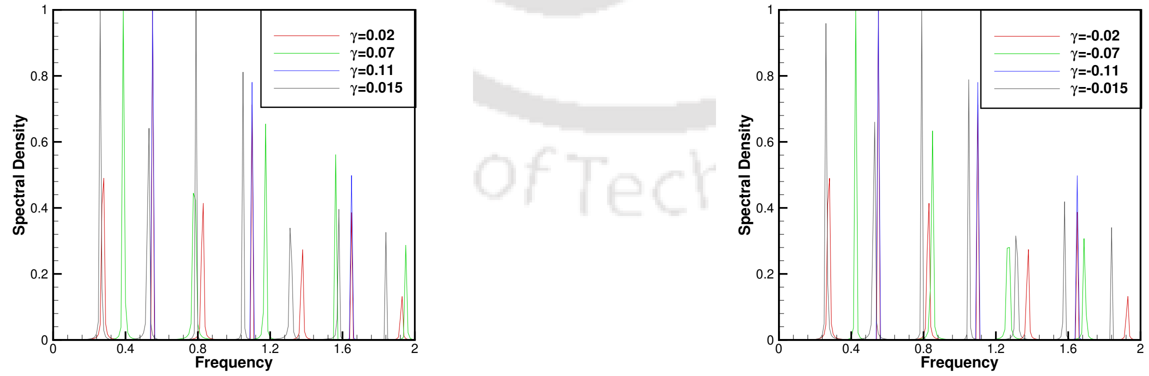

(a) (b)

Figure 5.16: Power spectra plots for the time history of u for certain values values γ in the range $400 \leq t \leq 500$: (a) $\gamma = 0.015$, 0.02, 0.07, 0.11 and (b) $\gamma = -0.015$ -0.02, -0.07, -0.11.

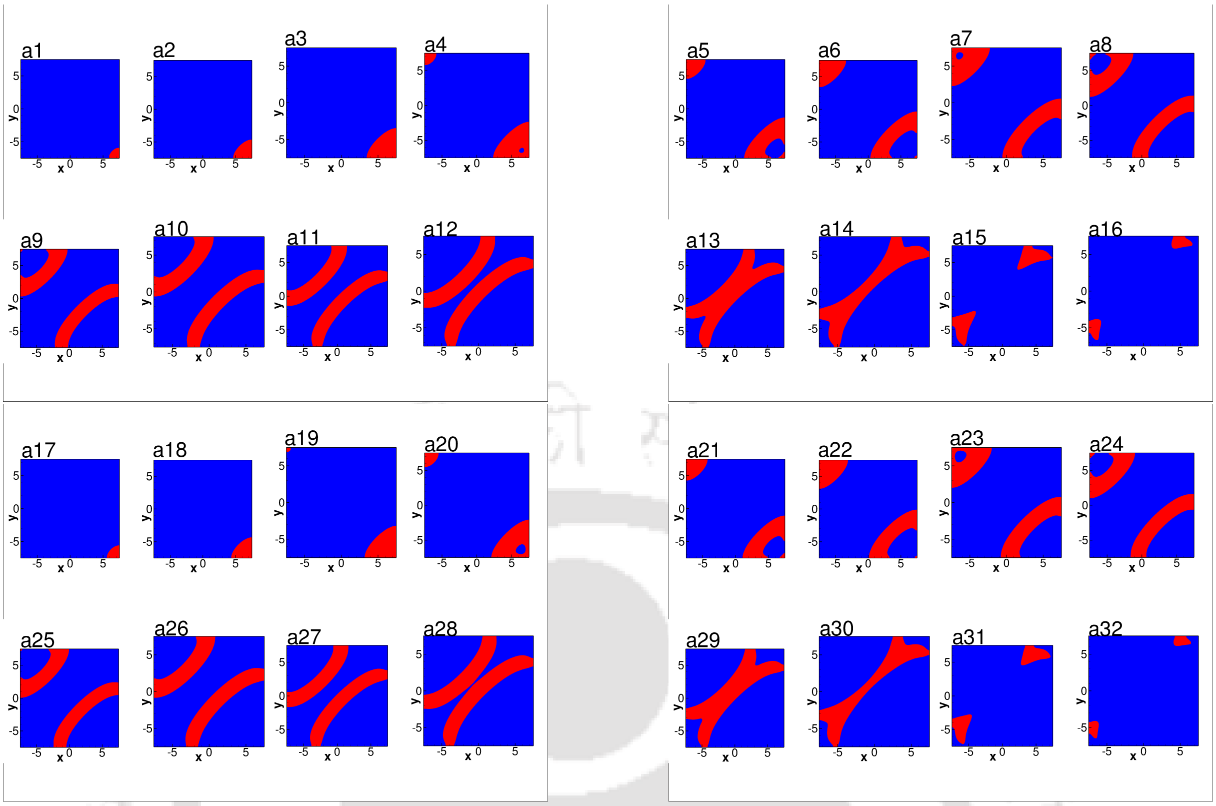

Figure 5.17: Patterns for the variable $u(=0.5)$ while the value of $\gamma = -0.115$ at different time stations: (a1)-(a16) $155.70 \leq t \leq 157.20$ and (a17)-(a32) $157.50 \leq t \leq 159.00$.

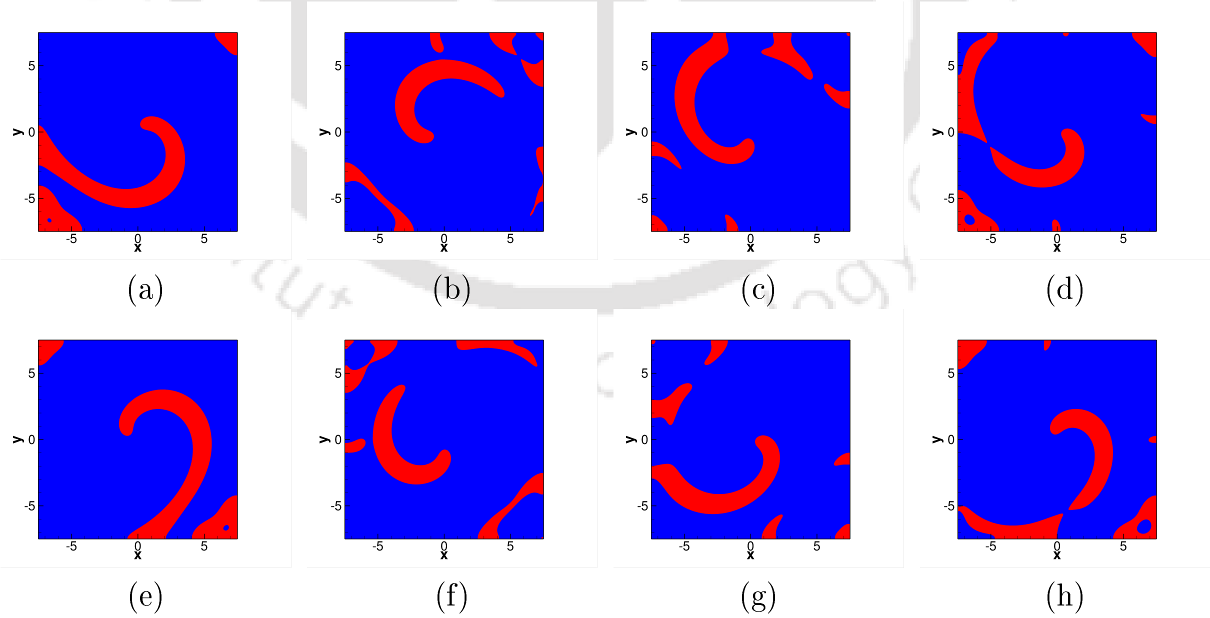

(a) (b) (c) (d)

(e) (f) (g) (h)

Figure 5.18: Patterns for the concentration of $u(=0.5)$ at different time stations: (a) $t = 102.12$, (b) $t = 104.40$, (c) $t = 104.70$, (d) $t = 105.00$, (a) $t = 102.52$, (b) $t = 104.75$, (c) $t = 105.08$, (d) $t = 105.42$. (a)-(d) for $\gamma = 0.12$ and (e)-(h) for $\gamma = -0.12$.

5.3 Conclusions

In this chapter, firstly we have probed the efficiency of the reconstructed HOC scheme, now for the Oregonator model of excitable media by establishing grid independence and convergence rate of the computed solutions. Further, we have carried out a comprehensive power spectral density analysis to investigate the parameter effect on spiral dynamics by exploiting the spiral tip as a major tool. Moreover, we have accomplished the stability analysis of rotating wave solutions and found that both periodic as well as meandering wave solutions are stable ones.

Next, we have studied the effect of straining on the dynamics of periodic rotating spiral wave, which was seen to generate a host of complex patterns in different regimes. Based on the characteristics of the patterns, our study confirms all the three regimes observed in the earlier studies, viz., the no break-up, the transitional, and the break-up. However, the time range of our projected regimes are entirely different from the earlier ones reported in the literature [94], where computations were performed for a very small time range with lower order schemes.

In the no break-up regime; immediately after implementing the non zero value of γ, spiral waves start drifting towards one of the corners, either top left (for $\gamma > 0$) or bottom left (for $\gamma < 0$), for a certain durations of times. They were eventually seen to settle into a periodic motion for all values of $|\gamma| \leq 0.01$. Interestingly, though varying the value of γ led to different spiral tip trajectories, all of them performed periodic rotation with the exactly the same time period equal to that of the waves without straining.

In the transitional regime; immediately after implementing the non zero value of γ, the spiral waves start drifting towards one of the corners either top left (for $\gamma > 0$) or bottom left (for $\gamma < 0$), accompanied by deformation and stretching, for certain durations of times and eventually transformed into thick curved fronts. The cycles of patterns are seen to repeat after certain time gaps. The last regime is categorized as the break-up regime, where the spiral waves break up at a very initial stage and the wave fronts start deforming randomly in no particular direction and no repetitions are seen to occur.

Chapter 6

HOC SCHEME FOR 3D UNSTEADY REACTION DIFFUSION EQUATIONS

6.1 Introduction

The previous chapters were concerned with the application of HOC finite difference scheme on simulating spiral waves in excitable media where we had reconstructed a recently developed scheme by Kalita [53] to discretize the governing reaction-diffusion (RD) equations in two dimensions. In the process, we have also demonstrated the limitations of the explicit schemes in accurately capturing the underlying physical processes governed by the RD equations. The superiority of the HOC scheme was clearly evident from all the simulations carried out in the preceding chapters. Therefore it makes sense to extend the scheme for 2D RD equations in [53] to three dimensions to simulate the 3D counterpart of spiral waves that is known as scroll waves. This chapter is concerned with the development of an HOC scheme for discretizing the 3D unsteady non-linear reaction-diffusion equations, which could be very useful in simulating scroll waves in excitable media.

There has also been a reasonable amount of experimental and numerical studies on the dynamics of scroll wave patterns in the 3D excitable media [4, 70, 71, 73, 80, 89, 91, 111, 117]. Likewise in the case of spiral waves, most of these numerical results on scroll wave dynamics have been obtained by lower order accurate schemes. The mathematical models which have been used quite frequently in order to perform the numerical computations on

TH-2268_136123014

the scroll wave dynamics, are the Barkley, the Fitz-Hugh Nagumo, and the Oregonator models. These models, which are constituted by the systems of nonlinear unsteady R-D equations can be written as

$$\frac{\partial u}{\partial t} = \frac{1}{\epsilon} f(u, v) + D_u \nabla^2 u, \tag{6.1}$$

$$\frac{\partial v}{\partial t} = g(u, v) + D_v \nabla^2 v. \tag{6.2}$$

Here ∇^2 is the 3D Laplacian operator, mathematically $\nabla^2 \equiv \partial^2/\partial x^2 + \partial^2/\partial y^2 + \partial^2/\partial z^2$, where x, y and z are coordinate variables along x-, y- and z- directions respectively. The variables u and v can be concentrations of any two reactants, or populations of two species, or excitable and recovery [4,89] variables in certain situations, etc. The nonlinear functions f and g are the reaction terms associated with the transport variables u and v, respectively. D_u and D_v are the constant diffusion coefficients corresponding to the variables u and v respectively, and t is the temporal variable. The parameter ϵ is a positive constant whose value lies between 0 to 1. It is also important to note that most of the mathematical models, which follow the Turing theory of pattern formation in 3D space, can also be written as in the form of system (6.1)-(6.2).

Instances of the use of HOC finite difference schemes to discretize the 3D nonlinear unsteady R-D equations are quite scanty in the existing literature. For example, In 2004, Mehdi Dehghan, [23] developed several numerical techniques based on the two-level fully explicit and fully implicit finite difference approximations to solve the 3D advection-diffusion equations. In 2010 [92], Jinggang, provided a new alternating direction implicit (ADI) scheme for computing the 3D parabolic equations with non-homogeneous boundary conditions, which had been extended later in the form of an HOC scheme. In 2013 [36], Ge et al. developed an implicit, unconditionally stable exponential HOC alternating direction method for discretizing the 3D unsteady convection–diffusion equations, which is spatially fourth and temporally second order accurate. In 2014, Kalita [52], derived a conditionally stable super-compact high order scheme to perform the numerical results of both unsteady and steady 3D convection-diffusion equations.

This scheme is second order accurate in time and fourth order accurate in all the spatial directions. In 2018 Yongbin et al. [37], developed a spatially fourth and temporally second order accurate, rational HOC ADI method to solve 3D unsteady convection-diffusion equations. This scheme is based on the idea of fourth order rational compact finite difference operator for spatial and Crank-Nicolson for the time discretizations. Having accomplished success with the reconstructed 2D HOC scheme to simulate spiral waves in excitable media, it is imperative that one should endeavour extending it to 3D unsteady reaction diffusion-equations, emerging from real world problems.

In this chapter, we will derive an implicit, unconditionally stable HOC scheme for solving the 3D unsteady nonlinear R-D equations with appropriate boundary conditions. This HOC scheme, which is the extension of the derived HOC scheme [53] to three dimensions, is also spatially fourth and temporally second order accurate. The scheme is employed to several test problems to check its efficiency. Interestingly, despite being in the reaction-diffusion format, the derived HOC scheme is also seen to accurately capture the solutions of unsteady convection-diffusion equations. On applying it to an unsteady convection-diffusion equation having an analytical solution, it is found out that our numerical results are extremely close to the analytical ones.

6.2 Formulation of the HOC scheme

In this section, we derive an HOC finite difference scheme to solve the 3D unsteady R-D equation for a transport variable $\psi(x, y, z, t)$ in some continuous domain (viz. cubical) with appropriate boundary conditions. The 3D unsteady R-D equation for the transport variable ψ can be written as

$$\frac{\partial \psi}{\partial t} - D\nabla^2\psi = F(x, y, z, t), \tag{6.3}$$

where $\nabla^2 \equiv \partial^2/\partial x^2 + \partial^2/\partial y^2 + \partial^2/\partial z^2$, is the 3D Laplacian operator and D is the constant diffusion coefficient. x, y and z are spatial variables in corresponding coordinates x-, y- and z-directions respectively, whereas t is the temporal variable. The function F is the nonlinear forcing term. It should be noted that each component of the system (6.1)-(6.2), is of the form of the equation (6.3).

To derive an HOC scheme for the R-D equation (6.3), we assume the domain to be cubical and the space step sizes h, k, and l are uniform in the x-, y- and z-directions respectively. We first approximate equation (6.3) by using the forward time central space (FTCS) finite difference scheme at the (i,j,k)th grid point of the domain, which can be written as

$$\left[\delta_t^+ - D\left(\delta_x^2 + \delta_y^2 + \delta_y^2\right)\right]\psi_{i,j,k} = \tau_{i,j,k} + F_{i,j,k}. \tag{6.4}$$

Here, δ_x^2, δ_y^2, and δ_z^2 are the second order central difference operators along the spatial directions x, y and z respectively, whereas δ_t^+ is the first order forward difference operator for time t. $\tau_{i,j,k}$ is the truncation error which is given by (Δt being of uniform time step),

$$\tau_{i,j,k} = \left[\frac{\Delta t}{2}\frac{\partial^2\psi}{\partial t^2} - \frac{Dh^2}{12}\frac{\partial^4\psi}{\partial x^4} - \frac{Dk^2}{12}\frac{\partial^4\psi}{\partial y^4} - \frac{Dl^2}{12}\frac{\partial^4\psi}{\partial z^4}\right]_{i,j,k} + O\left((\Delta t)^2, h^4, k^4, z^4\right). \tag{6.5}$$

Now, in order to derive temporally second and spatially fourth order accurate HOC scheme resulting from equation (6.4) for the equation (6.3), we compactly approximate the each of the leading derivative terms of the equation (6.5) by using the original R-D equation (6.3). The leading derivatives of the equation (6.5), using the original equation (6.3), can be written as,

$$\frac{\partial^2\psi}{\partial t^2} = D\left[\frac{\partial^2}{\partial x^2} + \frac{\partial^2}{\partial y^2} + \frac{\partial^2}{\partial z^2}\right]\frac{\partial\psi}{\partial t} + \frac{\partial F}{\partial t}, \tag{6.6}$$

$$\frac{\partial^4\psi}{\partial x^4} = \frac{\partial^3\psi}{\partial x^2\partial t} + \frac{\partial^4\psi}{\partial x^2\partial y^2} + \frac{\partial^4\psi}{\partial x^2\partial z^2} + \frac{\partial^4 F}{\partial x^2}, \tag{6.7}$$

$$\frac{\partial^4\psi}{\partial y^4} = \frac{\partial^3\psi}{\partial y^2\partial t} + \frac{\partial^4\psi}{\partial y^2\partial x^2} + \frac{\partial^4\psi}{\partial y^2\partial z^2} + \frac{\partial^4 F}{\partial y^2}, \tag{6.8}$$

$$\frac{\partial^4\psi}{\partial z^4} = \frac{\partial^3\psi}{\partial z^2\partial t} + \frac{\partial^4\psi}{\partial z^2\partial y^2} + \frac{\partial^4\psi}{\partial z^2\partial x^2} + \frac{\partial^4 F}{\partial z^2}. \tag{6.9}$$

Now, we approximate the derivatives of leading terms of the truncation error (6.5), given by equations (6.6)-(6.9), at the (i,j,k)th grid point, which after some simplifications, yield

$$\left[\frac{\Delta t}{2}\frac{\partial^2\psi}{\partial t^2}\right]_{i,j,k} = \frac{D\Delta t}{2}\left[\delta_x^2 + \delta_y^2 + \delta_z^2\right]\delta_t^+\psi_{ijk} + \frac{D\Delta t}{2}\delta_t^- F_{i,j,k}, \tag{6.10}$$

$$\left[-\frac{Dh^2}{12}\frac{\partial^4\psi}{\partial x^4}\right]_{i,j,k} = -\frac{h^2}{12}\delta_x^2\delta_t^+\psi_{i,j,k} + \frac{Dh^2}{12}\delta_x^2\delta_y^2\psi_{i,j,k} + \frac{Dh^2}{12}\delta_x^2\delta_z^2\psi_{i,j,k} + \frac{Dh^2}{12}\delta_x^2 F_{i,j,k}, \quad (6.11)$$

$$\left[-\frac{Dk^2}{12}\frac{\partial^4\psi}{\partial y^4}\right]_{i,j,k} = -\frac{k^2}{12}\delta_y^2\delta_t^+\psi_{i,j,k} + \frac{Dh^2}{12}\delta_y^2\delta_x^2\psi_{i,j,k} + \frac{Dh^2}{12}\delta_y^2\delta_z^2\psi_{i,j,k} + \frac{Dh^2}{12}\delta_x^2 F_{i,j,k}, \quad (6.12)$$

$$\left[-\frac{Dk^2}{12}\frac{\partial^4\psi}{\partial z^4}\right]_{i,j,k} = -\frac{l^2}{12}\delta_z^2\delta_t^+\psi_{ijk} + \frac{Dh^2}{12}\delta_z^2\delta_x^2\psi_{ijk} + \frac{Dh^2}{12}\delta_z^2\delta_y^2\psi_{ijk} + \frac{Dh^2}{12}\delta_x^2 F_{ijk}, \quad (6.13)$$

where δ_t^- is the first order temporal backward difference operator. Note that we use forward temporal difference operators for $\psi(x, y, z, t)$ and backward difference for $F(x, y, z, t)$. Using the approximations from (6.10)-(6.13) in the equation (6.5), and after simplifying, the truncation error $\tau_{i,j,k}$ becomes:

$$\begin{aligned}\tau_{i,j,k} = &\left[\left(\frac{D\Delta t}{2} - \frac{h^2}{12}\right)\delta_x^2 + \left(\frac{D\Delta t}{2} - \frac{k^2}{12}\right)\delta_y^2 + \left(\frac{D\Delta t}{2} - \frac{l^2}{12}\right)\delta_z^2\right]\delta_t^+\psi_{i,j,k} \\ &+ \left[\left(\frac{D(h^2+k^2)}{12}\right)\delta_x^2\delta_y^2 + \left(\frac{D(k^2+l^2)}{12}\right)\delta_y^2\delta_z^2 + \left(\frac{D(l^2+h^2)}{12}\right)\delta_z^2\delta_x^2\right]\psi_{i,j,k} \\ &+ \left[\frac{\Delta t}{2}\delta_t^- + \frac{h^2}{12}\delta_x^2 + \frac{k^2}{12}\delta_y^2 + \frac{l^2}{12}\delta_z^2\right]F_{i,j,k} + O\left((\Delta t)^2, h^4, k^4, l^4\right). \end{aligned} \quad (6.14)$$

Substituting the value of the truncation error $\tau_{i,j,k}$ from the equation (6.14), in the equation (6.4), an $O((\Delta t)^2, h^4, k^4, l^4)$ approximation for the equation (6.3) on a $(19, 7)$ stencil can be obtained as

$$\begin{aligned}&\left[1 + \left(\frac{h^2}{12} - \frac{D\Delta t}{2}\right)\delta_x^2 + \left(\frac{k^2}{12} - \frac{D\Delta t}{2}\right)\delta_y^2 + \left(\frac{l^2}{12} - \frac{D\Delta t}{2}\right)\delta_z^2\right]\delta_t^+\psi_{i,j,k} \\ &= \left[\left(\frac{D(h^2+k^2)}{12}\right)\delta_x^2\delta_y^2 + \left(\frac{D(k^2+l^2)}{12}\right)\delta_y^2\delta_z^2 + \left(\frac{D(l^2+h^2)}{12}\right)\delta_z^2\delta_x^2\right]\psi_{i,j,k} \\ &+ D\left[\delta_x^2 + \delta_y^2 + \delta_z^2\right]\psi_{ijk} + \left[1 + \frac{\Delta t}{2}\delta_t^- + \frac{h^2}{12}\delta_x^2 + \frac{k^2}{12}\delta_y^2 + \frac{l^2}{12}\delta_z^2\right]F_{i,j,k} + O\left((\Delta t)^2, h^4, k^4, l^4\right). \end{aligned} \quad (6.15)$$

The HOC scheme given by (6.15), is unconditionally stable and details of the stability analysis can found in [53]. Now, we explore the solution of the algebraic system emerging from the newly proposed HOC scheme (6.15), which can be written as,

$$\begin{aligned}&\sum_{n_1=-1}^{n_1=1}\sum_{n_2=-1}^{n_2=1}\sum_{n_3=-1}^{n_3=1}\alpha_{i+n_1,j+n_2,k+n_3}\psi^{n+1}_{i+n_1,j+n_2,k+n_3} \\ &= \sum_{n_1=-1}^{n_1=1}\sum_{n_2=-1}^{n_2=1}\sum_{n_3=-1}^{n_3=1}\beta_{i+n_1,j+n_2,k+n_3}\psi^{n}_{i+n_1,j+n_2,k+n_3} + G^n_{i,j,k} \end{aligned} \quad (6.16)$$

where $G^n_{i,j,k} = \left[1 + \frac{\Delta t}{2}\delta_t^- + \frac{h^2}{12}\delta_x^2 + \frac{k^2}{12}\delta_y^2 + \frac{l^2}{12}\delta_z^2\right] F_{i,j,k}$. $\alpha_{i+n_1,j+n_2,k+n_3} = 0$ when at least two of the indices n_1, n_2 and n_3 are non zero simultaneously, and $\beta_{i+n_1,j+n_2,k+n_3} = 0$ when all indices n_1, n_2 and n_3 are non zero simultaneously. $\alpha's$ and $\beta's$ are all constants for given space steps h, k and l, and time step Δt. The left and right hand sides coefficients of the HOC scheme (6.16), are given by

$$\alpha_{i+1,j,k} = \alpha_{i-1,j,k} = \left(\frac{1}{12\Delta t} - \frac{D}{2h^2}\right), \quad \alpha_{i,j+1,k} = \alpha_{i,j-1,k} = \left(\frac{1}{12\Delta t} - \frac{D}{2k^2}\right), \tag{6.17}$$

$$\alpha_{i,j,k-1} = \alpha_{i,j,k-1} = \left(\frac{1}{12\Delta t} - \frac{D}{2l^2}\right), \quad \alpha_{i,j,k} = \left(\frac{1}{2\Delta t} + \frac{D}{h^2} + \frac{D}{k^2} + \frac{D}{l^2}\right), \tag{6.18}$$

$$\beta_{i+1,j+1,k} = \beta_{i-1,j+1,k} = \beta_{i-1,j+1,k} = \beta_{i-1,j-1,k} = \frac{D\left(h^2+k^2\right)}{12h^2k^2}, \tag{6.19}$$

$$\beta_{i,j+1,k+1} = \beta_{i,j+1,k-1} = \beta_{i,j-1,k+1} = \beta_{i,j-1,k-1} = \frac{D\left(k^2+l^2\right)}{12k^2l^2}, \tag{6.20}$$

$$\beta_{i+1,j,k+1} = \beta_{i+1,j,k-1} = \beta_{i-1,j,k+1} = \beta_{i-1,j,k-1} = \frac{D\left(l^2+h^2\right)}{12l^2h^2}, \tag{6.21}$$

$$\beta_{i+1,j,k} = \beta_{i-1,j,k} = \left[-\left(\frac{2D\left(h^2+k^2\right)}{12h^2k^2}\right) - \left(\frac{2D\left(l^2+h^2\right)}{12l^2h^2}\right) + \frac{D}{h^2}\right] \tag{6.22}$$

$$\beta_{i,j+1,k} = \beta_{i,j-1,k} = \left[-\left(\frac{2D\left(k^2+l^2\right)}{12k^2l^2}\right) - \left(\frac{2D\left(h^2+k^2\right)}{12h^2k^2}\right) + \frac{D}{k^2}\right] \tag{6.23}$$

$$\beta_{i,j,k+1} = \beta_{i,j,k-1} = \left[-\left(\frac{2D\left(l^2+h^2\right)}{12l^2h^2}\right) - \left(\frac{2D\left(k^2+l^2\right)}{12k^2l^2}\right) + \frac{D}{l^2}\right] \tag{6.24}$$

$$\beta_{i,j,k} = \left[\frac{4D\left(h^2+k^2\right)}{12h^2k^2} + \frac{4D\left(k^2+l^2\right)}{12k^2l^2} + \frac{4D\left(l^2+h^2\right)}{12l^2h^2} - \frac{2D}{h^2} - \frac{2D}{k^2} - \frac{2D}{l^2}\right] \tag{6.25}$$

The matrix form of the system of algebraic equations given by (6.16), can be written as

$$A\psi^{n+1} = g(\psi^n) + G^n, \tag{6.26}$$

where A is the sparse matrix of dimensions $mnp \times mnp$ for the grid size $m \times n \times p$, and ψ^{n+1} and G^n are the mnp- component vectors. It is clear from equation (6.16), the derived scheme uses seven points at the $(n+1)$th and 19 points at the nth time level, as such we term it as a $(19, 7)$ scheme. It can be seen from the above coefficients given by (6.17)-(6.18), that the matrix A, emerging from the derived HOC scheme is diagonally dominant, hence a unique solution exists for (6.26). In order to solve the above matrix equations (6.26), we have used the BiCGStab [59] iterative method, which constitute the inner iterations for each outer time step.

6.3 Numerical test problems

In the following, we apply the proposed HOC finite difference scheme (6.15) above to several test cases in order to examine its effectiveness.

6.3.1 Test problem 1

First, we obtain the numerical solution of the system nonlinear R-D equations which was also studied in [66]. They considered the system of R-D equations given by

$$\frac{\partial u}{\partial t} = D_u\left(\frac{\partial^2 u}{\partial x^2}+\frac{\partial^2 u}{\partial y^2}+\frac{\partial^2 u}{\partial z^2}\right)+f_1(u,v), \quad 0<x,y,z<1, \quad t>0 \tag{6.27}$$

$$\frac{\partial v}{\partial t} = D_v\left(\frac{\partial^2 v}{\partial x^2}+\frac{\partial^2 v}{\partial y^2}+\frac{\partial^2 v}{\partial z^2}\right)+f_2(u,v), \quad 0<x,y,z<1, \quad t>0 \tag{6.28}$$

where values of diffusion coefficients are: $D_u = D_v = 0.01$, and the nonlinear functions $f_1(u,v) = -u^4v - u/2$ and $f_2(u,v) = u^4v - v/2$, are the reactions terms for the variables u and v respectively. The initial conditions are

$$u(x,y,z,0) = 1 - \exp^{-100\left((x-0.5)^2+(y-0.5)^2+(z-0.5)^2\right)} \tag{6.29}$$

$$v(x,y,z,0) = \exp^{-100\left((x-0.5)^2+(y-0.5)^2+(z-0.5)^2\right)}. \tag{6.30}$$

while at the boundary u and v satisfy the Neumann (zero flux) boundary conditions

$$\frac{\partial u}{\partial \mathbf{n}} = \frac{\partial v}{\partial \mathbf{n}} = 0,$$

where $\mathbf{n}$ is the unit normal vector to the surfaces bounding the domain $[0,1]\times[0,1]\times[0,1]$. Note that the high non-linearity of the reaction terms f_1 and f_2, makes it extremely difficult to find exact solution of system (6.27)- (6.28).

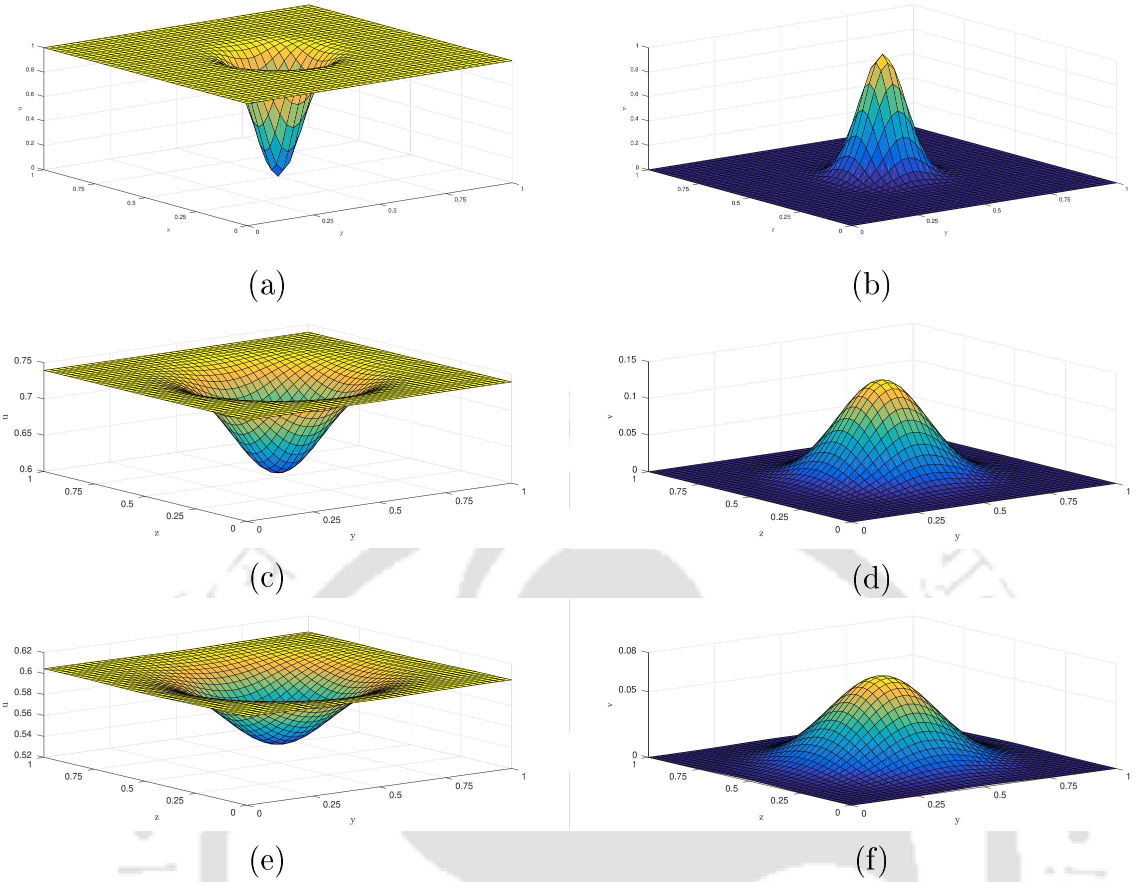

Figure 6.1: Numerical solutions at $x = 0.0$ at different time stations: (a)-(b) $t = 0.0$, (c)-(d) $t = 0.6$, and (e)-(f) $t = 1.0$. Left panel (u) and right panel (v).

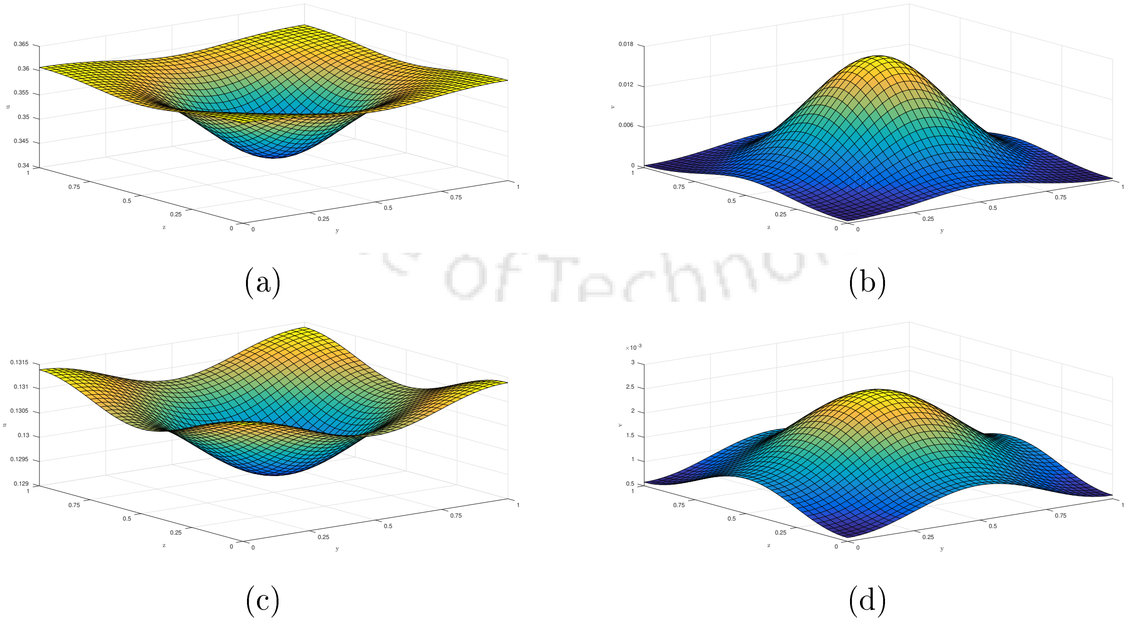

Figure 6.2: Numerical solutions at $x = 0.0$ at different time stations: (a)-(b) $t = 2.0$, (c)-(d) $t = 4.0$. Left panel (u) and right panel (v).

We demonstrate the time evolution of numerical results in figures 6.1-6.2, obtained on grid size $41 \times 41 \times 41$, with space steps $h = k = l = \frac{1}{40}$, using a time step $\Delta t = 0.025$. The numerical results obtained at $x = 0.05$ for u and v corresponding to final times $t = 0.6, 1, 2, 4$ match very well with the computed results of [66]. Due to diffusion and the negative source term present in equation (6.27), u decreases gradually, which is well evidenced in figures 6.1(c), (e) and 6.2(a), (c). Furthermore, the rate of decrease in the middle of the domain is much higher due to the large initial value of v there, which devises a deep valley that expands gradually. Likewise the peak of v declines in amplitude and broadens radially due to the diffusion and reaction. All our computed results presented in figures 6.1(d), (f) and 6.2(b), (d) are consistent with these physical phenomena.

6.3.2 Test problem 2

Next, we perform simulation of scroll waves modelled through the famous Barkley model [70], which has been widely used to study the dynamics of scroll waves in excitable media. Each component of the Barkley model can be written in the form of the equation (6.3) and can be written as,

$$\frac{\partial u}{\partial t} = D_u \left(\frac{\partial^2 u}{\partial x^2} + \frac{\partial^2 u}{\partial y^2} + \frac{\partial^2 u}{\partial z^2} \right) + \frac{1}{\epsilon} u(1-u) \left(u - \frac{v+b}{a} \right) \tag{6.31}$$

$$\frac{\partial v}{\partial t} = D_v \left(\frac{\partial^2 v}{\partial x^2} + \frac{\partial^2 v}{\partial y^2} + \frac{\partial^2 v}{\partial z^2} \right) + u - v \tag{6.32}$$

where variables u and v are excitable and recovery variable respectively. The parameter a, b and ϵ are positive constant, and the value of ϵ lies between 0 to 1 *i.e.* $(0 < \epsilon < 1)$.

For numerical computations, we have chosen a cube of size $[0, 150] \times [0, 150] \times [0, 150]$, which has been discretized using grid of size $151 \times 151 \times 151$, rendering the space steps $h = k = l = 1.0$. The parameters values are: $a = 0.84$, $b = 0.07$, $\epsilon = 0.02$, $D_u = 1.0$ and $D_v = 1.0$. For the numerical simulations, zero-flux boundary conditions have been employed at all the boundaries of the computational domain and the time step is $\Delta t = 0.01$. The initial conditions are given as follows: $u = 0.5$, $v = 0.0$ if $s_1 < 0$, $u = 0.6$, $v = 0.6$ if $s_2 < 0$, $u = 0.0$, $v = 0.5$ if $s_3 < 0$, $u = 0.0$, $v = 0.0$ if $s_4 < 0$ and

$u = v = 0$ otherwise, where s_i's are defined as: $s_i = (x-35)^2 + (y-35)^2 + (z-35)^2 - r_i^2$ for $i = 1, 2,\ 3$ and 4 with the values $r_1 = 32.5$, $r_2 = 30.5$, $r_3 = 28.5$ and $r_4 = 26.5$.

We depict the simulations emerging from HOC computations of the system (6.31)-(6.32), at different times $t = 10.0$, 30.0, 50.0, and 60.0. From the figures 6.3(a)-(b), one can see that triggered by the applied initial conditions, the scroll waves start developing at time $t = 10.0$ and they get fully resolved at a later time $t = 30.0$ (see figures 6.3(c)-(d)). We also illustrate the patterns obtained at later times $t = 50.0$ and $t = 60.0$ in figures 6.4(a)-(b) and 6.4(c)-(d), respectively. Note that we have presented the patterns of the variables u and v in the mid-plane corresponding to $x = 75.0$.

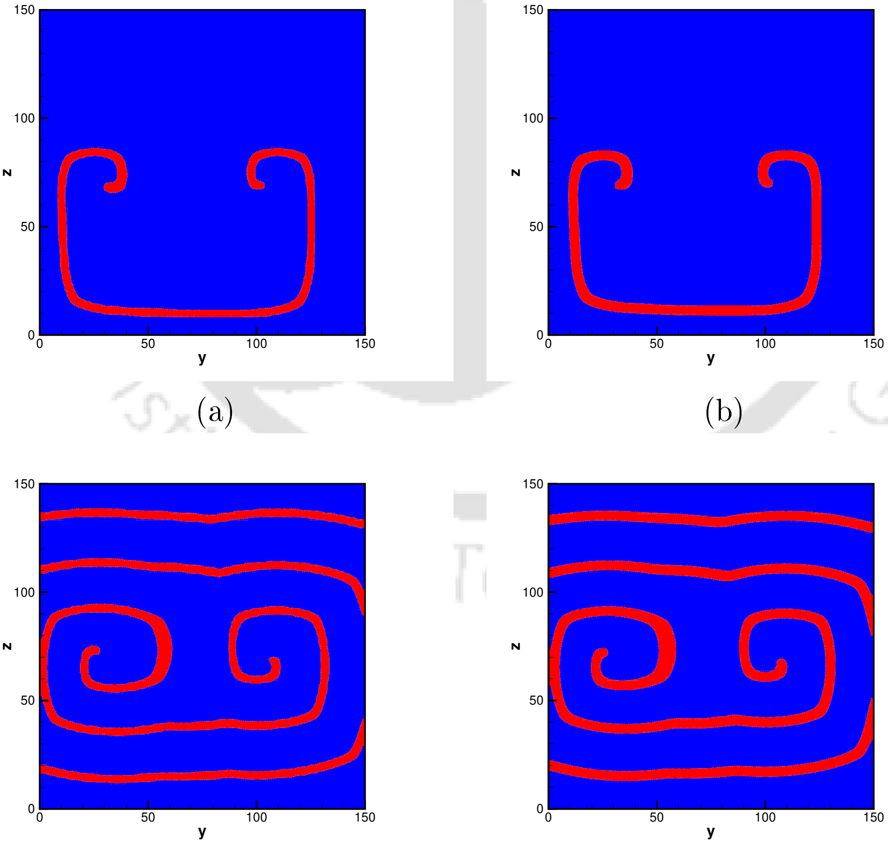

(a) (b)

(c) (d)

Figure 6.3: The concentrations of $u = 0.5$ and $v = 0.5$ in y-z plane keeping $x = 75$ at different times: (a)-(b) $t = 10.0$ and (c)-(d) $t = 30.0$. Left panel for u and right panel v.

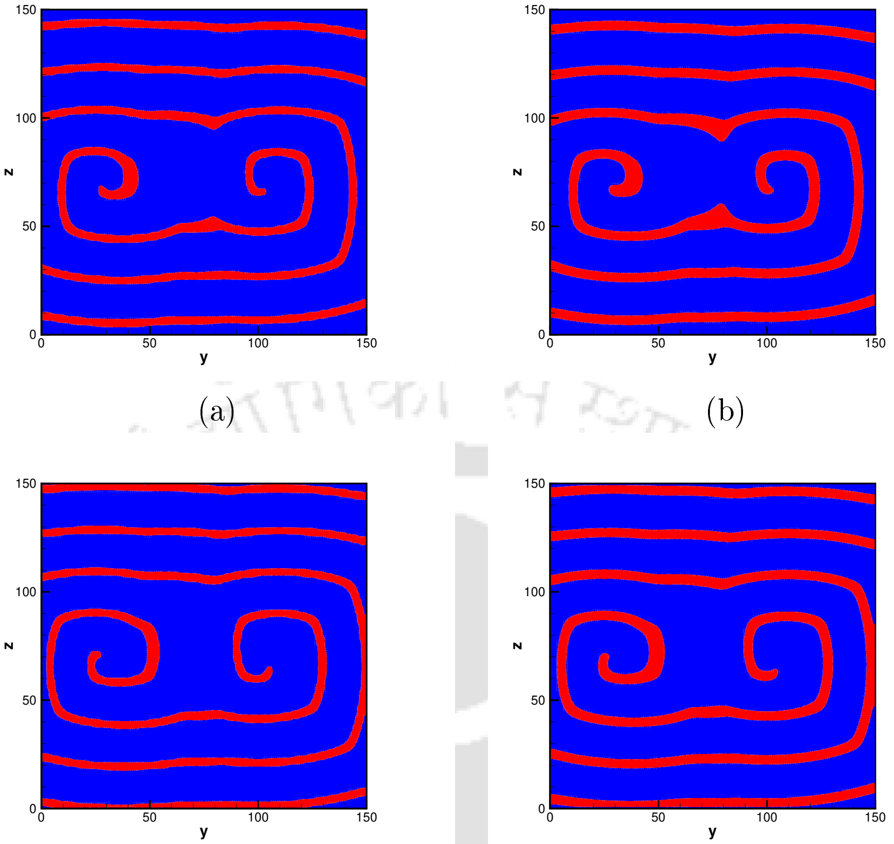

(a) (b)

(c) (d)

Figure 6.4: The concentrations of $u = 0.5$ and $v = 0.5$ in y-z plane keeping $x = 75$ at different times: (a)-(b) $t = 50.0$ and (c)-(d) $t = 60.0$. Left panel for u and right panel v.

6.3.3 Test problem 3

Now, we explore the numerical solution of unsteady convection-diffusion equation by converting it to R-D equation exploiting developed HOC scheme (6.15). Consider the convection-diffusion equation,

$$\frac{\partial u}{\partial t} + a_x\frac{\partial u}{\partial x} + a_y\frac{\partial u}{\partial y} + a_z\frac{\partial u}{\partial z} = D\left(\frac{\partial^2 u}{\partial x^2} + \frac{\partial^2 u}{\partial y^2} + \frac{\partial^2 u}{\partial z^2}\right) + f_3(x, y, z, t), \tag{6.33}$$

where D is the diffusion coefficient, and a_x, a_y and a_z are the convection coefficients and the function f_3 is given by,

$$\begin{aligned} f_3(x, y, z, t) = \exp(2t)((e + 3\pi^2)sin(\pi x)sin(\pi y)sin(\pi z) + a_x\pi cos(\pi x)sin(\pi y)sin(\pi z) \\ + a_y\pi sin(\pi x)cos(\pi y)sin(\pi z) + a_z\pi sin(\pi x)sin(\pi y)cos(\pi z)). \end{aligned} \tag{6.34}$$

Indian Institute of Technology Guwahati

The initial condition is given by

$$u(x, y, z) = sin(\pi x)sin(\pi y)sin(\pi z). \tag{6.35}$$

The analytical solution is given by,

$$u(x, y, z, t) = exp(2t)sin(\pi x)sin(\pi y)sin(\pi z). \tag{6.36}$$

Now, we solve the above equation (6.33), by converting it in the form of R-D equation (6.3).

$$\frac{\partial u}{\partial t} = D\left(\frac{\partial^2 u}{\partial x^2} + \frac{\partial^2 u}{\partial y^2} + \frac{\partial^2 u}{\partial z^2}\right) + f_4(u, v), \tag{6.37}$$

where $f_4 = a_x\frac{\partial u}{\partial x} + a_y\frac{\partial u}{\partial y} + a_z\frac{\partial u}{\partial z} + f_3(x, y, z, t)$.

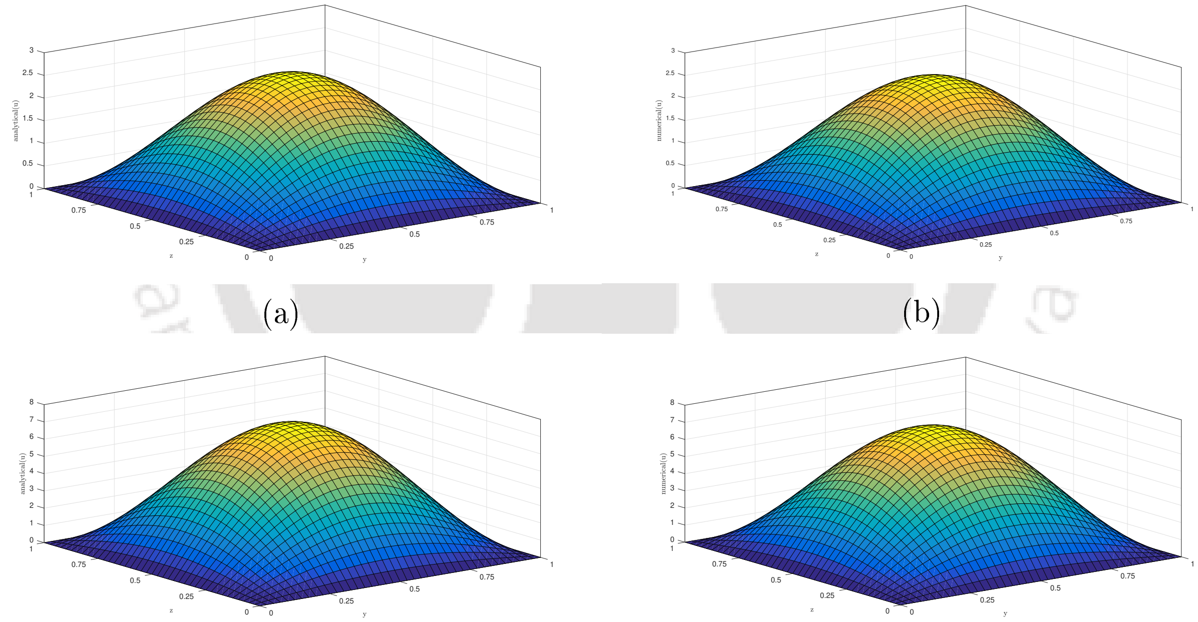

(a) (b)

(c) (d)

Figure 6.5: Comparison between analytical (left panel) and numerical (right panel) solutions at fixed $x = 0.5$ for grid of size $21 \times 21 \times 21$ at different times: (a)-(b) $t = 0.5$ and (c)-(d) $t = 1.0$,

As in the first test case, the problem domain is again a cube of size $[0, 1] \times [0, 1] \times [0, 1]$. The parameter values considered here are: $D = 1.0$, $e = 2$, $a_x = 2.35$, $a_y = 5.65$ and $a_z = 3.25$. In figure 6.5, we present the numerical solution obtained through our

TH-2268_136123014

computation on a grid of size $21 \times 21 \times 21$ with a time step $\Delta t = 0.0005$ along the plane $x = 0.5$ along with the corresponding analytical solutions at times $t = 0.5$ and 1.0. It is heartening to note that on a grid as coarse as $21 \times 21 \times 21$, one can hardly differentiate between the numerical and the analytical solutions. Further, in table 6.1, we compare the numerical values obtained from the developed HOC scheme with the analytical ones at the center point of the cube on different grid sizes at different time stations. This table again reconfirms the closeness of our computed solutions to the analytical ones even on coarser grids and gradual decreasee in the error as grid is refined.

Table 6.1: Comparison of the numerical solution on different grids at the center point of the cube.

Time	$11 \times 11 \times 11$	$21 \times 21 \times 21$	$41 \times 41 \times 41$	$81 \times 81 \times 81$	**Exact**
0.1	1.224667	1.222190	1.221529	1.221361	1.221403
0.5	2.725736	2.720079	2.718571	2.718188	2.718282
1.0	7.409318	7.393941	7.389842	7.388801	7.389056
5.0	22086.865911	22041.027355	22028.808110	22025.705735	22026.467595

6.4 Conclusions

In the present chapter, we have developed an implicit high order compact finite difference scheme to discretize the 3D unsteady R-D equations. The proposed scheme is unconditionally stable, spatially fourth and temporally second order accurate. This scheme is particularly derived to solve the mathematical models arising out the problems in pattern formation. Although the scheme is based on 3D unsteady R-D equations, it was seen to resolve the solution of unsteady convection-diffusion equations as well as simulate 3D scroll waves from the Barkley model at equal ease. For the last test case where an analytical solution is available, our numerical results on coarse grids were found to be extremely close to the analytical ones.

Indian Institute of Technology Guwahati

Chapter 7

CONCLUSION

This dissertation is mainly concerned with the simulation of two-dimensional (2D) spiral waves in excitable media through the application of High Order Compact (HOC) schemes. A recently developed HOC scheme has been reconstructed to discretize the reaction-diffusion equations governing the spiral waves. It further explores the possibility of simulating three-dimensional (3D) scroll waves in excitable media through the application of HOC schemes by proposing an HOC scheme for discretizing the 3D reaction-diffusion equations. In the following, we highlight its major achievements and also provide some hints for possible future works that can be undertaken based on the current work.

7.1 Highlights

1. An existing unconditionally stable, $O(h^4, (\Delta t)^2)$ implicit HOC scheme for the two dimensional convection-diffusion equations has been reconstructed to suit the discretization of some very well-known models of pattern formation in excitable media, notable amongst them are the Barkley and the FHN models. In the process it was able to remove the debilitating effects of the lower order accurate schemes in vogue for simulating spiral waves in excitable media in accurately capturing the underlying physical phenomena.

2. As described above, lower order accurate schemes, notably Euler's explicit scheme that has been used quite extensively for simulating pattern formation in excitable media lacked the power of HOC schemes to accurately resolve the physiological

TH-2268_136123014

processes. The discrepancies of explicit scheme results with experimental ones have been explained through the concept of implicit reaction, dispersion and diffusion by carrying out a thorough analysis of the corresponding modified differential equation.

3. The efficiency of the reconstructed HOC scheme has been established through the highly accurate and efficient coarse grid computation of spiral waves in excitable media in the most complicated cases. We have also established grid independence and the order of accuracy of simulated data from HOC scheme and the error was seen to decay with a rate of convergence around 3.5. The simulations of spiral waves from our numerical computations are found to be extremely close to ones found in the existing literature. We have further compared our simulated spiral wave patterns and spiral tip path with the ones obtained from Euler‘s explicit scheme and our results were found to be more closer to the experimental and the available benchmark results. Besides, we have demonstrated that our computed spiral tip path with different time steps for the same parameters follow the same path and as such is time grid-independent.

4. We have explored the effect of zero-flux and periodic boundary conditions on the spiral wave patterns resulting from the Barkley and FitzHugh-Nagumo models in excitable media. In the process, we have also derived fourth order accurate approximations to the periodic boundary conditions which has the potential to be employed in the other fields of computational physics as well. We found that the role of periodic conditions is to inflict spiral wave break-up against the regular spiral wave patterns seen with the zero flux boundary conditions.

5. Almost all the previous numerical studies on the spiral wave dynamics have been obtained by exploiting the state variables u and v. In the current study, for the first time, a comprehensive spectral density analysis of the spiral tip path has been performed to explore the effect of parameters in changing the dynamics of spiral wave. Further, we have also study the effect of an obstacle to the periodic rotating

spiral waves and demonstrated how it affects the dynamics of spiral wave. The obstacle was seen to change the trajectory of spiral tip which eventually settled into periodic motion. Moreover, we have also performed the linear stability analysis of rotating spiral wave solutions and found that both the periodic and the non-periodic rotating waves solutions are stable ones.

6. Again, we have used an already existing unconditionally stable, $O(h^4, (\Delta t)^2)$ implicit HOC scheme to simulate the spiral wave patterns from the Oregonator model. Then in order to examine the efficiency of HOC scheme for the Oregonator model, we have established the grid independence and the rate of convergence of the computed data. Further we have studied the effect of straining on the stable rotating spiral wave, which was seen to generate a host of complex patterns in different regimes. Our study reveals that these regimes can be broadly divided into three categories: no break-up, transitional and break-up regimes. Our projected regimes are different from the earlier ones found in literature where the computations were performed for very small time range and with lower order accurate schemes. In the process, we have also investigated the effect of reaction parameter on the spiral wave dynamics in the absence of any straining. Moreover, both the periodic and the meandering rotating spiral wave solutions resulting from the simulations of Oregonator model were also seen to be stable ones.

7. We have developed an unconditionally stable HOC scheme to discretize the 3D unsteady R-D equations. This scheme is implicit in nature, fourth order accurate in all space coordinates and second order accurate in time. This scheme is particularly derived to solve the mathematical models arising out the problems in pattern formation. Although the scheme is derived for unsteady R-D equations, it was also seen to tackle the unsteady convection-diffusion equations with equal ease. In order to probe the efficiency of developed scheme, we have also presented three numerical examples and found that our simulations are extremely close to the results of

Indian Institute of Technology Guwahati

existing literature. One of these examples is concerned with Barkley model in three-dimensions and as such the proposed scheme could go a long way in simulating scroll waves in excitable media.

7.2 Scope for Future Work

The work described in this dissertation could open up a host of possibilities, the major ones of which are listed below.

1. As has been mentioned in the previous chapters, many of the patterns observed in the evolution of spiral and scroll waves are also observed in the human heart. For example, the transition from a stable to a meandering or drifting spiral tip and then to spiral wave breakup is very similar to the transition from a stable to polymorphic electric arrhythmias and then to fibrillation and sudden cardiac death. Likewise, the transition of spiral waves from outward rotating to inward rotating is observed experimentally in glycolytic activity as a result of increasing the protein concentration of the extract. In general, such transitions are expected to occur close to a Hopf bifurcation. Thus, a bifurcation study based on the computed data seems to be an interesting and important area of research which can be undertaken in the near future.

2. In laboratory experiments, interaction between waves and dissipative structures in B-Z reaction was seen to result in not only chaos and but also the break up of excitation waves due to the strong convective motions. Interestingly similar chaotic phenomenon is also observed in heart fibrillation owing to the cells in heart muscles not being exactly identical. Thus it becomes imperative to control the meandering as well as drifting spiral waves resulting from the straining effect on stable rotating spiral waves. One such way of doing so is placing an obstacle in the problem domain so that the spiral waves start performing periodic rotation after being pinned to the obstacle. While the effect of convective motions could be mathematically modelled

by adding advection terms to the system of R-D equations as in chapter 5, pinning an obstacle is very similar to the studies performed in chapter 4. Thus there is a strong scope for the studies carried out chapters 4 and 5 to be extended further to simulate the physiological process resulting from such situations and it could be another area of research worth pursuing. A glimpse of our preliminary investigation on this can be found in the appendix A.

3. Over the past two decades, the study of scroll waves has made tremendous strides amongst the scientific community. The scheme proposed in chapter 6 can go a long way in efficiently simulating scroll waves in excitable media which is fraught with many interesting possibilities.

Indian Institute of Technology Guwahati

भारतीय प्रौद्योगिकी संस्थान गुवाहाटी • Indian Institute of Technology Guwahati •

Appendix A

STRAIN EFFECT ON A PINNED SPIRAL

Having seen the effect of strain on the dynamics of spiral waves in excitable media, it will be interesting to see how the dynamics changes once a spiral wave is pinned. However such a study is beyond the scope of the current study and as such we provide a glimpse of the effect of advection-induced spiral drift on the stability of pinned spiral for the benefit of the readers by choosing the value $\gamma = 0.01$ in the no break-up regime.

We accomplish the pinning of the obstacle to the spiral in the following way. A circular obstacle, that is a group of discrete points (x, y) such that $\sqrt{(x - x_0)^2 + (y - y_0)^2} \leq \frac{d}{2}$, where d is the diameter and (x_0, y_0) is the center of the spiral core [67], is placed on the problem domain and pinning is obtained by setting $u = v = 0$ thereat [22, 49]. This core is obtained by allowing the spiral wave to propagate freely [67] without the strain effect ($\gamma = 0.0$) for several rotations and eventually settle down into a periodic orbit. Note that the core is nothing but the periodically settled circular orbit [101]. In the current study, the core is the circle in figure 5.10(b) corresponding to $\gamma = 0.0$ with $(x_0, y_0) = (-0.2000, -0.0036)$ and $d = 0.46$. Once the obstacle is placed, the spiral wave is allowed to evolve by setting $\gamma = 0.01$. We also investigate the evolution of the spiral wave when there is no strain effect ($\gamma = 0.0$). The simulations are once again carried out on a grid of size 241×241 with no-flux boundary conditions.

We present our findings in figures A.1(a)-(b) and A.2(a)-(b), where simulations were performed up to time $t = 1500.00$ after pinning. Figure A.1(a) displays the periodically settled spiral wave without the strain effect along with the circular obstacle placed at the center of the core. In figure A.1(b), the spiral tip trajectory is shown along with the spiral wave at time $t = 100.0$. One can clearly see that the tip revolves around the obstacle initially; at around $t = 1.38$, after making one complete revolution it starts gradually drifting away from the obstacle and follow the trajectory as shown in figures A.1(b) and A.2(a)-(b). Due to the strain effect (figures A.2(a)-(b)), it then starts moving upwards

TH-2268_136123014

in the direction of the top left corner and settles into a periodic circular orbit at around $t = 800.00$ centered at $(-5.2, 4.0)$ and diameter 0.46. Interestingly, without the obstacle in place, although the tip follows a different trajectory, it eventually settles into exactly the same circular orbit as in the case with the obstacle, though with a much slower pace. The overlapping of the circular orbits shown in the inset of figure A.2(a) exemplifies this fact.

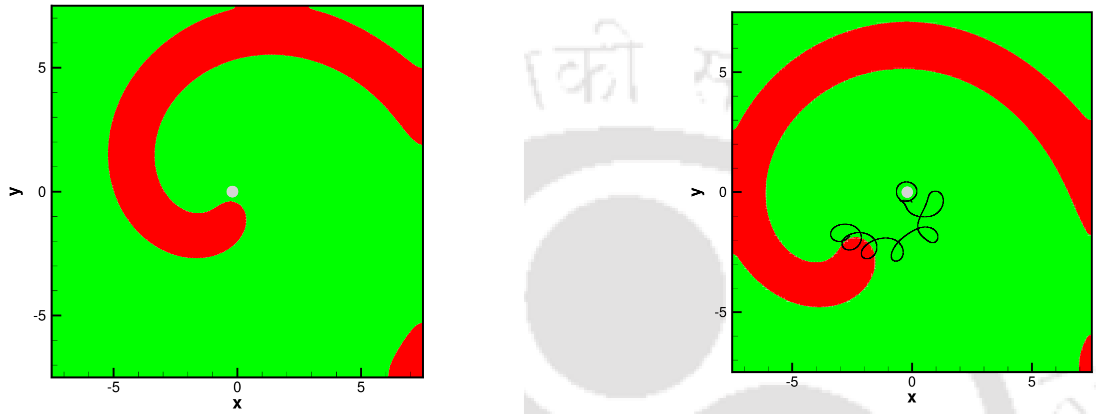

(a)

(b)

Figure A.1: (a) The spiral wave along with the circular obstacle at the core and (b) The spiral wave at time $t = 100$ along with the tip trajectory in the presence of the obstacle.

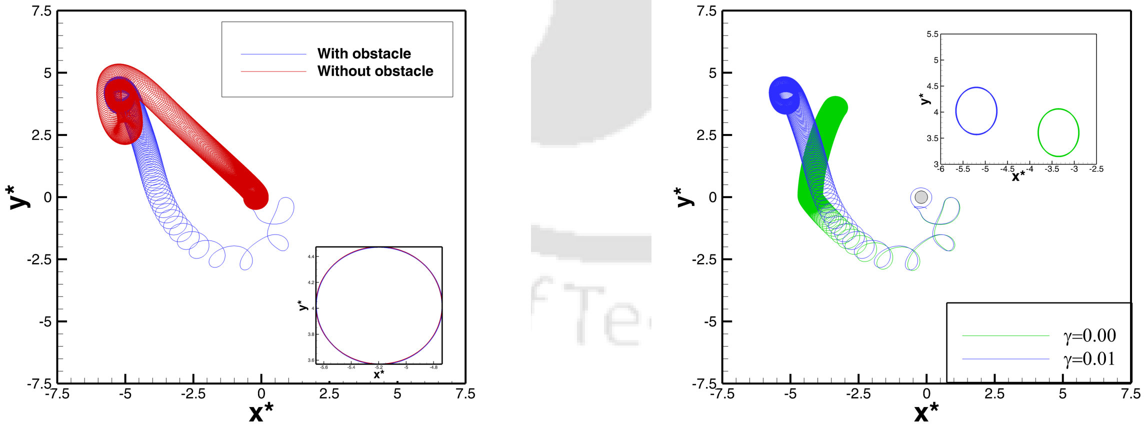

(a)

(b)

Figure A.2: (a) The tip trajectories with and without the circular obstacle in the presence of strain effect, the final cores at the inset and (b) The tip trajectories with and without the strain effect in presence of the circular obstacle, the final cores at the inset.

Next, we examine how the spiral wave behaves in presence of the obstacle without the strain effect. In figure A.2(b), we present the trajectories of the tips corresponding to $\gamma = 0.0$ and 0.01. One can clearly see that initially both the tips follow the same trajectory and begin to deviate from each other at around $t = 120.0$. Eventually the tip without the strain effect also settles into a periodic circular orbit, but at a different location as can be seen from the inset of figure A.2(b). Remarkably, in all the three cases discussed in figures A.2(a)-(b), the size of the core is exactly the same as the core inside which the obstacle was initially placed.

Currently, we are investigating the effect of straining on dynamics of a pinned spiral wave in all the three regimes described in chapter 5. The results from this comprehensive study will be detailed in the near future.

Bibliography

[1] S. Abarbanel and A. Kumar. Compact High-Order Schemes for the Euler Equations. Technical Report 1, 1988.

[2] K. Agladze and P. De Kepper. Influence of electric field on rotating spiral waves in the Belousov-Zhabotinskii reaction. *The Journal of Physical Chemistry*, 96(13):5239–5242, 1992.

[3] K. Agladze, V. Krinsky, and A. Pertsov. Chaos in the non-stirred Belousov-Zhabotinsky reaction is induced by interaction of waves and stationary dissipative structures. *Nature*, 308(5962):834–835, 1984.

[4] S. Alonso, F. Sagues, and A. S. Mikhailov. Negative-tension instability of scroll waves and Winfree turbulence in the Oregonator model. *The Journal of Physical Chemistry A*, 110(43):12063–12071, 2006.

[5] F. Amdjadi. A numerical method for the dynamics and stability of spiral waves. *Applied Mathematics and Computation*, 217(7):3385–3391, 2010.

[6] J. D. Anderson and J. Wendt. *Computational Fluid Dynamics*, volume 206. Springer, 1995.

[7] M. Bär and L. Brusch. Breakup of spiral waves caused by radial dynamics: Eckhaus and finite wavenumber instabilities. *New Journal of Physics*, 6(1):5, 2004.

[8] D. Barkley. Euclidean symmetry and the dynamics of rotating spiral waves. *Physical Review Letters*, 72(1):164, 1994.

[9] D. Barkley, M. Kness, and L. S. Tuckerman. Spiral-wave dynamics in a simple model of excitable media: The transition from simple to compound rotation. *Physical Review A*, 42(4):2489, 1990.

[10] A. L. Belmonte, Q. Ouyang, and J.-M. Flesselles. Experimental survey of spiral dynamics in the Belousov-Zhabotinsky reaction. *Journal de Physique II*, 7(10):1425–1468, 1997.

TH-2268_136123014

[11] B. Belousov. Sbornik Referatov po Radiacioni Medicine. In *1958 Meeting*, volume 145, 1959.

[12] B. P. Belousov. A periodic reaction and its mechanism. *Oscillation and Travelling Waves in Chemical Systems*, 1951.

[13] V. Biktashev, D. Barkley, and I. Biktasheva. Orbital motion of spiral waves in excitable media. *Physical Review Letters*, 104(5):058302, 2010.

[14] V. Biktashev, I. Biktasheva, A. Holden, M. Tsyganov, J. Brindley, and N. Hill. Effects of shear flows on nonlinear waves in excitable media. *Journal of Biological Physics*, 25(2-3):101–113, 1999.

[15] V. Biktashev, I. Biktasheva, A. Holden, M. Tsyganov, J. Brindley, and N. Hill. Spatiotemporal irregularity in an excitable medium with shear flow. *Physical Review E*, 60(2):1897, 1999.

[16] V. Biktashev, A. Holden, M. Tsyganov, J. Brindley, and N. Hill. Excitation wave breaking in excitable media with linear shear flow. *Physical Review Letters*, 81(13):2815, 1998.

[17] D. Bin-Wen, Z. Guo-Yong, and C. Yong. Dynamics of spiral wave tip in excitable media with gradient parameter. *Communications in Theoretical Physics*, 52(1):173, 2009.

[18] E. Boccia, S. Luther, and U. Parlitz. Modelling far field pacing for terminating spiral waves pinned to ischaemic heterogeneities in cardiac tissue. *Philosophical Transactions of the Royal Society A: Mathematical, Physical and Engineering Sciences*, 375(2096):20160289, 2017.

[19] A. Bozorgmanesh, M. Otadi, K. A. SAFE, F. Zabihi, and A. M. Barkhordari. Lagrange two-dimensional interpolation method for modeling nanoparticle formation during RESS process. 2009.

[20] R. L. Burden and J. Faires. *Numerical Analysis*. Cengage Learning, 2011.

[21] A. J. Christlieb, Y. Liu, and Z. Xu. High order operator splitting methods based on an integral deferred correction framework. *Journal of Computational Physics*, 294:224–242, 2015.

[22] N. P. Das, D. Mahanta, and S. Dutta. Unpinning of scroll waves under the influence of a thermal gradient. *Physical Review E*, 90(2):022916, 2014.

[23] M. Dehghan. Numerical solution of the three-dimensional advection-diffusion equation. *Applied Mathematics and Computation*, 150(1):5–19, 2004.

[24] M. Dehghan and M. Abbaszadeh. Variational multiscale element free Galerkin (VMEFG) and local discontinuous Galerkin (LDG) methods for solving two-dimensional Brusselator reaction–diffusion system with and without cross-diffusion. *Computer Methods in Applied Mechanics and Engineering*, 300:770–797, 2016.

[25] M. Dehghan, M. Abbaszadeh, and A. Mohebbi. The use of element free Galerkin method based on moving Kriging and radial point interpolation techniques for solving some types of Turing models. *Engineering Analysis with Boundary Elements*, 62:93–111, 2016.

[26] S. Dennis and J. Hudson. Compact h^4 finite-difference approximations to operators of Navier-Stokes type. *Journal of Computational Physics*, 85(2):390–416, 1989.

[27] Devanand and J. C. Kalita. HOC simulation of Barkley model in excitable media. In *AIP Conference Proceedings*, volume 1975, page 030011. AIP Publishing, 2018.

[28] S. Dutta and O. Steinbock. Spiral defect drift in the wave fields of multiple excitation patterns. *Physical Review E*, 83(5):056213, 2011.

[29] X. Feng, X. Gao, D.-B. Pan, B.-W. Li, and H. Zhang. Unpinning of rotating spiral waves in cardiac tissues by circularly polarized electric fields. *Scientific reports*, 4:4831, 2014.

[30] F. H. Fenton, E. M. Cherry, H. M. Hastings, and S. J. Evans. Multiple mechanisms of spiral wave breakup in a model of cardiac electrical activity. *Chaos: An Interdisciplinary Journal of Nonlinear Science*, 12(3):852–892, 2002.

[31] R. J. Field, E. Koros, and R. M. Noyes. Oscillations in chemical systems. II. Thorough analysis of temporal oscillation in the bromate-cerium-malonic acid system. *Journal of the American Chemical Society*, 94(25):8649–8664, 1972.

[32] R. J. Field and R. M. Noyes. Oscillations in chemical systems. IV. Limit cycle behavior in a model of a real chemical reaction. *The Journal of Chemical Physics*, 60(5):1877–1884, 1974.

[33] R. J. Field and A. T. Winfree. Travelling waves of chemical activity in the Zaikin-Zhabotinskii-Winfree reagent. *Journal of Chemical Education*, 56(11):754, 1979.

[34] R. FitzHugh. Impulses and physiological states in theoretical models of nerve membrane. *Biophysical Journal*, 1(6):445–466, 1961.

[35] A. J. Foulkes. Drift and meander of spiral waves. *arXiv preprint arXiv:0912.4247*, 2009.

[36] Y. Ge, Z. F. Tian, and J. Zhang. An exponential high-order compact ADI method for 3D unsteady convection–diffusion problems. *Numerical Methods for Partial Differential Equations*, 29(1):186–205, 2013.

[37] Y. Ge, F. Zhao, and J. Wei. A high order compact ADI method for solving 3D unsteady convection diffusion problems. *Applied and Computational Mathematics*, 7(1):1–10, 2018.

[38] C. Gray. An analysis of the Belousov-Zhabotinskii reaction. *Rose-Hulman Undergraduate Mathematics Journal*, 3(1):1, 2002.

[39] R. A. Gray, J. Jalife, A. Panfilov, W. T. Baxter, C. Cabo, J. M. Davidenko, and A. M. Pertsov. Nonstationary vortexlike reentrant activity as a mechanism of polymorphic ventricular tachycardia in the isolated rabbit heart. *Circulation*, 91(9):2454–2469, 1995.

[40] R. A. Gray, J. P. Wikswo, and N. F. Otani. Origin choice and petal loss in the flower garden of spiral wave tip trajectories. *Chaos: An Interdisciplinary Journal of Nonlinear Science*, 19(3):033118, 2009.

[41] P. Grindrod. *The theory and applications of reaction-diffusion equations: patterns and waves.* Clarendon Press, 1996.

[42] M. M. Gupta, R. P. Manohar, and J. W. Stephenson. A single cell high order scheme for the convection-diffusion equation with variable coefficients. *International Journal for Numerical Methods in Fluids*, 4(7):641–651, 1984.

[43] A. L. Hodgkin and A. F. Huxley. A quantitative description of membrane current and its application to conduction and excitation in nerve. *The Journal of Physiology*, 117(4):500–544, 1952.

[44] J. D. Hoffman and S. Frankel. *Numerical methods for engineers and scientists.* CRC press, 2018.

[45] W. Jahnke, W. Skaggs, and A. T. Winfree. Chemical vortex dynamics in the Belousov-Zhabotinskii reaction and in the two-variable Oregonator model. *The Journal of Physical Chemistry*, 93(2):740–749, 1989.

[46] W. Jahnke and A. T. Winfree. A survey of spiral-wave behaviors in the Oregonator model. *International Journal of Bifurcation and Chaos*, 1(02):445–466, 1991.

[47] D. Jaiswal and J. C. Kalita. HOC approximation of periodic boundary conditions in excitable media. *Under Review.*

[48] D. Jaiswal and J. C. Kalita. Effect of straining on spiral wave dynamics in excitable media. *Physica D: Nonlinear Phenomena*, 409:132483, 2020.

[49] D. Jaiswal and J. C. Kalita. Novel high-order compact approach for dynamics of spiral waves in excitable media. *Applied Mathematical Modelling*, 77:341–359, 2020.

[50] J. C. Kalita. *HOC Schemes for Incompressible Viscous Flows: Application and Development.* PhD thesis, 2001.

[51] J. C. Kalita. Effect of boundary location on the steady flow past an impulsively started circular cylinder. *International Journal of Computing Science and Mathematics*, 5(3):252–279, 2014.

[52] J. C. Kalita. A super-compact higher order scheme for the unsteady 3D incompressible viscous flows. *Computational and Applied Mathematics*, 33(3):717–738, 2014.

[53] J. C. Kalita. A Dual-Purpose High Order Compact Approach for Pattern Formation Using Gray-Scott Model. *International Journal of Applied and Computational Mathematics*, 3(3):2747–2760, 2017.

[54] J. C. Kalita, D. C. Dalal, and A. K. Dass. Fully compact higher-order computation of steady-state natural convection in a square cavity. *Physical Review E*, 64(6):066703, 2001.

[55] J. C. Kalita and B. B. Gogoi. Global two-dimensional stability of the staggered cavity flow with an HOC approach. *Computers & Mathematics with Applications*, 67(3):569–590, 2014.

[56] J. C. Kalita and B. B. Gogoi. A biharmonic approach for the global stability analysis of 2d incompressible viscous flows. *Applied Mathematical Modelling*, 40(15-16):6831–6849, 2016.

[57] J. C. Kalita and R. K. Ray. A transformation-free HOC scheme for incompressible viscous flows past an impulsively started circular cylinder. *Journal of Computational Physics*, 228(14):5207–5236, 2009.

[58] A. Karma. Spiral breakup in model equations of action potential propagation in cardiac tissue. *Physical Review Letters*, 71(7):1103, 1993.

[59] C. T. Kelley. *Iterative methods for linear and nonlinear equations.* SIAM Publications, 1995.

[60] Y.-H. Kim, F. Xie, M. Yashima, T.-J. Wu, M. Valderrábano, M.-H. Lee, T. Ohara, O. Voroshilovsky, R. N. Doshi, M. C. Fishbein, et al. Role of papillary muscle in the generation and maintenance of reentry during ventricular tachycardia and fibrillation in isolated swine right ventricle. *Circulation*, 100(13):1450–1459, 1999.

[61] P. Kumar and J. C. Kalita. A transformation-free ψ-v formulation of the Navier-Stokes equations on compact nonuniform grids. *Journal of Computational and Applied Mathematics*, 353:292–317, 2019.

[62] K. J. Lee, E. C. Cox, and R. E. Goldstein. Competing patterns of signaling activity in Dictyostelium discoideum. *Physical Review Letters*, 76(7):1174, 1996.

[63] J. Li and J. Li. High-order compact difference methods for simulating wave propagations in excitable media. *International Journal of Numerical Analysis and Modeling, Series B*, 5(4):339–346, 2014.

[64] T.-C. Li, X. Gao, F.-F. Zheng, D.-B. Pan, B. Zheng, and H. Zhang. A theory for spiral wave drift induced by ac and polarized electric fields in chemical excitable media. *Scientific Reports*, 7(1):1–9, 2017.

[65] T.-C. Li, D.-B. Pan, K. Zhou, R. Jiang, C. Jiang, B. Zheng, and H. Zhang. Jacobian-determinant method of identifying phase singularity during reentry. *Physical Review E*, 98(6):062405, 2018.

[66] W. Liao. A high-order ADI finite difference scheme for a 3D reaction-diffusion equation with Neumann boundary condition. *Numerical Methods for Partial Differential Equations*, 29(3):778–798, 2013.

[67] J. Luengviriya, M. Sutthiopad, M. Phantu, P. Porjai, J. Kanchanawarin, S. C. Müller, and C. Luengviriya. Influence of excitability on unpinning and termination of spiral waves. *Physical Review E*, 90(5):052919, 2014.

[68] R. MacKinnon and G. Carey. Analysis of material interface discontinuities and superconvergent fluxes in finite difference theory. *Journal of Computational Physics*, 3(3):275–288, 1988.

[69] R. J. MacKinnon and R. W. Johnson. Differential-equation-based representation of truncation errors for accurate numerical simulation. *International Journal for Numerical Methods in Fluids*, 13(6):739–757, 1991.

[70] D. Mahanta and S. Dutta. Unpinning of scroll waves attached to multiple heterogeneities. *Physical Review E*, 98(5):052206, 2018.

[71] R. Majumder, A. R. Nayak, and R. Pandit. Scroll-wave dynamics in human cardiac tissue: lessons from a mathematical model with inhomogeneities and fiber architecture. *PLOS One*, 6(4), 2011.

[72] P. F. Mancera. A study of a numerical solution of the steady two dimensional Navier-Stokes equations in a constricted channel problem by a compact fourth order method. *Applied Mathematics and Computation*, 146(2-3):771–790, 2003.

[73] R.-M. Mantel and D. Barkley. Parametric forcing of scroll-wave patterns in three-dimensional excitable media. *Physica D: Nonlinear Phenomena*, 149(1-2):107–122, 2001.

[74] H. Mittal, J. C. Kalita, and Q. M. Al-Mdallal. A hybrid ψ-v HOC approach for surface tension driven flows in level set framework. *Computers & Mathematics with Applications*, 2019.

[75] A. Munuzuri, V. Davydov, V. Pérez-Muñuzuri, M. Gómez-Gesteira, and V. Pérez-Villar. General properties of the electric-field-induced vortex drift in excitable media. *Chaos, Solitons & Fractals*, 7(4):585–595, 1996.

[76] E. Nakouzi, J. F. Totz, Z. Zhang, O. Steinbock, and H. Engel. Hysteresis and drift of spiral waves near heterogeneities: from chemical experiments to cardiac simulations. *Physical Review E*, 93(2):022203, 2016.

[77] A. R. Nayak and R. Pandit. Spiral-wave dynamics in ionically realistic mathematical models for human ventricular tissue: the effects of periodic deformation. *Frontiers in Physiology*, 5:207, 2014.

[78] D. Olmos. Reflection and attachment of spirals at obstacles for the Fitzhugh-Nagumo and Beeler-Reuter models. *Physical Review E*, 81(4):041924, 2010.

[79] D. Olmos-Liceaga, D. L. Soto, and R. Ávila-Pozos. Breaking of Spiral Waves Due to Obstacles. *Journal of Advances in Mathematics and Computer Science*, pages 1–14, 2017.

[80] N. F. Otani, K. Wheeler, V. Krinsky, and S. Luther. Termination of scroll waves by surface impacts. *Physical Review Letters*, 123(6):068102, 2019.

[81] S. K. Pandit, J. C. Kalita, and D. C. Dalal. A transient higher order compact scheme for incompressible viscous flows on geometries beyond rectangular. *Journal of Computational Physics*, 225(1):1100–1124, 2007.

[82] S. K. Pandit, J. C. Kalita, and D. C. Dalal. A fourth-order accurate compact scheme for the solution of steady Navier-Stokes equations on non-uniform grids. *Computers & Fluids*, 37(2):121–134, 2008.

[83] A. V. Panfilov and J. P. Keener. Effects of high frequency stimulation on cardiac tissue with an inexcitable obstacle. *Journal of theoretical biology*, 163(4):439–448, 1993.

[84] A. Pechenkin. On the origin of the Belousov-Zhabotinsky reaction. *Biological Theory*, 4(2):196–206, 2009.

[85] A. Pertsov and M. Vinson. Dynamics of scroll waves in inhomogeneous excitable media. *Philosophical Transactions of the Royal Society of London. Series A: Physical and Engineering Sciences*, 347(1685):687–701, 1994.

[86] A. M. Pertsov, J. M. Davidenko, R. Salomonsz, W. T. Baxter, and J. Jalife. Spiral waves of excitation underlie reentrant activity in isolated cardiac muscle. *Circulation Research*, 72(3):631–650, 1993.

[87] M. Phantu, N. Kumchaiseemak, P. Porjai, M. Sutthiopad, S. C. Müller, C. Luengviriya, and J. Luengviriya. Generation of spiral waves pinned to obstacles in a simulated excitable system. In *Journal of Physics: Conference Series*, volume 901, page 012021. IOP Publishing, 2017.

[88] R. H. Pletcher, J. C. Tannehill, and D. Anderson. *Computational Fluid Mechanics and Heat Transfer*. CRC press, 2012.

[89] P. Porjai, M. Sutthiopad, K. Khaothong, M. Phantu, N. Kumchaiseemak, J. Luengviriya, K. Showalter, and C. Luengviriya. Twisted scroll wave dynamics: partially pinned waves in excitable chemical media. *Physical Chemistry Chemical Physics*, 21(5):2419–2425, 2019.

[90] S. Punacha, S. Berg, A. Sebastian, V. I. Krinski, S. Luther, and T. Shajahan. Spiral wave unpinning facilitated by wave emitting sites in cardiac monolayers. *Proceedings of the Royal Society A*, 475(2230):20190420, 2019.

[91] C. Qiao, Y. Wu, X. Lu, C. Wang, Q. Ouyang, and H. Wang. Control of scroll wave turbulence in a three-dimensional reaction-diffusion system with gradient. *Chaos: An Interdisciplinary Journal of Nonlinear Science*, 18(2):026109, 2008.

[92] J. Qin. The new alternating direction implicit difference methods for solving three-dimensional parabolic equations. *Applied Mathematical Modelling*, 34(4):890–897, 2010.

[93] Z. Qu, F. Xie, A. Garfinkel, and J. N. Weiss. Origins of spiral wave meander and breakup in a two-dimensional cardiac tissue model. *Annals of Biomedical Engineering*, 28(7):755–771, 2000.

[94] J. Ramos. Pattern formation in two-dimensional reactive-diffusive media with straining. *Chemical Physics Letters*, 365(3-4):260–266, 2002.

[95] J. I. Ramos. Spiral wave break-up and planar front formation in two-dimensional reactive-diffusive media with straining. *Applied Mathematics and Computation*, 154(3):697–711, 2004.

[96] R. K. Ray and J. C. Kalita. Higher-order-compact simulation of unsteady flow past a rotating cylinder at moderate Reynolds numbers. *Computational and Applied Mathematics*, 35(1):219–250, 2016.

[97] S. Sen and J. C. Kalita. A 4OEC scheme for the biharmonic steady Navier-Stokes equations in non-rectangular domains. *Computer Physics Communications*, 196:113–133, 2015.

[98] S. Sen, J. C. Kalita, and M. M. Gupta. A robust implicit compact scheme for two-dimensional unsteady flows with a biharmonic stream function formulation. *Computers & Fluids*, 84:141–163, 2013.

[99] T. Shajahan, S. Sinha, and R. Pandit. Spiral-wave dynamics depend sensitively on inhomogeneities in mathematical models of ventricular tissue. *Physical Review E*, 75(1):011929, 2007.

[100] H. Shen and Z. Jin. Two Dimensional Pattern Formation of Prey-predator System. In *Eighth ACIS International Conference on Software Engineering, Artificial Intelligence, Networking, and Parallel/Distributed Computing (SNPD 2007)*, volume 2, pages 343–346. IEEE, 2007.

[101] S. Sinha and S. Sridhar. *Patterns in excitable media: genesis, dynamics, and control.* CRC Press, 2014.

[102] W. Spotz and G. Carey. High-order compact scheme for the steady stream-function vorticity equations. *International Journal for Numerical Methods in Engineering*, 38(20):3497–3512, 1995.

[103] W. F. Spotz and G. Carey. High-order compact finite difference methods with applications to viscous flows. In *ISOSAHOM'95: Proceedings of the Third International Conference on Spectral and High Order Methods*, pages 397–408. Huston Journal of Mathematics, 1994.

[104] O. Steinbock, J. Schütze, and S. Müller. Electric-field-induced drift and deformation of spiral waves in an excitable medium. *Physical Review Letters*, 68(2):248, 1992.

[105] R. Straube, S. Vermeer, E. M. Nicola, and T. Mair. Inward rotating spiral waves in glycolysis. *Biophysical Journal*, 99(1):L4–L6, 2010.

[106] Y. Y. Tarasevich, V. V. Laptev, A. S. Burmistrov, and N. I. Lebovka. Pattern formation in a two-dimensional two-species diffusion model with anisotropic nonlinear diffusivities: a lattice approach. *Journal of Statistical Mechanics: Theory and Experiment*, 2017(9):093203, 2017.

[107] B. B. Theisen. Waves in Excitable Media. Master's thesis, Institutt for matematiske fag, 2012.

[108] A. M. Turing. The chemical basis of morphogenesis. *Bulletin of Mathematical Biology*, 52(1-2):153–197, 1990.

[109] K. H. W. J. Tusscher. *Spiral Wave Dynamics and Ventricular Arrhythmias*. 2004.

[110] J. J. Tyson and P. C. Fife. Target patterns in a realistic model of the Belousov-Zhabotinskii reaction. *The Journal of Chemical Physics*, 73(5):2224–2237, 1980.

[111] A. Winfree and S. Strogatz. Singular filaments organize chemical waves in three dimensions: I. Geometrically simple waves. *Physica D: Nonlinear Phenomena*, 8(1-2):35–49, 1983.

[112] A. Winfree and S. Strogatz. Singular filaments organize chemical waves in three dimensions: IV. Wave taxonomy. *Physica D: Nonlinear Phenomena*, 13(1-2):221–233, 1984.

[113] A. Winfree, E. Winfree, and H. Seifert. Organizing centers in a cellular excitable medium. *Physica D: Nonlinear Phenomena*, 17(1):109–115, 1985.

[114] A. T. Winfree. Spiral waves of chemical activity. *Science*, 175(4022):634–636, 1972.

[115] A. T. Winfree. Scroll-shaped waves of chemical activity in three dimensions. *Science*, 181(4103):937–939, 1973.

[116] A. T. Winfree and S. H. Strogatz. Organizing centres for three-dimensional chemical waves. *Nature*, 311(5987):611–615, 1984.

[117] X.-P. Yuan, J.-X. Chen, Y.-H. Zhao, G.-Q. Liu, and H.-P. Ying. Dynamics of Scroll Wave in a Three-Dimensional System with Changing Gradient. *PLOS One*, 11(3), 2016.

[118] A. Zaikin and A. Zhabotinsky. Concentration wave propagation in two-dimensional liquid-phase self-oscillating system. *Nature*, 225(5232):535–537, 1970.

[119] H. Zhang, B. Hu, G. Hu, and J. Xiao. Drift velocity of rotating spiral waves in the weak deformation approximation. *The Journal of Chemical Physics*, 119(8):4468–4472, 2003.

[120] V. S. Zykov. Spiral wave initiation in excitable media. *Philosophical Transactions of the Royal Society A: Mathematical, Physical and Engineering Sciences*, 376(2135):20170379, 2018.

Indian Institute of Technology Guwahati